POWER SPECTRAL DENSITY OF MULTI-LEVEL CONSTRAINED SEQUENCES WITH APPLICATIONS

A THESIS SUBMITTED TO
THE GRADUATE SCHOOL OF NATURAL AND APPLIED SCIENCES
OF
MIDDLE EAST TECHNICAL UNIVERSITY

BY

SERAL BUSE ATAK

IN PARTIAL FULFILLMENT OF THE REQUIREMENTS
FOR
THE DEGREE OF MASTER OF SCIENCE
IN
ELECTRICAL AND ELECTRONICS ENGINEERING

AUGUST 2024

Approval of the thesis:

POWER SPECTRAL DENSITY OF MULTI-LEVEL CONSTRAINED SEQUENCES WITH APPLICATIONS

submitted by **SERAL BUSE ATAK** in partial fulfillment of the requirements for the degree of **Master of Science in Electrical and Electronics Engineering Department, Middle East Technical University** by,

Prof. Dr. Naci Emre Altun
Dean, Graduate School of **Natural and Applied Sciences** _____

Prof. Dr. İlkay Ulusoy
Head of Department, **Electrical and Electronics Engineering** _____

Assist. Prof. Dr. Ahmed Hareedy
Supervisor, **Electrical and Electronics Engineering, METU** _____

Examining Committee Members:

Assist. Prof. Dr. Serkan Sarıtaş
Electrical and Electronics Engineering, METU _____

Assist. Prof. Dr. Ahmed Hareedy
Electrical and Electronics Engineering, METU _____

Assist. Prof. Dr. Ertan Kazıklı
Electrical and Electronics Engineering, TOBB ETU _____

Date: 22.08.2024

I hereby declare that all information in this document has been obtained and presented in accordance with academic rules and ethical conduct. I also declare that, as required by these rules and conduct, I have fully cited and referenced all material and results that are not original to this work.

Name, Surname: Seral Buse Atak

Signature :

ABSTRACT

POWER SPECTRAL DENSITY OF MULTI-LEVEL CONSTRAINED SEQUENCES WITH APPLICATIONS

Atak, Seral Buse
M.S., Department of Electrical and Electronics Engineering
Supervisor: Assist. Prof. Dr. Ahmed Hareedy

August 2024, 94 pages

In various data storage and transmission systems, certain data patterns are likely to result in errors when stored or transmitted. In order to enhance reliability in these systems, constrained coding is used to forbid such error-prone data patterns. Analyzing the power spectral density (PSD) of constrained sequences as random processes reveals important properties such as the average power at DC and the bandwidth. In this work, a new method is proposed to theoretically derive closed-form expressions for the PSD of multi-level constrained sequences, where the number of possible levels is greater than two, via their binary counterparts that share specific properties in regard to the constraint itself with the multi-level sequences. Constrained sequences associated with constrained codes used in modern two-dimensional magnetic recording (TDMR) and Flash memory systems are focused on. It is shown that the theoretical PSD derived matches the experimental PSD obtained via extensive Monte-Carlo simulations. Additionally, an approximation method for obtaining the PSD is proposed for codes that have more complex state diagrams. It is shown that the approximate PSD derived has quite a low mean squared error (MSE) error compared to the experimental PSD obtained via Monte-Carlo simulations.

Keywords: Constrained Codes, Multi-level Constrained Sequences, Power Spectral Density, Flash Memory, Magnetic Recording

ÖZ

ÇOK SEVİYELİ KISITLI DİZİLERİN GÜÇ SPEKTRAL YOĞUNLUĞU VE UYGULAMALARI

Atak, Seral Buse
Yüksek Lisans, Elektrik ve Elektronik Mühendisliği Bölümü
Tez Yöneticisi: Dr. Öğr. Üyesi. Ahmed Hareedy

Ağustos 2024 , 94 sayfa

Çeşitli veri depolama ve iletim sistemlerinde, belirli veri örüntülerinin saklanması veya iletilmesi sırasında hataların ortaya çıkması muhtemeldir. Bu sistemlerde güvenilirliği artırmak amacıyla, bu tür hataya açık veri örüntülerini engellemek için kısıtlı kodlama kullanılır. Kısıtlanmış dizilerin güç spektral yoğunluğunun (PSD) rastgele süreçler olarak analiz edilmesi, DC'deki ortalama güç ve bant genişliği gibi önemli özellikleri ortaya çıkarır. Bu çalışmada, olası seviyelerin sayısının ikiden büyük olduğu çok seviyeli kısıtlı dizilerin PSD'lerinin kapalı form ifadelerini, bu çok seviyeli dizilerin kısıtlamalarıyla belirli özellikleri paylaşan ikili karşılıkları aracılığıyla teorik olarak üretmek için yeni bir yöntem önerilmektedir. Modern iki boyutlu manyetik kayıt (TDMR) ve Flash bellek sistemlerinde kullanılan kısıtlı kodlarla ilişkili kısıtlı dizilere odaklanılmaktadır. Ürettilen teorik PSD'nin, kapsamlı Monte-Carlo simülasyonları yoluyla elde edilen deneysel PSD ile eşleştiği gösterilmektedir. Ek olarak, daha karmaşık durum diyagramlarına sahip kodlar için PSD elde etmek amacıyla bir yaklaşım yöntemi önerilmektedir. Önerilen yaklaşık PSD'nin, Monte-Carlo simülasyonlarıyla elde edilen deneysel PSD ile karşılaştırıldığında oldukça düşük ortalama

karesel hataya (MSE) sahip olduğu gösterilmiştir.

Anahtar Kelimeler: Kısıtlı Kodlar, Çok Seviyeli Kısıtlı Diziler, Güç Spektral Yoğunluğu, Flaş Bellek, Manyetik Kayıt

To my family

ACKNOWLEDGMENTS

My deepest gratitude goes to my supervisor, Assist. Prof. Dr. Ahmed Hareedy, whose support and guidance were instrumental throughout this study. This thesis would not have been possible without his invaluable assistance.

I am immensely grateful to my esteemed professors at METU, Prof. Şenan Ece Güran Schmidt and Assist. Prof. Serkan Sarıtaş, for their unwavering belief in me and their constant encouragement to strive for excellence. I extend my sincere thanks to the jury members, Assist. Prof. Serkan Sarıtaş and Assist. Prof. Ertan Kazıklı whose insightful feedback during my defense, greatly enhanced this work.

I am profoundly grateful to my family. To my father, Hacı Ali Atak, for his unwavering support and wisdom, guiding me with his experience and life insights. To my mother, Serpil Atak, for her endless love and care, whose energy has been a constant source of strength and motivation. To my dear sister, Eylül Özgür Atak, for her companionship and understanding, always lifting my spirits and sharing in both challenges and triumphs. Your collective support has been the cornerstone of my journey, and I am forever grateful for your love and encouragement.

Words cannot express my deepest gratitude to my grandparents, Hayriye Atak, Duran Çoban, Nazlı Çoban. Even though they are not familiar with my field of study, their love and constant prayers have been a tremendous source of comfort and strength. I wish to honor the memory of my beloved grandfather, Ahmet Atak, who passed away in 2012. I am sure he would be proud to see that I studied at the university, where he contributed during its construction. His unwavering belief in education has brought my family and me to where we are today.

I am thankful to my cats, Doja and Leo, for their constant companionship and the joy they brought into my life. Their playful antics and affectionate presence provided me with much-needed breaks and comfort during the long hours of work. Doja's curiosity and Leo's fierce demeanor were a source of inspiration and tranquility, helping me to

stay focused and balanced throughout this journey.

I am grateful to my dear friends who stood by me, often before I realized I needed their support. Surrounding oneself with loved ones is vital, especially during challenging times. Ceren Su Şimşek and Buse Ceren Olcay, the study-related photos we shared to motivate each other meant a lot to me. Bertay Eren, Selin Buket Aydoğdu, and Behre Nur Bice, I would be lost without your company in the department. Aslı Umay Öztürk, your knowledge and wisdom have always inspired me. Muhammed Safa Kabar, I am grateful to have met your kind and thoughtful soul.

I am deeply appreciative of Doğu Erkan Arkadaş, my companion on this academic journey. I continue to learn from your unique perspective while sharing some of the best moments of my life.

I wish to honor the memory of my dear friend Menderes Karakaş, whose amazing personality, curiosity, and kindness continue to inspire and guide me. His presence, even in his absence, has been a source of strength throughout this journey.

I am grateful to each member of our research team, REINS, for their kindness, especially Doğukan Özbayrak, who always answers my questions patiently. Lastly, I would like to thank TUBITAK for being a sponsor for our research team.

TABLE OF CONTENTS

LIST OF FIGURES

FIGURES

LIST OF ABBREVIATIONS

ABBREVIATIONS	
A-LOCO	Asymmetric LOCO
BER	Bit error rate
FER	Frame error rate
FSM	Finite state machine
FSTD	Finite state transition diagram
GF	Galois field
ICI	Inter-cell interference
ISI	Inter-symbol interference
ITI	Inter-track interference
LOCO	Lexicographically-ordered constrained
MLC	Multi-level cell
MR	Magnetic recording
MSE	Mean squared error
NRZ	Non-return-to-zero
NRZI	Non-return-to-zero inverted
ODMR	One-dimensional magnetic recording
OP-LOCO	Optimal plus LOCO
OSTD	One-step state transition diagram
OSTM	One-step state transition matrix
OT-LOCO	Optimal-T LOCO
PIS	Plus isolation
PLC	Penta-level cell

PSD	Power spectral density
QA-LOCO	Q-ary asymmetric LOCO
QLC	Quad-level cell
RLL	Run-length limited
SIS	Square isolation
S-LOCO	Symmetric LOCO
SLC	Single-level cell
SNR	Signal-to-noise ratio
SP-LOCO	Simple plus LOCO
TDMR	Two-dimensional magnetic recording
TD	Two-dimensional
TLC	Triple-level cell
WSS	Wide-sense stationary

CHAPTER 1

INTRODUCTION

In the growing age of information, data storage and transmission remain important concepts, and researchers have to keep up with the latest demand in terms of transmission rate, efficiency, and reliability [1]. Flash devices [2] and magnetic recording devices [3] are still in popular use for this purpose. Consequently, the development of more efficient coding schemes that can handle higher data volumes and rates continues to be a significant area of research [4].

The performance and characteristic properties of these coding schemes need to be measured, with one crucial performance criterion being the power spectral density (PSD) of the scheme [5]. PSD helps in analyzing how power is distributed across different frequency components [6, 7], which can impact the efficiency and reliability of data storage systems. PSD reveals crucial properties of the signal, like the average power at zero frequency, the bandwidth of the signal, and the discrete power components [8]. Therefore, obtaining and understanding the PSD of a coding scheme is essential for optimizing the performance of data storage devices. In the field of data transmission, the power spectra of coded streams produced by an FSM and transmitted over digital repeatered lines were discussed in [9] and [10]. For wireless communications, both numerical [11] and analytical [12] approaches to obtain the spectra of FSM-generated coded streams were explored. The power spectrum of a block-coded modulated signal using a multi-dimensional constellation was examined in [13]. Regarding data storage, the power spectra of specific FSM-based codes in MR systems were derived in [14], and spectral null analysis of (d, k) RLL codes in MR and magneto-optic systems was presented in [15]. The influence of asymmetry in coded data with non-return-to-zero (NRZ) signaling, which encodes data by repre-

senting 1 and 0 with two distinct signal levels without returning to a baseline between bits, on the power spectrum was outlined in [16]. Gallopoulos et al. [7] introduced a method for determining the power spectra of RLL codes associated with NRZI signaling for storage and transmission. Lastly, Centers et al. [8] proposed a method for obtaining the power spectrum of a binary constrained stream that is associated with level-based signaling and extends the method on finite-length constrained codes.

Constrained coding is a widely used coding scheme for Flash and magnetic recording devices [17, 18, 19, 20]. The main idea of constrained coding is preventing erroneous patterns from happening in the device with the developed encoding algorithm [21]. In 1948 [21], Shannon introduced constrained codes for preventing erroneous patterns from happening in the device with the developed encoding algorithm and defined the capacity for an input-constrained noiseless channel as the maximum information rate given the channel input constraints. Ideally, a good channel code should approach a code rate close to the constrained channel's Shannon capacity, use a simple implementation, and avoid the propagation of errors at the decoding process [22]. In real-life applications, this ideal becomes a compromise between these competing attributes according to the application requirements [22].

Researchers began utilizing constrained codes in magnetic recording devices employing peak detection to enhance data density [23]. These codes, known as (d, k) binary run-length-limited (RLL) codes, regulate the minimum and maximum distances between consecutive transitions, with the parameter d controlling the minimum spacing to reduce inter-symbol interference (ISI), which occurs when symbols overlap and interfere with each other during transmission, and the parameter k managing the maximum spacing to improve self-clocking [24]. RLL codes are linked to transition-based signaling, specifically in the binary case with bipolar non-return-to-zero inverted (NRZI) signaling where the absence of a transition indicates a '0', while a transition indicates a '1'.

Constrained codes are also commonly employed in various data transmission systems since they help reduce cross-talk between wires carrying the data [25] and ensure DC balance, meaning zero average power at zero frequency [26]. While the Run Length Limited (RLL) codes in [24] were originally designed using lexicographic

indexing, the focus of the coding community soon shifted to codes based on finite-state machines (FSMs) [27]. However, designing FSM-based constrained codes that approach capacity is a challenging task, and it becomes even harder for high-rate codes [28]. Constrained codes using lexicographic indexing were reintroduced in [29], drawing on the guidance from [30]. Recently, the basics of constrained coding have been revisited, and the family of lexicographically-ordered constrained (LOCO) codes is introduced [31], which are known to be capacity-achieving, generalizable, and reconfigurable [31].

There has been considerable work on theoretically obtaining the PSD of constrained codes, particularly for binary-level codes as mentioned above. However, there is a lack of research focused on obtaining the PSD for constrained codes with non-binary levels. Non-binary codes offer several advantages over binary codes, such as higher data density and improved error correction capabilities [32].

By extending the analysis for obtaining the PSD of a constrained code theoretically to non-binary constrained codes, this research addresses the specific challenges posed by their more complex state diagrams. The results of the proposed method are compared against those of Monte Carlo simulations, showing a perfect match.

This thesis also suggests a method for obtaining the PSD plots of multi-level constrained codes with more complex state diagrams approximately using a probabilistic manner. The results from this approximation technique are also compared against Monte Carlo simulations, with the mean squared error (MSE) found to be very low, indicating that the approximation works with minimal error. This thesis illustrates the theoretical derivations for multi-level constrained codes on Flash and magnetic recording devices that use LOCO codes [19]. With the derivations and verifications provided on LOCO codes, this work aims to suggest a generic framework for obtaining PSD for multi-level constrained codes.

The thesis organization is as follows. In Chapter 2, a detailed background is provided to the reader, including the basics of constrained codes, Flash devices, magnetic recording devices, and the properties of PSD and LOCO codes, and the literature review is presented. The literature review discusses the recent related work on obtaining the PSD of constrained codes. It highlights the yet undiscovered parts

and the theoretical derivation of the PSD offered for binary-constrained codes, which is explained in detail and constructs the base of this work. In Chapter 3, the suggested idea for mapping the binary theoretical work to multi-level constrained codes is demonstrated, and the application of this idea on magnetic recording devices with simple plus LOCO (SP-LOCO) codes is given. Chapter 4 extends the idea for the application on Flash memory devices that use Q-ary asymmetric LOCO (QA-LOCO) codes. Chapter 5 gives the approximation technique for multi-level constrained codes with more complex state diagrams. Lastly, Chapter 6 gives this thesis's conclusion and future directions.

CHAPTER 2

PRELIMINARIES

This chapter presents the background knowledge necessary for understanding the research presented in this thesis. Firstly, a comprehensive review of constrained codes in general is offered. Then, the work of Gallopoulos et al. [7] and Centers et al. [8] are explained in detail, which lay the foundations of the work conducted in this thesis. Lastly, the physical grounds for Flash and two-dimensional magnetic recording devices are illustrated to better understand the principles of constrained coding.

2.1 A Brief Overview of Constrained Coding

Constrained codes aim to avoid recording the sequences whose retrieval may cause an erroneous read by the system [21]. These error-prone patterns are likely to be caused by various factors that depend on the physical characteristics of the storage medium. For instance, deficiencies in the reading technology may cause such errors in magnetic recording devices [23, 27], while for Flash memories, the primary source of errors is the charge propagation in adjacent Flash cells [33]. Even though the improvements on the physical recording channel can help reduce some of the errors, it may not be the perfect solution since there exist some error-prone patterns that are unavoidable with enhancements due to the system medium [34, 35]. Another crucial reason for the increase of the errors in the device is aging [33]. Therefore, analyzing the spatial properties of the system and introducing system-dependent restrictions may help improve the system's overall data retrieval and reliability. Since the constraints chosen are system-dependent, they can be introduced in different forms, such as limitations on run lengths [24], transition counts [22], and the presence of specific

patterns [19].

Constrained coding has a wide application area other than magnetic recording devices, including Flash memory [23], optoelectronics devices [23], and even DNA data storage [36]. As mentioned in Chapter 1, the majority of the history of constrained codes focuses on FSM-based codes, which generally lack the qualities of generalizability and reconfigurability. LOCO codes that are introduced in [19] are very promising, considering the advantages of reconfigurability, scalability, and low encoding-decoding complexity. This thesis proposes exact and approximate methods for obtaining the PSD of multi-level constrained codes and applies the method to codes from the LOCO family. The following example gives the definition of a member from the LOCO family, namely symmetric-LOCO (S-LOCO) codes [31], and demonstrates how to find the Shannon capacity [21] for the described case.

A maxentropic binary $\mathcal{S}_x$-constrained code is defined as the set of all possible infinite-length binary codewords that do not contain any pattern in $\mathcal{S}_x$. $\mathcal{S}_x$-constrained codes forbid ISI patterns, which are the most error-prone data patterns in magnetic recording systems [31]. $\mathcal{S}_x$-constrained codes are also used in specific data transmission standards and are often linked with level-based signaling [31].

Let $\mathcal{S}_x = \{010, 101, 0110, 1001, \ldots, 0\mathbf{1}^x0, 1\mathbf{0}^x1\}$ with $|\mathcal{S}_x| = 2x$. The code achieves maximum entropy in the sense that it is not strictly contained in any other binary code satisfying the same constraint. An infinite length $\mathcal{S}_1$-constrained code forbids the patterns in the forbidden pattern set $\mathcal{T}$,

$$\mathcal{T} = \mathcal{S}_1 \triangleq \{010, 101\}. \tag{2.1}$$

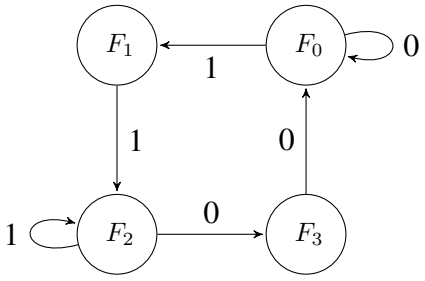

Figure 2.1: An FSTD for infinite-length $\mathcal{S}_1$-constrained sequence.

A finite state transition diagram (FSTD) representing an infinite length $\mathcal{S}_1$-constrained

sequence can be seen in Figure 2.1. The adjacency matrix $\mathbf{A}$ can be formed based on the FSTD shown in Figure 2.1 as follows:

$$\mathbf{A} = \begin{bmatrix} 1 & 1 & 0 & 0 \\ 0 & 0 & 1 & 0 \\ 0 & 0 & 1 & 1 \\ 1 & 0 & 0 & 0 \end{bmatrix}. \tag{2.2}$$

Let the maximum real positive eigenvalue of $\mathbf{A}$ be $\lambda_{\max}(\mathbf{A})$. Then the capacity C, which is the maximum achievable rate at which information can be transmitted reliably over a communication channel [21], for the infinite-length $\mathcal{S}_1$-constrained code can be calculated as:

$$C = \log_2(\lambda_{\max}(\mathbf{F})) = \log_2\left(\frac{1}{2}(1+\sqrt{5})\right) \approx 0.6942. \tag{2.3}$$

2.2 Power Spectral Density of Constrained Codes

PSD shows the distribution of a signal's power content on different frequencies [37]. It is widely used in various fields of research in order to have a quantitative measure of the characteristics of the signal [38, 39]. Deriving the PSD is also an important performance metric in data storage and transmission systems[5]. Since the PSD reveals to the system designer how power is distributed across different frequencies, the system designer becomes able to identify pivotal properties of the system, such as the average power of the stream at DC and the frequency range in which most of the power is allocated, i.e., the stream bandwidth and the discrete power components if they exist [6, 7].

There have been comprehensive studies about how power spectra can be obtained and utilized in data storage and transmission systems, which are represented in Chapter **??**. The most relevant work for this thesis is Gallopoulos et al.'s [7] and Centers et al.'s work [8], as it is primarily built on these two papers theoretically, which deal with constrained codes on binary sequences and can be considered an extension of their work to multi-level sequence constrained codes.

Gallopoulos et al.'s work [7] focuses on deriving a closed-form mathematical ex-

pression for the PSD of RLL codes. The method begins with finding the finite state transition diagram (FSTD) for the code, followed by deriving a suitable state diagram using state splitting and merging techniques. The main theorem is then applied based on this state diagram. The process of finding a suitable state diagram is rather complex, and the signaling method used in this work is NRZI.

In the work of Centers et al. [8], the theoretical foundations are equation-wise the same, but they are applied to LOCO codes [31], which use level-based signaling and can be considered more general than RLL codes in terms of their application area. A key contribution of this work is simplifying the process of finding the initial state diagram. Rather than using the more complicated state splitting and merging process, the creation of the state diagram is explicitly described. For LOCO codes that forbid sequences with k binary bits, all possible and allowed combinations of the last $k-1$ bits are written as states. The states are named according to the binary combination, and states that end with the binary bit '1' are selected. From these states, a reduction is applied, and a one-step state transition diagram (OSTD) is constructed. Finally, the necessary one-step state transition matrix (OSTM) is obtained, and the conversion to a closed mathematical formula of the PSD is achieved using a theorem analogous to the one proposed in [7]. A more detailed discussion of the theoretical derivation in this work will be given shortly.

2.2.1 Deriving the PSD for Binary Sequence Constrained Codes

Gallopoulos et al. [7] developed a method for calculating the power spectrum of RLL codes using NRZI signaling and involves an intermediate step for finding the initial state diagram that will be used in the theorem. Centers et al. [8] streamlines this approach by eliminating the intermediate sequence and presents a more direct method tailored for level-based signaling, making it more applicable to a broader range of constrained codes, such as LOCO codes. Given that the focus of the applications in this thesis is on LOCO codes, the steps and methodology of the main reference and steps will be taken from [8].

The FSTDs discussed in this method represent each state as a fixed number of the most recently generated bits. For notation, matrices will be represented with bold

and uppercase letters, while vectors, by default row vectors, will be represented as bold and lowercase vectors. Power spectral densities will be denoted by $S(\cdot)$, and one-step state transition matrices will be denoted by $\mathbf{G}(\cdot)$. These notations will also be adopted throughout the thesis.

First, an FSTD that shows how a sequence of binary data of 0s and 1s, namely $\{X_n\}$, is generated while following the system constraints. Each transition in the diagram should generate a single symbol, either a 1 or a 0, and the probability of each transition should be recorded. Also, all transitions leading to a state must have the same symbol generated.

Next, the one-step state transition diagram (OSTD) should be derived from the FSTD. In OSTD, only the states where the most recent bit is 1 are shown. The transitions in this diagram indicate the number of steps or symbols needed to move from one state to another based on the initial system FSTD. The probabilities for these transitions should also be noted. The sequence created by this diagram is referred to as $\{T_i\}$, where T_i represents the number of consecutive 0's plus the ending 1 of the ith run in $\{X_n\}$.

After the OSTD is created, the one-step transition matrix (OSTM) noted as $\mathbf{G}_{i,j}(D)$ is created using the edge probabilities and run lengths from the OSTD.

Define the probability of transitioning from state i to state j in the OSTD as $p_{i,j}(t)$ and the run length characterizing that transition as t. The general entry $\mathbf{G}_{i,j}(D)$ is given as follows where $p_{i,j}(t)$ is the probability of transitioning from state i to state j in the OSTD and t is the run length characterizing that transition:

$$\mathbf{G}_{i,j}(D) = \sum_{t=1}^{\infty} p_{i,j}(t) D^t. \tag{2.4}$$

Then, the closed-form expression for the PSD of a written or transmitted sequence using the OSTM will be derived where the following signal generation scheme is adopted:

$$\overset{\text{Code}}{\{X_n\}} \xrightarrow[\text{signaling}]{\text{NRZ}} \overset{\text{Modulation sequence}}{\{Y_n\}} \xrightarrow[\text{shaping}]{\text{Pulse}} \overset{\text{Write signal}}{W(t)} \quad . \tag{2.5}$$

The PSD function of a wide-sense-stationary (WSS) discrete-time process $\{X_n\}$ is

given as follows, where $\mathbb{R}_X(k)$ is the auto-correlation function with time lag k and D is defined as the complex exponential $e^{i2\pi fT}$ for some frequency f and bit interval T:

$$S_X(D) = \sum_{k=-\infty}^{\infty} \mathbb{R}_X(k) D^k = \sum_{k=-\infty}^{\infty} \mathbb{E}[X_0 X_k] D^k. \tag{2.6}$$

Then, the fundamental result analogous to [7] can be found. Assuming the Markov chain describing the code sequence generation is at equilibrium, the power spectrum $S_X(D)$ of the process $\{X_n\}$ is given as:

$$S_X(D) = p(1)\boldsymbol{\pi} \left[(\mathbf{I} - \mathbf{G}(D))^{-1} + (\mathbf{I} - \mathbf{G}(D^{-1}))^{-1} - \mathbf{I} \right] \mathbf{u}^{\mathsf{T}}, \tag{2.7}$$

where $\mathbf{u}$ is an all-one vector, $p(1) = \mathbb{P}[X_n = 1]$ for arbitrary n is the equilibrium probability of a 1 in $\{X_n\}$, $\mathbf{I}$ is the identity matrix of the same size as $\mathbf{G}(D)$, and $\boldsymbol{\pi}$ is the stationary distribution of the OSTD states represented by $\mathbf{G}(1)$. The proof regarding the result in (2.7) can be found in [8]. Observe that the independent variable in (2.7) is actually f since $D = e^{i2\pi fT}$. Therefore, the equation for power spectra will be notated as $S_X(f)$ from now on in this chapter to eliminate confusion.

Note that the stationary distribution $\boldsymbol{\pi}$ satisfies $\boldsymbol{\pi}\mathbf{u}^{\mathsf{T}} = 1$ and $\boldsymbol{\pi}\mathbf{G}(1) = 1$. It follows from the definition of $\{T_i\}$ and (2.4) that,

$$\mathbb{E}[T_i] = \frac{1}{p(1)} = \boldsymbol{\pi}\mathbf{G}'(1)\mathbf{u}^{\mathsf{T}}. \tag{2.8}$$

A more detailed discussion about the proof regarding the result in (2.8) can be found in [7].

Consider $\{Y_n\}$ as an example modulation sequence with $Y_n = 2X_n - 1$. Thus, for any $k \in \mathbb{Z}$,

$$\begin{aligned} \mathbb{R}_Y(k) = \mathbb{E}[Y_0 Y_k] &= \mathbb{E}[(2X_0 - 1)(2X_k - 1)] \\ &= 4\mathbb{E}[X_0 X_k] - 4p(1) + 1. \end{aligned} \tag{2.9}$$

Therefore, the PSD $S_Y(f)$ of $\{Y_n\}$ is as follows where $\delta(\cdot)$ is the Dirac delta function

and $D = e^{i2\pi fT}$:

$$\begin{aligned} S_Y(f) &= \sum_{k=-\infty}^{\infty} D^k \cdot \mathbb{E}[Y_0 Y_k] \\ &= 4S_X(f) + [1 - 4p(1)] \sum_{k=-\infty}^{\infty} D^k \\ &= 4S_X(f) + [1 - 4p(1)]\, \delta(f). \end{aligned} \tag{2.10}$$

Note that both the sequences $\{X_n\}$ and $\{Y_n\}$ are WSS since they are irreducible constrained systems and represented by strongly connected graphs. Their stationary distributions are independent of the starting points, and they are ergodic Markov chains. Additionally, all sequences described in this thesis will have the same properties. This examination is valid except for the cyclo-stationarity induced by the writing signal $W(t)$, which will be discussed shortly.

The modulation pulse function $P_T(t)$ is chosen as a rectangular pulse in the context of the work with bit interval T,

$$P_T(t) = \begin{cases} 1, & 0 \le t < T, \\ 0, & \text{otherwise.} \end{cases} \tag{2.11}$$

Then, the write signal $W(t)$ which is represented in (2.5) is given by:

$$W(t) = \sum_{n=-\infty}^{\infty} Y_n P_T(t - nT). \tag{2.12}$$

Even though the sequence $\{Y_n\}$ is WSS, the resultant signal becomes cyclo-stationary after it is convoluted with the writing signal $W(t)$. Therefore, the auto-correlation function $\mathbb{R}_Y(k)$ needs to be averaged over the period T. The PSD $S_W(f)$ of the write signal $W(t)$ is given as follows:

$$S_W(f) = \frac{1}{T}\text{sinc}^2(\pi fT)T^2 S_Y(f) = \text{sinc}^2(\pi fT)T S_Y(f). \tag{2.13}$$

Note that the result of the expression in (2.13) becomes as follows for $f = 0$:

$$S_W(0) = T S_Y(0) = T\left(4S_X(0) + [1 - 4p(1)]\, \delta(0)\right). \tag{2.14}$$

For the following discussions, both the paper [8] and the work on this thesis consider f to be the normalized frequency, i.e., T is set to 1.

Overall, the steps needed to be followed to obtain the PSD of a binary constrained sequence $\{X_n\}$ are FSTD $\rightarrow$ OSTD $\rightarrow$ OSTM $\rightarrow$ applying the formula given in (2.7). This fundamental result links the PSD to the transition matrix derived from the FSTD of the code by applying matrix operations and leveraging the stationary distribution of the code's state diagram. With this relationship between the code's transition structure and its spectral properties, a precise analysis of the power distribution in both infinite and finite-length constrained codes is enabled, and a framework for analyzing how the power in the signal is distributed across frequencies is provided, which is crucial for understanding the performance of constrained codes in terms of bandwidth and signal integrity.

2.3 Constrained Coding for Multi-Level Flash Memory and Two-Dimensional Magnetic Recording Devices

This section will provide detailed physical illustrations for Flash memory and magnetic recording devices. The presented background will be helpful in understanding the constraints used in the codes that will be studied later in this work. Fundamentals about the non-binary world of Flash and magnetic recording devices will also be mentioned.

2.3.1 Constrained Coding for Multi-Level Flash Memory

Toshiba introduced Flash memory in the 1980s as a type of non-volatile electronic storage [40]. Unlike volatile memory such as DRAM, Flash memory retains stored data even when power is lost, which makes it suitable for long-term data storage applications [41]. Over time, this new kind of storage of Flash memory changed how mass data was stored because electronic storage is much faster, although it costs more than magnetic storage [42]. Flash memory devices are currently ahead of magnetic recording devices in terms of storage density [43]. Also, it is widely used in applications ranging from consumer electronics like USB drives and smartphones to

enterprise-level storage solutions such as data centers and SSDs [44, 45, 46].

There are two main types of Flash memory: NAND and NOR. NAND Flash is commonly used in high-density storage applications like SSDs and memory cards due to its fast write and erase speeds, while NOR Flash is used in embedded systems and firmware storage, offering fast read speeds and random access capabilities [43, 47].

The architecture of Flash memory is based on floating-gate transistors, where data is stored as electrical charges trapped in an insulated gate [48]. Figure 2.2 shows an illustration of the Flash cell memory. Memory organization is hierarchical and structured into blocks and pages. Each block contains multiple pages, and data is written to or erased from memory at the block level. However, while data can be read at the page level, any modification, such as rewriting data, requires the entire block to be erased first. This erase-before-write characteristic is a core limitation of Flash memory that affects both its performance and longevity [49].

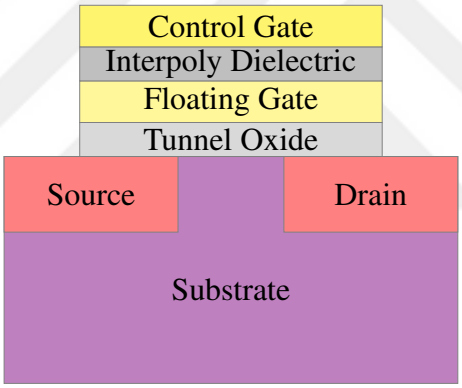

Figure 2.2: A Flash cell memory structure showing the source, drain, and substrate layers, including the control and floating gates.

In Flash memory systems, unwanted capacitances in and between floating-gate transistors cause charge movement during the programming process [50]. This movement of charge leads to inter-cell interference (ICI), which is a significant source of errors in Flash memory systems [51]. Some studies, such as [33] and [52], introduced special codes that prevent data patterns where an unprogrammed or erased cell is surrounded by two cells with the highest charge level. More recent studies such as [51] and [53] have shown that even patterns where the middle cell is programmed to be less than the highest level in the same arrangement should also be avoided. On top of these con-

cerns, as Flash devices age, the number of patterns that need to be avoided increases because charges can move across cells that are not next to each other [54, 28].

Constrained codes for Flash memories usually work with level-based signaling, where each symbol in a codeword is matched to a physical level in the system, such as a charge level in Flash memory [28, 55]. Constrained codes can help improve the performance and lifespan of Flash memory devices [51, 28].

2.3.2 Constrained Coding for Two-Dimensional Magnetic Recording Devices

The intense competition for higher storage density between magnetic and solid-state products has sparked creativity in various fields like physics, architecture, and data processing to create new storage technologies [56]. One of the most advanced magnetic technologies is two-dimensional magnetic recording (TDMR), which has shown the potential to reach storage densities of up to 10 terabits per square inch since its introduction [57, 58, 59].

TDMR is especially appealing because it increases storage density beyond what one-dimensional magnetic recording (ODMR) products can achieve by using architectural methods like track squeezing and shingled writing [58, 60] as well as advanced data processing techniques [61, 62] without needing new magnetic materials.

The write head in TDMR systems is typically larger than the individual tracks, leading to overlapping tracks during writing. This process is known as shingled writing, where new data partially overwrites the previously written track. This overlapping process introduces interference across tracks, which must be managed through signal processing [63].

The read head is responsible for detecting the magnetization of the grains. In TDMR, the read head produces a signal by sensing magnetization and convolving it with the response of the read head, followed by sampling at the center of the bit locations [63].

In TDMR, inter-track interference (ITI) is a significant challenge due to the overlapping nature of tracks caused by the shingled writing process. In traditional magnetic recording systems, each track is well-separated, minimizing ITI, with ISI mainly oc-

curring along individual tracks. However, in TDMR, as tracks are densely packed, the read head, which is larger than the individual tracks, picks up signals from adjacent tracks, resulting in severe ITI. This interference not only happens along a track but also across neighboring tracks, making the signal detection process more complex [63]. For more detailed information about TDMR, you can refer to a comprehensive survey in [63].

In the early ODMR devices, special codes were used to control the distance between transitions, which significantly helped increase storage density [27, 24]. These codes are still used today to improve the reliability of modern ODMR devices [17, 54].

In TDMR, certain data patterns where a bit is surrounded by opposite bits both horizontally and vertically are prone to errors [60, 64]. Since the channel's impulse response in TDMR is usually 3×3, grids of this size are typically used. These error-prone patterns can look like a square, where the bit in the center is surrounded by eight opposite bits on the 3×3 grid, called square isolation (SIS) patterns [65]. They can also look like a plus sign, where the bit in the center is surrounded by four opposite bits at a distance of 1, called plus isolation (PIS) patterns [60, 64, 66]. Figure 2.3 shows possible PIS patterns. When a TDMR system uses a wide read head, which reads three adjacent tracks at the same time [58, 61], the two-dimensional (TD) binary constraints can be changed into one-dimensional 8-ary constraints. This allows for non-binary coding schemes, such as OP-LOCO codes that forbid PIS patterns [31].

Research that explores the capacity of TD-constrained codes and suggests TD bit-stuffing techniques can be found in [66], [67] and [68]. There are also signal processing methods, such as TD equalization and TD detection schemes, that can help reduce media noise [61, 63]. It is important to note that the choice of which scheme to use is usually made by the TDMR system designer based on the balance between complexity and performance.

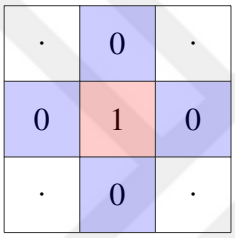

(a) PIS pattern where the center bit is 1.

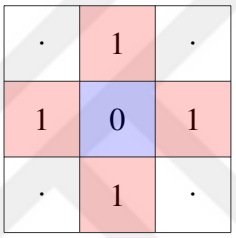

(b) PIS pattern where the center bit is 0.

Figure 2.3: PIS patterns in a 3×3 TDMR grid.

CHAPTER 3

PSD FOR MULTI-LEVEL CONSTRAINED CODES: SP-LOCO CODES

This chapter presents power spectra derivation for simple plus LOCO (SP-LOCO) codes [35]. Section 3.1 will provide a detailed discussion for SP-LOCO codes, Section 3.2 will show the step-by-step derivation for the PSD and Section 3.3 will present the results as a comparison between the theoretical derivation and experimental results obtained by Monte Carlo (MC) simulations.

3.1 SP-LOCO Codes

In the ongoing battle between Flash memory and magnetic recording devices, the recent improvements in magnetic recording devices based on the new TDMR technology caused a striking increase in the data storage density for magnetic recording devices [57, 58, 59]. One of the advantages of this new regime is that it uses the already-existing magnetic materials rather than the new ones [61]. Therefore, developing new coding schemes that can provide advanced signal processing algorithms is essential to achieve this beneficial system's potential [69].

In 2022, rate-wise optimal LOCO codes named OP-LOCO [31] and in 2024, named optimal-T LOCO (OT-LOCO) [34] were created to prevent specific error-prone TD patterns and enhance the functionality of a TDMR device that uses a wide read head to access three down tracks at once. Rate-wise optimization refers to minimal redundancy, achieved by building the code so that the average number of coding digits per message is kept to a minimum [70].

For designing codes for TDMR, usually, a two-dimensional binary-constrained cod-

ing problem is converted into a one-dimensional non-binary constrained coding problem [34, 31, 65], which makes the alphabet size for a 3×3 grid eight since there exist $2 \times 2 \times 2 = 8$ unique combinations. These ideal LOCO codes, OP-LOCO [31] and OT-LOCO [34], are more complex in terms of design, and they are more prone to codeword-to-message error propagation because of their large alphabet size, which is eight [35]. At the cost of some rate loss, constrained coding schemes that use alphabet sizes smaller than eight can help to reduce these issues, and they can also enable some uncoded tracks or data streams to be processed independently, which helps speed up reading in TDMR systems [35].

In July 2024, SP-LOCO codes were introduced [35], which prohibits plus isolation (PIS) patterns to provide lower complexity, lower error propagation, complete track separation, and better performance at the expense of a limited rate loss compared to its rate-optimal counterpart, OP-LOCO. Denoting a Galois field of size q by $\mathrm{GF}(q)$, where $q \geq 2$ is a prime power, SP-LOCO codes are defined over $\mathrm{GF}(2)$ instead of $\mathrm{GF}(8)$ as it is the case in OP-LOCO codes. With this modification, SP-LOCO codes allow the separation of uncoded streams [35], where the idea originated from their work in Flash memory systems where page separation was adopted [71].

ISI and inter-track interference (ITI) are two types of interference that can occur in TDMR devices. The former is caused by neighboring bits in the same track and the latter by nearby bits in adjacent tracks [58, 61]. ISI on the same down track and ITI on the same cross-track can cause the level at any 3×3 TD grid's center location to change sign, which if this level is isolated, results in an error when read [60].

When the central level on the TD grid is surrounded by four levels at Manhattan distance 1 with the complementary sign, the corresponding 3×3 binary pattern is called a plus isolation pattern [64, 66]. SP-LOCO codes intend to prevent the writing of any PIS patterns [35] similar to its rate-optimal counterpart, OP-LOCO codes [31].

For the following discussions, let $\mathrm{GF}(2) = \{0, 1\}$ and $\mathrm{GF}(8) = \{0, 1, \alpha, \alpha^2, \ldots, \alpha^6\}$, where α is a primitive element of $\mathrm{GF}(8)$. The following standard mapping-demapping from the binary 3×1 pattern to the GF symbol is used for OP-LOCO as in the $\mathrm{GF}(8)$ column and SP-LOCO codes as in the $\mathrm{GF}(2)$ column, where a symbol in GF represents a column with 3 bits to be written on three adjacent down tracks in the same

group:

$$
\begin{array}{ccccc}
3-\text{Tuple} & & \text{GF}(8) & & \text{GF}(2) \\
[0\ 0\ 0]^{\text{T}} & \longleftrightarrow & 0 & \longleftrightarrow & 0, \\
[0\ 0\ 1]^{\text{T}} & \longleftrightarrow & 1 & \longleftrightarrow & 0, \\
[0\ 1\ 0]^{\text{T}} & \longleftrightarrow & \alpha & \longleftrightarrow & 1, \\
[0\ 1\ 1]^{\text{T}} & \longleftrightarrow & \alpha^2 & \longleftrightarrow & 1, \\
[1\ 0\ 0]^{\text{T}} & \longleftrightarrow & \alpha^3 & \longleftrightarrow & 0, \\
[1\ 0\ 1]^{\text{T}} & \longleftrightarrow & \alpha^4 & \longleftrightarrow & 0, \\
[1\ 1\ 0]^{\text{T}} & \longleftrightarrow & \alpha^5 & \longleftrightarrow & 1, \\
[1\ 1\ 1]^{\text{T}} & \longleftrightarrow & \alpha^6 & \longleftrightarrow & 1.
\end{array} \tag{3.1}
$$

Let $\mathcal{T}$ be a finite set of forbidden patterns. PIS patterns are eliminated by forbidding the $\text{GF}(2)$ 3-tuple patterns in $\mathcal{T} = \{010, 101\}$ on the middle track [35].

The SP-LOCO coding scheme is introduced for each group of three down tracks as follows: firstly, applying a $\text{GF}(2)$ constrained code on the middle track such that all PIS patterns are eliminated, and then leaving the data on the upper and lower tracks uncoded [35].

The critical point here is that the $\text{GF}(2)$ code that is applied on the middle track is the S-LOCO code itself [31], which was discussed in Section 2.1.

An S-LOCO code of length m and parameter x, the set of forbidden patterns $\mathcal{T} = \{010, 101\}$ and the code is denoted as $\mathcal{SC}^2_{m,1}$ [31]. Therefore, an SP-LOCO code of length m, which is denoted by $\mathcal{SPC}^2_m$, actually has $\mathcal{SC}^2_{m,1}$ applied on the middle track, and uncoded data on the upper and lower tracks, which leads to track separation [35].

For SP-LOCO, the enumerating of the codewords, the encoding-decoding rule formulation, bridging, and self-clocking are also achieved via the instructions defined for $\mathcal{SC}^2_{m,1}$ [35].

As calculated in Section 2.1, the capacity in input bits per coded symbol of an $\mathcal{SC}^2_{m,1}$ code is $C = 0.6942$. For SP-LOCO, $\mathcal{SPC}^2_m$, coding is applied only on the middle track, and $\mathcal{SC}^2_{m,1}$ code capacity can directly be used for the middle track. Since the

upper and lower tracks are uncoded for $\mathcal{SPC}_m^2$, capacity is 1. Therefore, the normalized capacity C_n of an $\mathcal{SPC}_m^2$ code is $C_n = (0.6942 + 2)/3 = 0.8981$. Hence, the code $\mathcal{SPC}$ is capacity-achieving under such constraint setup [35].

The capacity for OP-LOCO codes is calculated as 0.9710 in [31]. The capacity loss of SP-LOCO compared to OP-LOCO resulted by forbidding more patterns than needed [35], which will be demonstrated in detail shortly.

The forbidden pattern set for OP-LOCO codes that are defined over $\mathrm{GF}(8)$ is as follows:

$$\begin{aligned}\mathcal{T} = \mathcal{OP}^8 \triangleq \big\{ &\bar{\beta}_1 \alpha \beta_1, \bar{\beta}_2 \alpha^4 \beta_2, \forall \bar{\beta}_1, \beta_1 \in \{0, 1, \alpha^3, \alpha^4\} \\ &\text{and} \, \forall \bar{\beta}_2, \beta_2 \in \{\alpha, \alpha^2, \alpha^5, \alpha^6\} \big\} . \end{aligned} \tag{3.2}$$

The forbidden pattern set for SP-LOCO codes that are defined over $\mathrm{GF}(2)$ and their $\mathrm{GF}(8)$ equivalent symbols are as follows:

$$\begin{aligned}\mathcal{T} = \mathcal{SPC}_m^2 &\triangleq \{010, 101\}, \\ &= \Big\{ \hat{\beta}_1 \beta_2 \bar{\beta}_1, \hat{\beta}_2 \bar{\beta}_1 \bar{\beta}_2, \forall \hat{\beta}_1, \bar{\beta}_1, \beta_1 \in \{0, 1, \alpha^3, \alpha^4\} \\ &\quad \text{and} \quad \forall \hat{\beta}_2, \bar{\beta}_2, \beta_2 \in \{\alpha, \alpha^2, \alpha^5, \alpha^6\} \Big\} . \end{aligned} \tag{3.3}$$

It can be seen from (3.2) that the number of forbidden patterns in OP-LOCO codes is $(4 \times 4) + (4 \times 4) = 32$, while it is $(4 \times 4 \times 4) + (4 \times 4 \times 4) = 128$ for SP-LOCO codes. Defining SP-LOCO codes over $\mathrm{GF}(2)$ creates a more simplistic design while forbidding more patterns than needed, ultimately resulting in some capacity loss.

In [35], the probability analysis of the transition rates on the TDMR grid is investigated for different coding schemes. It is seen that the average transition rate of SP-LOCO codes is lower than OP-LOCO codes' [35]. This analysis gives insights into how the coding schemes can be adjusted as the TDMR device ages, benefiting the reconfigurability characteristic of the LOCO codes [35]. Since the OP-LOCO coding scheme has higher rates, it can be utilized in the earlier times of the device, and the coding scheme might be changed to SP-LOCO at an intermediate point in the device lifespan to improve performance [35].

OP-LOCO codes, which are defined over $\mathrm{GF}(8)$, need large adder sizes that result

in high complexity. In contrast, SP-LOCO codes have significantly lower complexity, error propagation, and processing latency through the complete track separation achieved by two tracks having uncoded data that enables the use of a smaller-size field $\mathrm{GF}(2)$ [35].

3.2 Theoretical Derivation of PSD for SP-LOCO Codes

This section will provide the theoretical derivation for obtaining the PSD for SP-LOCO codes. SP-LOCO codes are finite-length codes. However, the derivation will be for infinite-length SP-LOCO codes. From now on, SP-LOCO codes will mean infinite-length SP-LOCO codes. Observe that (3.1) and (3.3) still apply to infinite length SP-LOCO codes since the results do not change with codeword length m. Also, note that normalized frequency is used for all sequences described here, which makes the period $T = 1$.

In the TDMR setup [34], level-based signaling is adopted before writing the binary data to the tracks. Each 0 is converted into level $-A$, while each binary bit 1 is converted into level $+A$.

The TDMR medium is characterized by a wide read that reads 3 bits of data from the adjacent down tracks simultaneously, where the center of the read head is always at the middle track in each group of 3 down tracks [58]. As a result, the middle track of each 3×1 down track suffers from the highest interference, and the middle track level dominates the overall level of each 3×1 down track [34].

Each 3×1 down track read is mapped to a physical level. There exist $2 \times 2 \times 2 = 8$ combinations and they can be defined over $\mathrm{GF}(8)$, which will later be mapped to $\mathrm{GF}(2)$ as SP-LOCO codes suggest. With the symmetry due to level-based signaling by $-A$ and $+A$, it can be concluded that the dual 3-tuples will be mapped to the same physical level in magnitude with $+/-$ changing. 3-tuples having all bits as the same sign will have the highest magnitude level, and this applies to 2 combinations, $[0\ 0\ 0]^{\mathrm{T}}$ and $[1\ 1\ 1]^{\mathrm{T}}$. Considering the middle track domination, 3-tuples having the first and the third track bits in the complementary sign with respect to the middle track will have the lowest magnitude level, and this also applies to 2 combinations, $[0\ 1\ 0]^{\mathrm{T}}$

and $[1\ 0\ 1]^{\mathrm{T}}$. Lastly, 3-tuples having the first or the third track bits in complementary sign with respect to the middle track will have a magnitude in between the highest and lowest levels, and this applies to all 4 combinations that were left because there will be no difference between the physical levels read by the magnetic read head. A more detailed discussion about data-dependent readback amplitude distributions for various input data patterns can be found at [62].

Let the symbol corresponding to each physical level be as follows, where $a_0 > a_1 = a_2 > a_3 > 0$ using the discussion above:

$$\begin{aligned}
&3-\text{Tuple} && \text{GF}(8) && \text{Level} \\
&[0\ 0\ 0]^{\mathrm{T}} && \longleftrightarrow && 0 && \longleftrightarrow -a_0, \\
&[0\ 0\ 1]^{\mathrm{T}} && \longleftrightarrow && 1 && \longleftrightarrow -a_1, \\
&[0\ 1\ 0]^{\mathrm{T}} && \longleftrightarrow && \alpha && \longleftrightarrow +a_3, \\
&[0\ 1\ 1]^{\mathrm{T}} && \longleftrightarrow && \alpha^2 && \longleftrightarrow +a_2, \\
&[1\ 0\ 0]^{\mathrm{T}} && \longleftrightarrow && \alpha^3 && \longleftrightarrow -a_2, \\
&[1\ 0\ 1]^{\mathrm{T}} && \longleftrightarrow && \alpha^4 && \longleftrightarrow -a_3, \\
&[1\ 1\ 0]^{\mathrm{T}} && \longleftrightarrow && \alpha^5 && \longleftrightarrow +a_1, \\
&[1\ 1\ 1]^{\mathrm{T}} && \longleftrightarrow && \alpha^6 && \longleftrightarrow +a_0.
\end{aligned} \tag{3.4}$$

Let the sequence of the physical levels be $\{Y_n\}$ where $Y_n \in \{\pm a_0, \pm a_1, \pm a_2, \pm a_3\}$. Since the code is symmetric, the probability for each 8 physical level is equivalent.

$$\begin{aligned}
\mathbb{P}[Y_n = a_0] = \mathbb{P}[Y_n = a_1] = \mathbb{P}[Y_n = a_2] = \mathbb{P}[Y_n = a_3] = 0.125, \\
\mathbb{P}[Y_n = -a_0] = \mathbb{P}[Y_n = -a_1] = \mathbb{P}[Y_n = -a_2] = \mathbb{P}[Y_n = -a_3] = 0.125, \\
\mathbb{P}[Y_n = y_n] = 0.125, \quad y_n \in \{\pm a_0, \pm a_1, \pm a_2, \pm a_3\}.
\end{aligned} \tag{3.5}$$

Observe that 3-tuples having their middle bit as 0 are mapped to negative physical levels while 3-tuples having their middle bit as 1 are mapped to positive physical levels in (3.4). Let the binary mapping sequence be $\{X_n\}$ where $X_n \in \{0, 1\}$:

$$X_n = \begin{cases} 1, & \text{if } Y_n \in \{a_0, a_1, a_2, a_3\}, \\ 0, & \text{else.} \end{cases} \tag{3.6}$$

Also, it can be observed from (3.6) that,

$$\mathbb{P}[X_n = 0] = \mathbb{P}[X_n = 1] = 0.5. \tag{3.7}$$

In order to simplify the expressions and improve the readability of the equations, the following notations will be used throughout the derivation:

$$\begin{aligned} p_{00} &= \mathbb{P}[X_0 = 0, X_k = 0], \\ p_{01} &= \mathbb{P}[X_0 = 0, X_k = 1], \\ p_{10} &= \mathbb{P}[X_0 = 1, X_k = 0], \\ p_{11} &= \mathbb{P}[X_0 = 1, X_k = 1]. \end{aligned} \tag{3.8}$$

Then, the auto-correlation function of the sequence $\{X_n\}$ can be written as:

$$\mathbb{R}_X(k) = \mathbb{E}[X_0 X_k] = 0 \cdot 0 \cdot p_{00} + 0 \cdot 1 \cdot p_{01} + 1 \cdot 0 \cdot p_{10} + 1 \cdot 1 \cdot p_{11} = p_{11}. \tag{3.9}$$

Since SP-LOCO codes are symmetric, it can be concluded that:

$$\begin{aligned} p_{11} &= p_{00}, \\ p_{10} &= p_{01}. \end{aligned} \tag{3.10}$$

The unit measure axiom of probability theory allows to write,

$$p_{00} + p_{01} + p_{10} + p_{11} = 1. \tag{3.11}$$

Using equations (3.9) and (3.10) in (3.11) leads to:

$$\begin{aligned} 2p_{11} + 2p_{10} &= 1. \\ 2p_{10} &= 1 - 2p_{11} \\ p_{10} &= 0.5 - p_{11}. \end{aligned} \tag{3.12}$$

For the auto-correlation function of $\{Y_n\}$ where $k \neq 0$, $a_m, a_n \in \{a_0, a_1, a_2, a_3\}$ and

$m, n \in \{0, 1, 2, 3\}$:

$$\begin{aligned}\mathbb{R}_Y(k) = \mathbb{E}[Y_0 Y_k] = &\sum_{m=0}^{3}\sum_{n=0}^{3} a_m a_n \mathbb{P}[Y_0 = a_m, Y_k = a_n] \\ &- \sum_{m=0}^{3}\sum_{n=0}^{3} a_m a_n \mathbb{P}[Y_0 = a_m, Y_k = -a_n] \\ &- \sum_{m=0}^{3}\sum_{n=0}^{3} a_m a_n \mathbb{P}[Y_0 = -a_m, Y_k = a_n] \\ &+ \sum_{m=0}^{3}\sum_{n=0}^{3} a_m a_n \mathbb{P}[Y_0 = -a_m, Y_k = -a_n], \quad k \neq 0. \end{aligned} \tag{3.13}$$

Using the symmetric property of SP-LOCO codes on Y_n probabilities:

$$\begin{aligned}\mathbb{E}[Y_0 Y_k] = &2 \cdot \sum_{m=0}^{3}\sum_{n=0}^{3} a_m a_n \mathbb{P}[Y_0 = a_m, Y_k = a_n] \\ &- 2 \cdot \sum_{m=0}^{3}\sum_{n=0}^{3} a_m a_n \mathbb{P}[Y_0 = a_m, Y_k = -a_n], \quad k \neq 0. \end{aligned} \tag{3.14}$$

Define the first probability that has same signed physical levels $\mathbb{P}[Y_0 = a_m, Y_k = a_n]$ as p_{S}, where $a_m, a_n \in \{a_0, a_1, a_2, a_3\}$, $m, n \in \{0, 1, 2, 3\}$ and $k \neq 0$. Using results from (3.5), (3.7) and (3.9),

$$\begin{aligned} p_{\mathrm{S}} &= \mathbb{P}[Y_0 = a_m, Y_k = a_n] \\ &= \sum_{x_0}\sum_{x_k} \mathbb{P}[Y_0 = a_m, Y_k = a_n \mid X_0 = x_0, X_k = x_k] \cdot \mathbb{P}[X_0 = x_0, X_k = x_k] \\ &= \mathbb{P}[Y_0 = a_m, Y_k = a_n \mid X_0 = 1, X_k = 1] \cdot p_{11} \\ &= \mathbb{P}[Y_0 = a_m \mid X_0 = 1] \cdot \mathbb{P}[Y_k = a_m \mid X_k = 1] \cdot p_{11} \\ &= \left(\frac{0.125}{0.5}\right)^2 \cdot p_{11} \\ &= \frac{p_{11}}{16}. \end{aligned} \tag{3.15}$$

Define the second probability that has different signed physical levels $\mathbb{P}[Y_0 = a_m, Y_k = -a_n]$ as p_{S}, where $a_m, a_n \in \{a_0, a_1, a_2, a_3\}$, $m, n \in \{0, 1, 2, 3\}$ and $k \neq 0$. Using

results from (3.5), (3.7) and (3.12),

$$\begin{aligned}
p_{\mathrm{D}} &= \mathbb{P}[Y_0 = a_m, Y_k = -a_n] \\
&= \sum_{x_0} \sum_{x_k} \mathbb{P}[Y_0 = a_m, Y_k = -a_n \mid X_0 = x_0, X_k = x_k] \cdot \mathbb{P}[X_0 = x_0, X_k = x_k] \\
&= \mathbb{P}[Y_0 = a_m, Y_k = -a_n \mid X_0 = 1, X_k = 0] \cdot p_{10} \\
&= \mathbb{P}[Y_0 = a_m \mid X_0 = 1] \cdot \mathbb{P}[Y_k = -a_n \mid X_k = 0] \cdot p_{10} \\
&= \left(\frac{0.125}{0.5}\right) \cdot \left(\frac{0.125}{0.5}\right) \cdot (0.5 - p_{11}) \\
&= \frac{(0.5 - p_{11})}{16}.
\end{aligned} \tag{3.16}$$

Now, using equations (3.15) and (3.16) in (3.14) gives the result of:

$$\begin{aligned}
\mathbb{E}[Y_0 Y_k] &= 2 \sum_{m=0}^{3} \sum_{n=0}^{3} a_m a_n \cdot \frac{p_{11}}{16} - 2 \sum_{m=0}^{3} \sum_{n=0}^{3} a_m a_n \cdot \left(\frac{0.5 - p_{11}}{16}\right) \\
&= \frac{1}{16} \cdot \sum_{m=0}^{3} \sum_{n=0}^{3} a_m a_n \cdot (4\mathbb{E}[X_0 X_k] - 1), \quad k \neq 0.
\end{aligned} \tag{3.17}$$

Define the multiplier term as S, then (3.17) becomes:

$$\begin{aligned}
S &= \frac{1}{16} \cdot \sum_{m=0}^{3} \sum_{n=0}^{3} a_m a_n, \\
\mathbb{E}[Y_0 Y_k] &= S \cdot (4\mathbb{E}[X_0 X_k] - 1), \\
\mathbb{R}_Y(k) &= S\,(4\mathbb{R}_X(k) - 1), \quad k \neq 0.
\end{aligned} \tag{3.18}$$

Note that the result in 3.18 is found by using the total probability theorem, and since the symbol probabilities are equivalent, the operation applied here is just averaging.

After obtaining $\mathbb{E}[Y_0 Y_k]$ in terms of $\mathbb{E}[X_0 X_k]$, Discrete Fourier Transform can be applied to auto-correlation functions to obtain the power spectrum as follows where $\mathbb{R}_Y(k)$ is the auto-correlation function with time lag k, frequency f and period 1:

$$S_Y(f) = \sum_{k=-\infty}^{\infty} \mathbb{R}_Y(k) \cdot e^{i2\pi fk} = \sum_{k=-\infty}^{\infty} \mathbb{E}[Y_0 Y_k] \cdot e^{i2\pi fk}. \tag{3.19}$$

However, the expression given in (3.19) requires $\mathbb{R}_Y(0)$ term also. The expression found for $\mathbb{R}_Y(k)$ in (3.17) is for $k \neq 0$, and the relation becomes incorrect for the

case of $k = 0$. Because when $k = 0$, Y_0 and Y_k become the same. This problem will also occur in the later chapters since the method of mapping a non-binary sequence to a binary sequence and derivations for expressing one in terms of the other will be used. Therefore, a general solution for this problem will be introduced so that it will be easier to obtain correct PSDs in all chapters.

First, the Kronecker delta function is denoted as $\delta[k]$, where:

$$\delta[k] = \begin{cases} 1 & \text{if } k = 0 \\ 0 & \text{if } k \neq 0. \end{cases} \tag{3.20}$$

Assume the auto-correlation function for $\{X_n\}$ is given as $\mathbb{R}_X(k)$. Also, assume that the following relation is given between $\mathbb{R}_Y(k)$ and $\mathbb{R}_X(k)$ where a and b are real-valued constants and $k \neq 0$. Note that this relation might not give the true auto-correlation value for $k = 0$.

$$\mathbb{R}_Y(k) = a\mathbb{R}_X(k) + b, \quad k \neq 0. \tag{3.21}$$

Then, the following auto-correlation function can be written for $\{Y_n\}$,

$$\begin{aligned} \mathbb{E}[Y_0 Y_k] = \mathbb{R}_Y(k) &= \begin{cases} a\mathbb{R}_X(k) + b, & \text{if } k \neq 0, \\ \mathbb{R}_Y(0), & \text{if } k = 0. \end{cases} \\ &= a\mathbb{R}_X(k) + b + (\mathbb{R}_Y(0) - (a\mathbb{R}_X(0) + b))\,\delta[k]. \end{aligned} \tag{3.22}$$

Applying the formula given in (3.19) for turning the auto-correlation function to power spectra using (3.22) and (3.21) gives the following result where $S_X(f)$ is the power spectra of $\{X_n\}$:

$$\begin{aligned} S_Y(f) &= \sum_{k=-\infty}^{\infty} \Big(a\mathbb{R}_X(k) + b + \big(\mathbb{R}_Y(0) - (a\mathbb{R}_X(0) + b)\big)\delta[k] \Big) e^{i2\pi fk} \\ &= aS_X(f) + b\delta(f) + \big(\mathbb{R}_Y(0) - (a\mathbb{R}_X(0) + b)\big). \end{aligned} \tag{3.23}$$

Observe that the above offset $\big(\mathbb{R}_Y(0) - (a\mathbb{R}_X(0) + b)\big)$ is a constant in the PSD $S_Y(f)$, $\forall f$, it is not the Dirac delta function $\delta(\cdot)$.

For ease of notation for the later derivations, the following naming convention will be used for deriving $S_Y(f)$ where $\mathbb{R}_Y(k)$ is defined as in (3.22):

$$\begin{aligned}
\text{Addition} &= \mathbb{R}_Y(0) = \mathbb{E}[Y_n^2], \\
\text{Subtraction} &= a\mathbb{R}_X(0) + b, \\
\text{Correction} &= \text{Addition} - \text{Subtraction}, \\
S_Y(f) &= aS_X(f) + b\delta(f) + \text{Correction}.
\end{aligned} \tag{3.24}$$

Another general conclusion that will be useful for this and the later chapters will be provided using $\mathbb{R}_Y(k)$ defined as in (3.22) regarding the Dirac delta functions existence in $S_Y(f)$. Remember that all sequences that will be considered in this thesis work will be wide sense stationary (WSS) processes, as discussed earlier in Subsection 2.2.1, and WSS processes have time-invariant mean and auto-correlation functions.

The auto-correlation function given for $\{Y_n\}$ in (3.22) can be rewritten as follows where $\mathbb{C}_X(k)$ represents the auto-covariance function of $\{X_n\}$:

$$\begin{aligned}
\mathbb{R}_Y(k) &= a\mathbb{R}_X(k) + b + \big(\mathbb{R}_Y(0) - (a\mathbb{R}_X(0) + b)\big)\delta[k] \\
&= a\left(\mathbb{R}_X(k) - \mathbb{E}^2[X_n] + \mathbb{E}^2[X_n]\right) + b + \big(\mathbb{R}_Y(0) - (a\mathbb{R}_X(0) + b)\big)\delta[k] \\
&= a\left(\mathbb{R}_X(k) - \mathbb{E}^2[X_n]\right) + a\mathbb{E}^2[X_n] + b + \big(\mathbb{R}_Y(0) - (a\mathbb{R}_X(0) + b)\big)\delta[k] \\
&= a\mathbb{C}_X(k) + a\mathbb{E}^2[X_n] + b + \big(\mathbb{R}_Y(0) - (a\mathbb{R}_X(0) + b)\big)\delta[k]
\end{aligned} \tag{3.25}$$

Now, the Fourier transform will be applied to $\mathbb{R}_Y(k)$ to obtain power spectra where $\mathcal{F}\{\,\cdot\}$ represents the Fourier transform.

$$\begin{aligned}
S_Y(f) &= \sum_{k=-\infty}^{\infty} \Big(a\mathbb{C}_X(k) + a\mathbb{E}^2[X_n] + b + \big(\mathbb{R}_Y(0) - (a\mathbb{R}_X(0) + b)\big)\delta[k]\Big)e^{i2\pi fk} \\
&= a\mathcal{F}\{\mathbb{C}_X(k)\} + \big(a\mathbb{E}^2[X_n] + b\big)\,\delta(f) + \big(\mathbb{R}_Y(0) - (a\mathbb{R}_X(0) + b)\big)
\end{aligned} \tag{3.26}$$

From (3.26), it can be observed that $a\mathcal{F}\{\mathbb{C}_X(k)\}$ term will not result in a delta function and $\big(\mathbb{R}_Y(0) - (a\mathbb{R}_X(0) + b)\big)$ term is a constant offset. Therefore, in $S_Y(f)$ there exists a delta function with an area of $(a\mathbb{E}^2[X_n] + b)$. It can also be concluded that for a sequence $\{Y_n\}$ which has an auto-correlation function defined as in (3.22),

a discrete component in $S_Y(f)$ exists only if $(a\mathbb{E}^2[X_n]+b)$ is non-zero. Also, observe that this term equals $\mathbb{E}^2[Y_n]$. Hence, if $\mathbb{E}^2[X_n]=-\frac{b}{a}$, it can be concluded that $S_Y(f)$ is continuous and does not involve a delta function. For readers' convenience for later derivations, these conclusions will expressed as follows where $S_Y^c(f)$ and $S_Y^d(f)$ represent the continuous and discrete parts of $S_Y(f)$ respectively:

$$\begin{aligned} S_Y(f) &= S_Y^c(f) + S_Y^d(f), \\ S_Y^d(f) &= \mathbb{E}^2[Y_n]\delta(f) = \left(a\mathbb{E}^2[X_n]+b\right)\delta(f), \\ \mathbb{E}^2[X_n] &= -\frac{b}{a} \implies S_Y^d(f) = 0. \end{aligned} \tag{3.27}$$

Note that equations from (3.27) to (3.34) were provided for a general $\mathbb{R}_X(k)$. Now, the derivation of PSD for SP-LOCO codes will be continued. Using (3.18), $\mathbb{R}_Y(k)$ can be written as follows:

$$\mathbb{R}_Y(k) = \begin{cases} S\left(4\mathbb{R}_X(k)-1\right), & \text{if } k \neq 0, \\ \mathbb{R}_Y(0), & \text{if } k = 0. \end{cases} \tag{3.28}$$

Since $\mathbb{R}_Y(k)$ found for SP-LOCO codes in (3.28) is in the shape of general $\mathbb{R}_Y(k)$ which is defined in (3.22), respective a and b constants in (3.21) can be written as follows:

$$\begin{aligned} a &= 4S, \\ b &= -S. \end{aligned} \tag{3.29}$$

Using the definitions in (3.24), the following expressions can be written:

$$\begin{aligned} \text{Addition} &= \mathbb{R}_Y(0) = \mathbb{E}[Y_n^2] \\ &= \frac{1}{8}\cdot\left[\sum_{n=0}^{3} a_n^2 + \sum_{n=0}^{3}(-a_n)^2\right] = \frac{1}{4}\sum_{n=0}^{3} a_n^2, \end{aligned} \tag{3.30}$$

$$\begin{aligned} \text{Subtraction} &= a\mathbb{R}_X(0) + b \\ &= 4S\mathbb{E}[X_n^2] - S \\ &= 4S\frac{1}{2} - S = S, \end{aligned} \tag{3.31}$$

$$\begin{aligned}\text{Correction} &= \text{Addition} - \text{Subtraction},\\ &= \frac{1}{4}\sum_{n=0}^{3} a_n^2 - S,\end{aligned} \tag{3.32}$$

$$\begin{aligned}S_Y(f) &= aS_X(f) + b\delta(f) + \text{Correction}\\ &= 4S \cdot S_X(f) - S\delta(f) + \frac{1}{4}\sum_{n=0}^{3} a_n^2 - S.\end{aligned} \tag{3.33}$$

Now, using the second general conclusion in (3.27), the existence of the Dirac delta function will be inspected.

$$\begin{aligned}S_Y^d(f) &= \left(a\mathbb{E}^2[X_n] + b\right)\delta(f)\\ &= \left(4S\left(\frac{1}{2}\right)^2 - S\right)\delta(f)\\ &= 0.\end{aligned} \tag{3.34}$$

The result in (3.34) shows that $S_Y(f)$ has no discrete component at $f = 0$ and it is a continuous function of f as it was expected due to symmetry in SP-LOCO codes.

Since S_Y is written in terms of S_X, the only thing left is converting the sequence into the writing signal $W(t)$ as it was explained in (2.13).

$$S_W(f) = \text{sinc}^2(\pi f) S_Y(f). \tag{3.35}$$

After obtaining S_W in terms of S_X, the method given in [8] and described in detail in Subsection 2.2.1 can be applied.

The first step is creating an FSTD. The non-binary FSTD representation is given in Figure 3.1. As discussed, SP-LOCO codes are actually $\mathcal{SC}^2_{m,1}$ constrained codes, which were described in detail in Section 2.1. Therefore, the binary FSTD given before applies here also. Note that the states represent the last generated 2 binary bits, and grey-colored states are the ones where the latest bit is a 1 in Figure 3.2.

The probabilities given on the edges of Figure 3.2 represent the maxentropic probabilities. The computation details can be found in [72]. The computed values are as

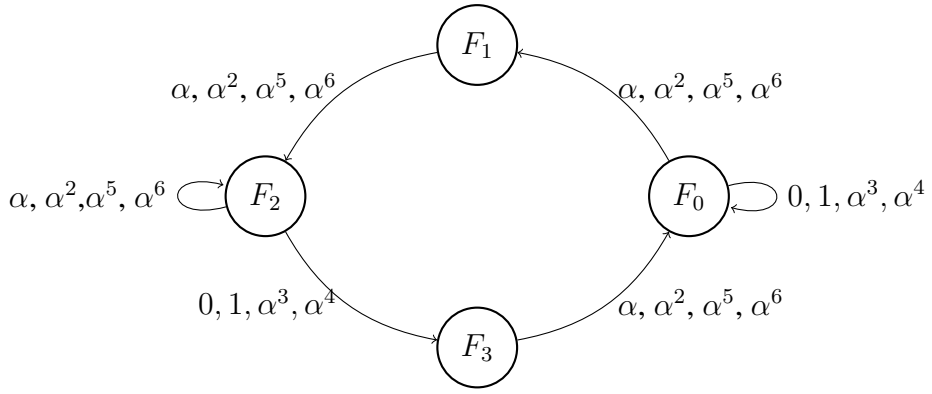

Figure 3.1: FSTD for SP-LOCO codes that have infinite length, defined over $\mathrm{GF}(8)$ and prevent PIS patterns.

Figure 3.2: (a) An FSTD that represents an SP-LOCO constrained sequence, (b) The same FSTD with transition probabilities on the edges.

follows:

$$\mathbf{V} = \begin{bmatrix} v_{0,0} & v_{0,1} & v_{0,2} & v_{0,3} \\ v_{1,0} & v_{1,1} & v_{1,2} & v_{1,3} \\ v_{2,0} & v_{2,1} & v_{2,2} & v_{2,3} \\ v_{3,0} & v_{3,1} & v_{3,2} & v_{3,3} \end{bmatrix} = \begin{bmatrix} 0.618 & 0.382 & 0 & 0 \\ 0 & 0 & 1 & 0 \\ 0 & 0 & 0.618 & 0.382 \\ 1 & 0 & 0 & 0 \end{bmatrix} \tag{3.36}$$

Observe that $v_{0,0} = v_{2,2}$ and $v_{0,1} = v_{2,3}$. Now, the FSTD needs to be converted into an OSTD as explored in detail in Subsection 2.2.1.

Then, using the OSTD given in Figure 3.3, OSTM can be constructed as follows using (2.4):

$$\mathbf{G}(D) = \begin{bmatrix} 0 & D \\ \alpha & \beta \end{bmatrix}, \tag{3.37}$$

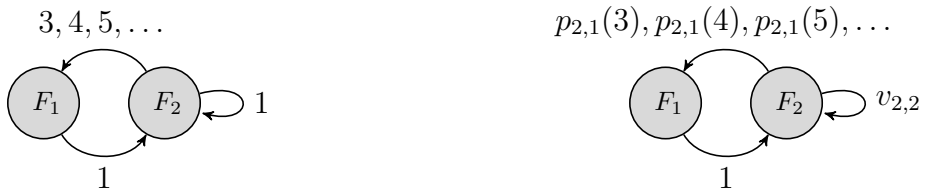

(a) (b)

Figure 3.3: (a) OSTD that is formed considering the FSTD of SP-LOCO codes where the numbers represent the run-lengths, (b) OSTD with transition probabilities on the edges for infinite-length SP-LOCO constrained sequence where $p_{i,j}(t)$ as represented in (2.4) and $p_{2,1}(3) = v_{2,3} \cdot v_{0,1}$, $p_{2,1}(4) = v_{2,3} \cdot v_{0,1} \cdot v_{0,0}$, $p_{2,1}(5) = v_{2,3} \cdot v_{0,1} \cdot v_{0,0}^2$.

$$\alpha = v_{2,3} v_{0,1} D^3 \sum_{k=0}^{\infty} (v_{0,0} D)^k = \frac{v_{0,1}^2 D^3}{1 - v_{0,0} D}, \tag{3.38}$$

$$\beta = v_{2,2} D = v_{0,0} D. \tag{3.39}$$

Finally, with (3.37) obtained above, the PSD $S_X(D)$ can be obtained through the method defined in (2.7).

3.3 Results

This section compares the theoretical result obtained for the PSD from the above discussion with the actual non-binary sequence's PSD, which is calculated conventionally. The non-binary sequences are generated via extensive MC simulations with 10^7 elements.

It is seen from Figure 3.4 that the theoretical results match the experimental results perfectly, which is the expected result since 2 distinct levels exist, making the problem binary. Nonetheless, this result serves as a trivial check for the theorem developed. Further inspection at different physical levels is also presented.

It is seen from Figure 3.5 that the theoretical results match the experimental results perfectly with 1 physical level differentiation. The magnitude increase compared to Figure 3.4 was expected since the voltage levels are increased.

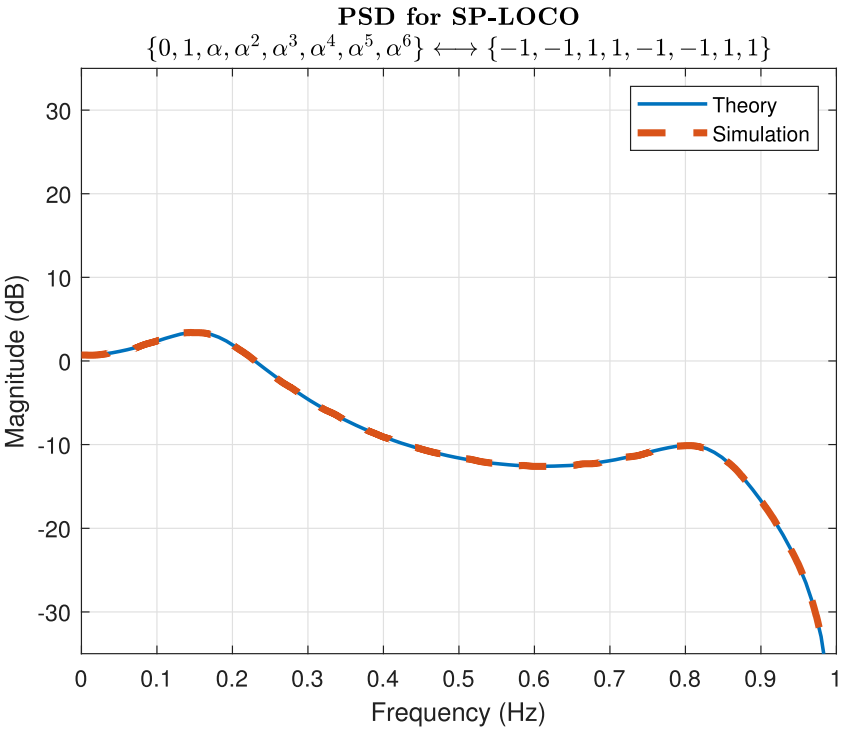

Figure 3.4: PSD for SP-LOCO, all the physical levels are the same.

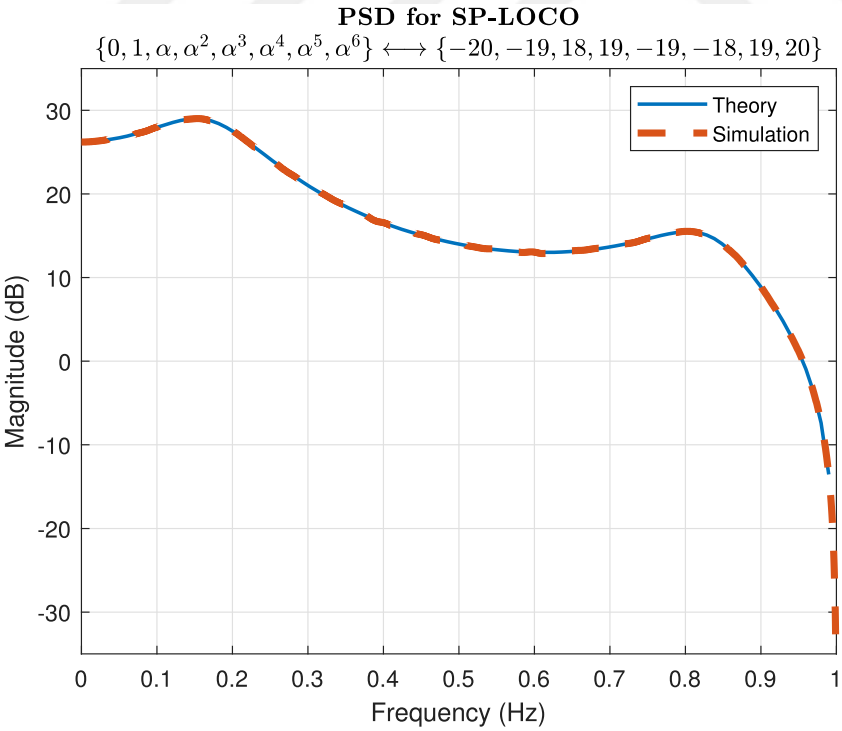

Figure 3.5: PSD for SP-LOCO, the physical levels are 1 level apart.

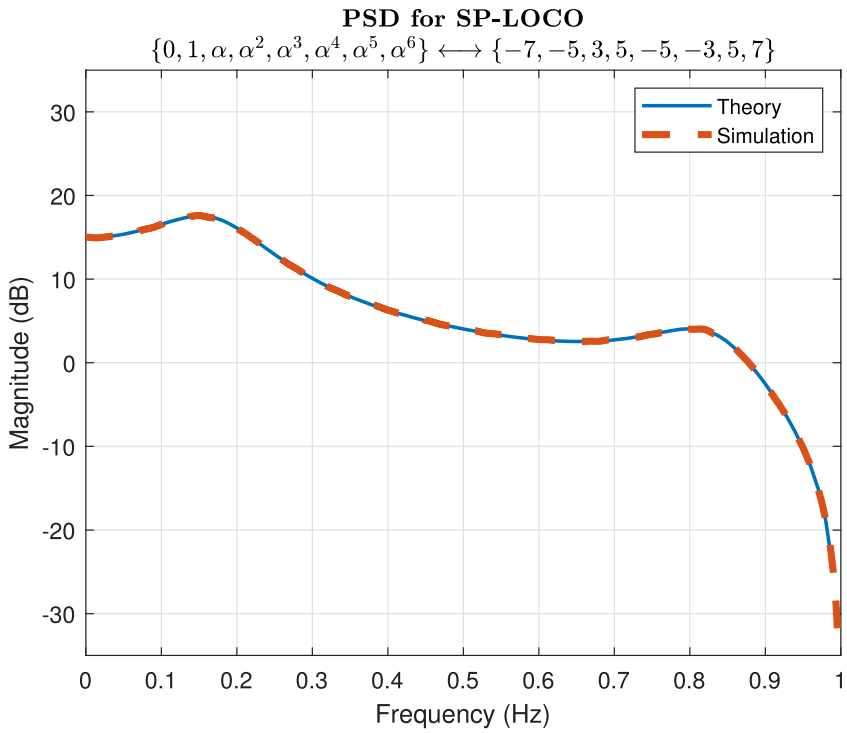

Figure 3.6: PSD for SP-LOCO, the physical levels are 2 levels apart.

It is seen from Figure 3.6 that the theoretical results match the experimental results perfectly with 2 physical level differentiation. The magnitude decrease compared to Figure 3.4 was expected since the voltage levels are decreased.

It is seen from Figure 3.7 that the theoretical results match the experimental results perfectly with 4 physical level differentiation. These different voltage read levels presented in Figure 3.5, Figure 3.6, and Figure 3.7 show that the theoretical derivation is correct and can be applied with any voltage level considering the baseline properties of the physical level mapping from the $\mathrm{GF}(8)$ symbols, which are $a_0 > a_1 > a_2 > a_3 > 0$.

Now, the possible effects of the assumption made for the equivalence between the symbols belonging to the same set, 3-tuples having the first or the third track bits in complementary sign with respect to the middle track, will be inspected by setting a_1 and a_2 levels differently in two possible cases.

It is seen from Figure 3.8 that the theoretical results match the experimental results

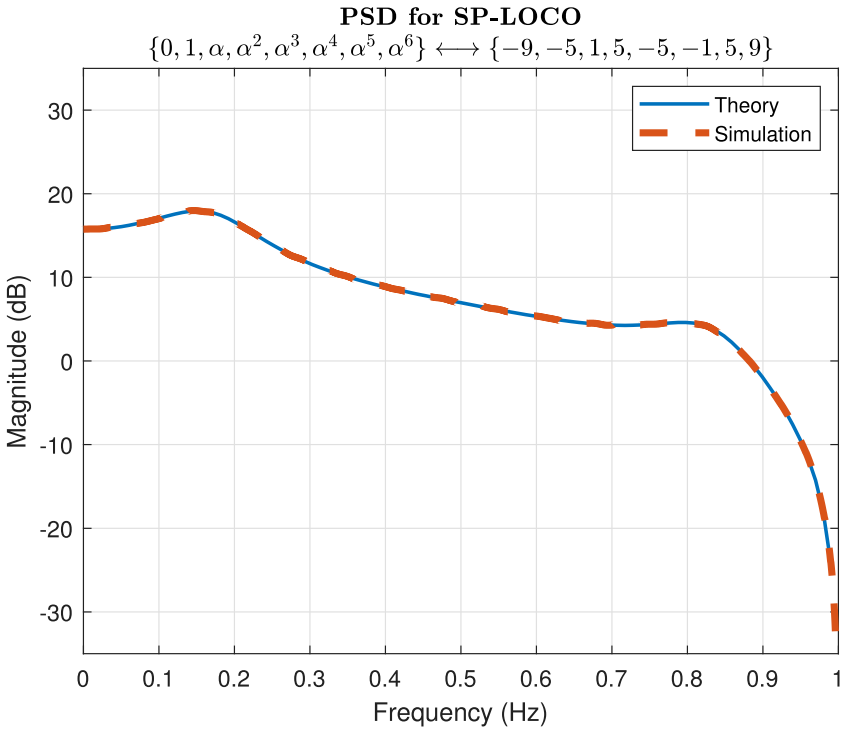

Figure 3.7: PSD for SP-LOCO, the physical levels are 4 levels apart.

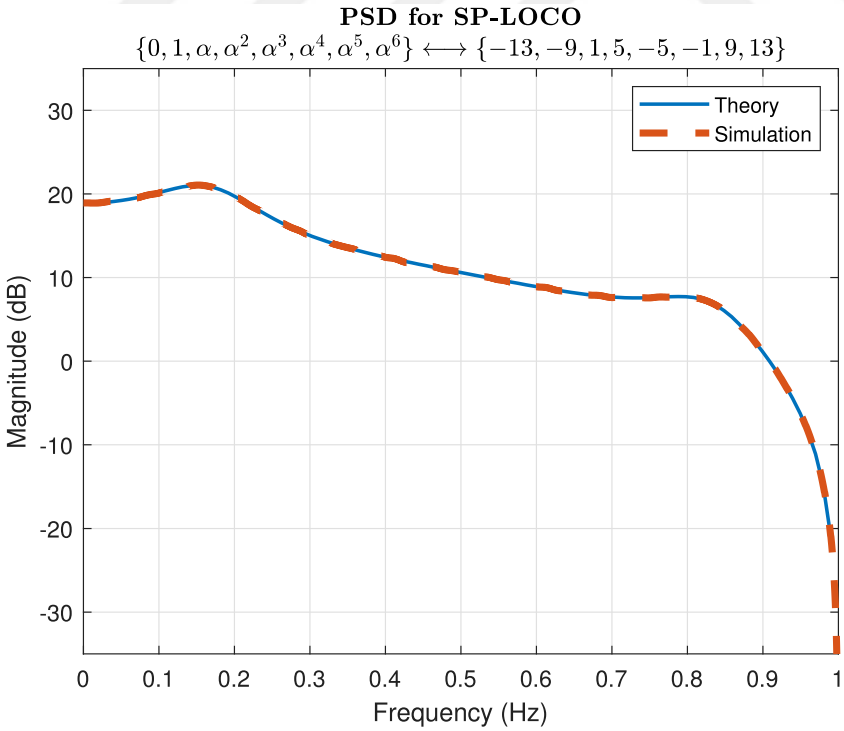

Figure 3.8: PSD for SP-LOCO, the physical levels are 4 levels apart, $a_1 > a_2$.

perfectly when different physical levels are defined for a_1 and a_2.

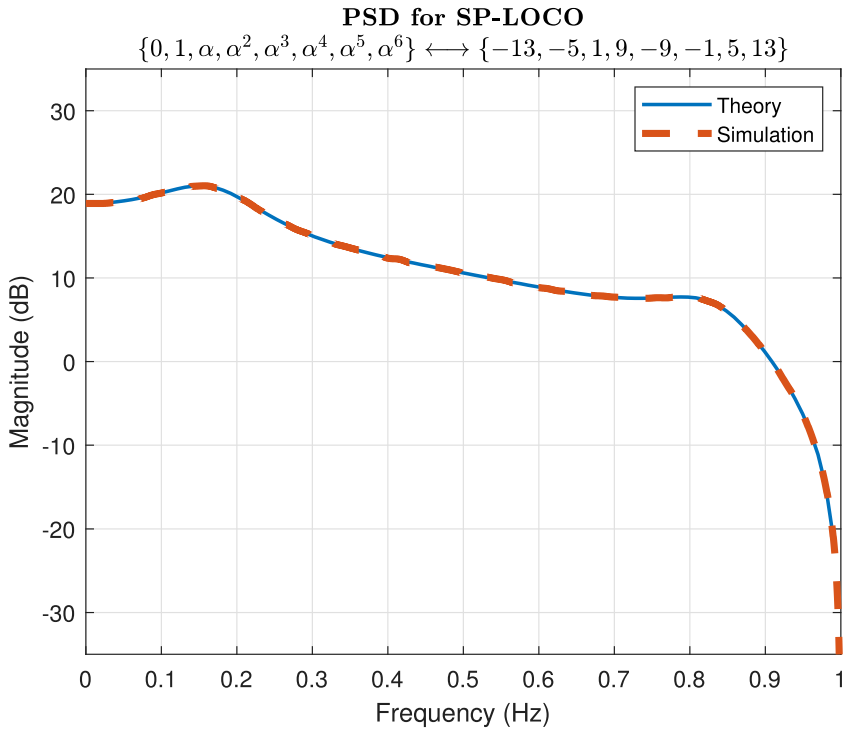

Figure 3.9: PSD for SP-LOCO, the physical levels are 4 levels apart, $a_2 > a_1$.

It is seen from Figure 3.9 that the theoretical results match the experimental results perfectly when different physical levels are defined for a_1 and a_2 in the reverse direction.

In another setting where the inference is not restricted in the 3×3 grid alone and further detrimental patterns are considered, infinite SP-LOCO codes with $x = 2$ can be used where the forbidden set $\mathcal{T}$ is defined as follows:

$$\begin{aligned}\mathcal{T} &\triangleq \{010, 101, 0110, 1001\}, \\ &= \Big\{\hat{\beta}_1\beta_2\tilde{\beta}_2\bar{\beta}_1, \hat{\beta}_2\bar{\beta}_1\tilde{\beta}_1\bar{\beta}_2, \forall\hat{\beta}_1, \bar{\beta}_1, \tilde{\beta}_1, \beta_1 \in \{0, 1, \alpha^3, \alpha^4\} \\ &\quad \text{and} \quad \forall\hat{\beta}_2, \bar{\beta}_2, \tilde{\beta}_2, \beta_2 \in \{\alpha, \alpha^2, \alpha^5, \alpha^6\}\Big\}. \end{aligned} \tag{3.40}$$

As the TDMR device ages, horizontal transitions should be further separated to give the read head enough time to respond and mitigate interference even more. This is not necessarily the typical case in TDMR systems as the focus is mostly on 3×3 grids [34], but the results of such a case are offered for the interested reader. The details

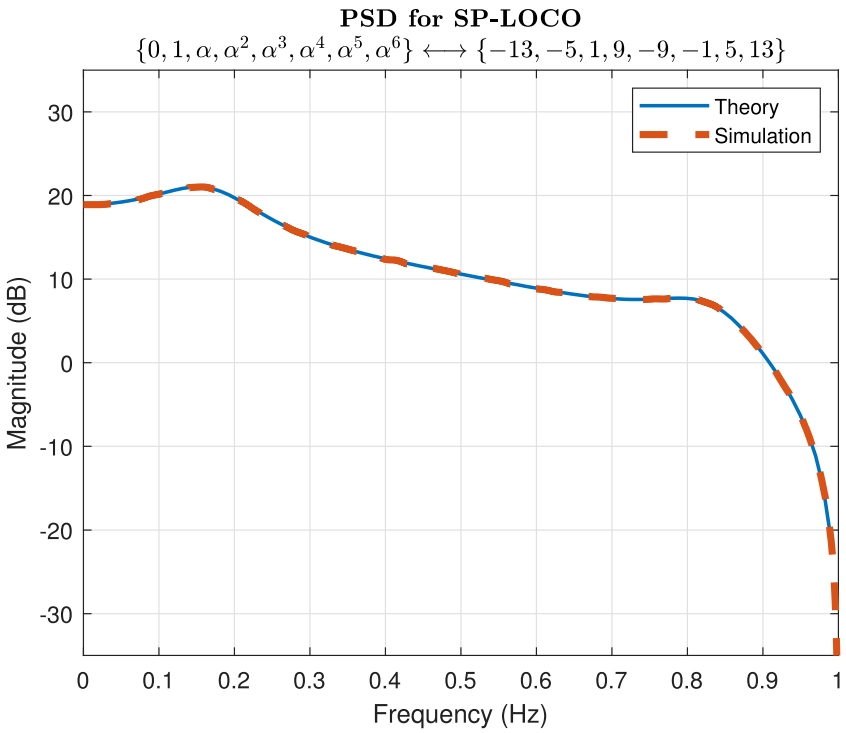

Figure 3.10: PSD for SP-LOCO, the physical levels are 4 levels apart, $a_2 > a_1$.

of finding the power spectra of SP-LOCO codes with $x = 2$, which are actually $\mathcal{S}_2$ constrained codes, can be found in [8].

Acknowledgments

The contributions made by Assist. Prof. Ahmed Hareedy and Kaan Büyükkalaycı were instrumental in completing this section.

CHAPTER 4

PSD FOR MULTI-LEVEL CONSTRAINED CODES: QA-LOCO CODES

This chapter introduces the mapping concept for the theoretical derivation of multi-level constrained codes. It demonstrates its application to QA-LOCO codes, where the multi-level sequence is first mapped into three distinct binary sequences. Through algorithmic manipulations, its power spectral density (PSD) is represented in terms of these binary sequences, utilizing the derivation from Chapter 4 directly.

4.1 QA-LOCO Codes

With the recent advancements in physics, Flash devices can store more than one bit per cell, and the advancements in signal processing have helped the effect of physical instabilities [28]. These improvements laid the groundwork for the growth of the use of the multi, triple, quad, and penta-level cell (M/T/Q/P-LC) Flash memory devices, which can be considered a necessity in this age of information [28].

Hareedy et al. [28] introduce simple constrained codes for Flash memory devices named QA-LOCO codes, that are suitable for the non-binary physical gates in the M/T/Q/P-LC Flash memory devices and any future Flash memory that has q levels per cell. QA-LOCO codes belong to the general family of LOCO codes, which was introduced to the reader in the preliminaries section. They subsume the previously designed asymmetric LOCO (A-LOCO) codes for SLC Flash memory devices and extend the application to the non-binary world in parallel with the recent developments in technology while preserving the important features of the family of LOCO codes such as capacity-achieving rates, affordable encoding-decoding complexity, and ease of reconfigurability [28]. The main objective of designing the codes for Flash mem-

ory devices is to mitigate inter-cell inference since it is a massive source of error in Flash devices [33]. It is also known that as the device ages, the number of error-prone patterns increases [33]. While the reconfigurability of a coding scheme is a desirable quality in general [4], it becomes even more crucial for Flash devices, making the usage of QA-LOCO codes in Flash devices more desirable.

The definition of QA-LOCO codes will be given, directly referencing the work of Hareedy et al. [28]. Denote a Galois field of size q by $\mathrm{GF}(q)$ where α is a primitive element of the field.

$$\mathrm{GF}(q) \triangleq \{0, 1, \alpha, \alpha^2, \ldots, \alpha^{q-2}\}. \tag{4.1}$$

Even though the analysis for QA-LOCO codes works for any GF of size q, q can be particularized as 2^v where $v \geq 1$ because, for a Flash device that has v bits per cell, there exist $q = 2^v$ levels [28].

Define δ and δ_i for any i, as elements in $\mathrm{GF}(q) \backslash \{\alpha^{q-2}\}$ and define $\delta_d^r \triangleq \delta_{r-1}\delta_{r-2}\cdots\delta_m$ as a sequence in $[\mathrm{GF}(q) \setminus \{\alpha^{q-2}\}]^r$, with $\delta_d^1 = \delta_m = \delta$.

Then, for a QA-LOCO $QC_{m,x}^q$ with $q \geq 2$, $m \geq 1$, and $x \geq 1$ that has its symbols in $\mathrm{GF}(q)$, the set of forbidden patterns, $\mathcal{T}$, can be defined as [31]:

$$\mathcal{T} = Q_x^q \triangleq \{\alpha^{q-2}\delta^\tau\alpha^{q-2},\ \forall \delta_d^\tau \in [\mathrm{GF}(q) \setminus \{\alpha^{q-2}\}]^\tau \mid 1 \leq \tau \leq x\}. \tag{4.2}$$

For the following discussions, charge levels are directly translated to threshold voltage levels that are defined by their indices for simplicity [28]. Defining the set of charge levels equivalent to $\mathrm{GF}(q)$ is $0, 1, 2, \ldots, q-1$, the set of charge-level patterns equivalent to Q_x^q becomes:

$$\{(q-1)\mu_0(q-1), (q-1)\mu_1\mu_0(q-1), \ldots, (q-1)\mu_{x-1}\mu_{x-2}\cdots\mu_0(q-1)\}. \tag{4.3}$$

where $\mu_i \in \{0, 1, \ldots, q-2\}$. Note that charge levels will be used to represent the symbols for the sake of simplicity.

4.2 Theoretical Derivation of PSD for QA-LOCO Codes

A QA-LOCO code [28], $QC_{m,x}^q$, is a finite length constrained code with length m. However, the PSD derivation will be provided for infinite-length QA-LOCO codes.

From now on, infinite length QA-LOCO codes will be simply referred to as QA-LOCO codes, and they will be denoted as Q_x^q with $q \geq 2$, and $x \geq 1$ and the set of forbidden patterns given in (4.2) still applies. Also, note that QA-LOCO codes also use level-based signaling, making it possible to apply the method given in [8] to the binary signal derived after necessary mapping.

The main idea behind the derivation is connecting the binary problem solution to the non-binary problem setup. Considering the forbidden set of patterns given in (4.2), it can be observed that the first and last symbols are α^{q-2}, the highest level symbol. The symbols in between the two highest level symbols are grouped together and belong to the set $\mathrm{GF}(q) \setminus \{\alpha^{q-2}\}$ and no matter which one they are, they are treated as equally important to forbid, which will eventually lead each symbol having the same probability of being generated. In short, it can be claimed that for the non-binary problem, there also exist two sets of symbols which are named as the highest level symbol, α^{q-2}, and the low-level symbols, $\delta \in \mathrm{GF}(q) \setminus \{\alpha^{q-2}\}$. In terms of charge levels and the simplification mentioned, the highest charge level becomes $(q-1)$, and the low charge levels become $\mu_i \in \{0, 1, \ldots, q-2\}$.

Remember that in the binary case with A-LOCO codes [54], the high-level symbol was represented as a 1, and the low-level symbol was represented as a 0, which led to the forbidden pattern set:

$$\mathcal{T} = \mathcal{A}_x \triangleq \{101, 1001, \ldots, 10^x1\} \tag{4.4}$$

Since the two sets of levels and charges in the non-binary problem are analogous to the binary problem as discussed, the highest level charge $(q-1)$ can be mapped to 1, and any member from the low-level charges, $\mu_i \in \{0, 1, \ldots, (q-2)\}$, can be mapped to 0. Hence, the problem is reduced to an algebraic manipulation for this binary mapping.

Let $\{Y_n\}$ be the stream of charge levels of the symbols, which is the original charge level sequence that $Y_n \in \{0, 1, \ldots, (q-1)\}$.

Then, let $\{X_n\}$ be the stream of bits mapped according to the charge levels of the symbols, which is the baseline mapping, and $X_n \in \{0, 1\}$. The sequence $\{X_n\}$ can

be defined as follows:

$$X_n = \begin{cases} 1, & \text{if } Y_n = (q-1), \\ 0, & \text{else.} \end{cases} \tag{4.5}$$

In order to simplify the expressions and improve the readability of the equations, the following notations will be used throughout the derivation:

$$\begin{aligned} p_{00} &= \mathbb{P}[X_0 = 0, X_k = 0], \\ p_{01} &= \mathbb{P}[X_0 = 0, X_k = 1], \\ p_{10} &= \mathbb{P}[X_0 = 1, X_k = 0], \\ p_{11} &= \mathbb{P}[X_0 = 1, X_k = 1]. \end{aligned} \tag{4.6}$$

The auto-correlation function of $\{X_n\}$ can be written as follows:

$$\mathbb{R}(X) = \mathbb{E}[X_0 X_k] = 0 \cdot 0 \cdot p_{00} + 0 \cdot 1 \cdot p_{01} + 1 \cdot 0 \cdot p_{10} + 1 \cdot 1 \cdot p_{11} = p_{11}. \tag{4.7}$$

Before exploring the auto-correlation function of $\{Y_n\}$, the charge level probabilities of Y_n will be inspected using the total probability theorem.

Define $a_m, a_n \in= \{0, 1, \ldots, q-2\}$ and $x_0, x_k \in \{0, 1\}$. The charge level probabilities will be derived case by case.

$$\begin{aligned} p_{LL} &= \mathbb{P}[Y_0 = a_m, Y_k = a_n] \\ &= \sum_{x_0} \sum_{x_k} \mathbb{P}[Y_0 = a_m, Y_k = a_n \mid X_0 = x_0, X_k = x_k] \cdot \mathbb{P}[X_0 = x_0, X_k = x_k] \\ &= \mathbb{P}[Y_0 = a_m, Y_k = a_n \mid X_0 = 0, X_k = 0] \cdot p_{00} \\ &= \mathbb{P}[Y_0 = a_m \mid X_0 = 0] \cdot \mathbb{P}[Y_k = a_n \mid X_k = 0] \cdot p_{00} \\ &= \frac{p_{00}}{(q-1)^2} \end{aligned} \tag{4.8}$$

$$\begin{aligned} p_{LH} &= \mathbb{P}[Y_0 = a_m, Y_k = (q-1)] \\ &= \sum_{x_0} \sum_{x_k} \mathbb{P}[Y_0 = a_m, Y_k = a_n \mid X_0 = x_0, X_k = x_k] \cdot \mathbb{P}[X_0 = x_0, X_k = x_k] \\ &= \mathbb{P}[Y_0 = a_m, Y_k = (q-1) \mid X_0 = 0, X_k = 1] \cdot p_{01} \\ &= \mathbb{P}[Y_0 = a_m \mid X_0 = 0] \cdot \mathbb{P}[Y_k = (q-1) \mid X_k = 1] \cdot p_{01} \\ &= \frac{p_{01}}{(q-1)} \end{aligned} \tag{4.9}$$

$$
\begin{aligned}
p_{HL} &= \mathbb{P}[Y_0 = (q-1), Y_k = a_n] \\
&= \sum_{x_0} \sum_{x_k} \mathbb{P}[Y_0 = a_m, Y_k = a_n \mid X_0 = x_0, X_k = x_k] \cdot \mathbb{P}[X_0 = x_0, X_k = x_k] \\
&= \mathbb{P}[Y_0 = (q-1), Y_k = a_n \mid X_0 = 1, X_k = 0] \cdot p_{10} \\
&= \mathbb{P}[Y_0 = (q-1) \mid X_0 = 1] \cdot \mathbb{P}[Y_k = a_n \mid X_k = 0] \cdot p_{10} \\
&= \frac{p_{10}}{(q-1)}
\end{aligned} \tag{4.10}
$$

$$
\begin{aligned}
p_{HH} &= \mathbb{P}[Y_0 = (q-1), Y_k = (q-1)] \\
&= \sum_{x_0} \sum_{x_k} \mathbb{P}[Y_0, Y_k = (q-1) \mid X_0 = x_0, X_k = x_k] \cdot \mathbb{P}[X_0 = x_0, X_k = x_k] \\
&= \mathbb{P}[Y_0, Y_k = (q-1) \mid X_0 = 1, X_k = 1] \cdot p_{11} \\
&= \mathbb{P}[Y_0 = (q-1) \mid X_0 = 1] \cdot \mathbb{P}[Y_k = (q-1) \mid X_k = 1] \cdot p_{11} \\
&= p_{11}
\end{aligned} \tag{4.11}
$$

Now, the auto-correlation function of $\{Y_n\}$ can be written as for $k \neq 0$:

$$
\begin{aligned}
\mathbb{R}(Y) = \mathbb{E}[Y_0 Y_k] &= \sum_{a_m=0}^{q-2} \sum_{a_n=0}^{q-2} a_m \cdot a_n \cdot p_{LL} + \sum_{a_m=0}^{q-2} a_m \cdot (q-1) \cdot p_{LH} \\
&\quad + \sum_{a_n=0}^{q-2} (q-1) \cdot a_n \cdot p_{HL} + (q-1)^2 \cdot p_{HH} \\
&= \sum_{a_m=0}^{q-2} \sum_{a_n=0}^{q-2} a_m \cdot a_n \cdot \frac{p_{00}}{(q-1)^2} + \sum_{a_m=0}^{q-2} a_m \cdot (q-1) \cdot \frac{p_{01}}{(q-1)} \\
&\quad + \sum_{a_n=0}^{q-2} (q-1) \cdot a_n \cdot \frac{p_{10}}{(q-1)} + (q-1)^2 \cdot p_{11} \\
&= \left(\frac{q-2}{2}\right)^2 \cdot p_{00} + \frac{(q-1)(q-2)}{2} \cdot (p_{01} + p_{10}) + (q-1)^2 \cdot p_{11}.
\end{aligned} \tag{4.12}
$$

Since the ultimate goal is to express (4.12) in terms of (4.7), the probabilities p_{00} and $(p_{01} + p_{10})$ also needs to be expressed in terms of (4.7). For this purpose, the sub-signal $\{Z_n\}$ is defined as follows:

$$
Z_n = \begin{cases} 0, & \text{if } Z_n = (q-1), \\ 1, & \text{else.} \end{cases} \tag{4.13}
$$

Notice that Z_n is defined in an antagonistic manner, and the following observations can be made about Z_n:

$$\begin{aligned}
\mathbb{P}[Z_0 = 0, Z_k = 0] &= \mathbb{P}[X_0 = 1, X_k = 1] = p_{11}, \\
\mathbb{P}[Z_0 = 0, Z_k = 1] &= \mathbb{P}[X_0 = 1, X_k = 0] = p_{10}, \\
\mathbb{P}[Z_0 = 1, Z_k = 0] &= \mathbb{P}[X_0 = 0, X_k = 1] = p_{01}, \\
\mathbb{P}[Z_0 = 1, Z_k = 1] &= \mathbb{P}[X_0 = 0, X_k = 0] = p_{00}.
\end{aligned} \tag{4.14}$$

Using (4.14), the auto-correlation function of $\{Z_n\}$ can be written as follows:

$$\mathbb{E}[Z_0 Z_k] = 0 \cdot 0 \cdot p_{11} + 0 \cdot 1 \cdot p_{10} + 1 \cdot 0 \cdot p_{01} + 1 \cdot 1 \cdot p_{00} = p_{00}. \tag{4.15}$$

Benefiting, $Z_n = 1 - X_n$, which is a linear relation, Z_n and X_n will be related together. Denoting the equilibrium probability of a 1 in $\{X_n\}$ as $p(1)$, the following expression is obtained:

$$\mathbb{E}[Z_0 Z_k] = \mathbb{E}[(1 - X_0)(1 - X_k)] = \mathbb{E}[X_0 X_k] - 2p(1) + 1 = p_{00}. \tag{4.16}$$

Now, the only term left to be expressed in terms of (4.7) is $(p_{01} + p_{10})$. For this, the unit measure axiom of the probability can be used:

$$\sum_{x_0} \sum_{x_k} \mathbb{P}[X_0 = x_0, X_k = x_k] = p_{00} + p_{01} + p_{10} + p_{11} = 1. \tag{4.17}$$

Using (4.7), (4.16) and (4.17),

$$\begin{aligned}
p_{01} + p_{10} &= 1 - p_{00} - p_{11} \\
&= 1 - (\mathbb{E}[X_0 X_k] - 2p(1) + 1) - \mathbb{E}[X_0 X_k] \\
&= 2p(1) - 2\mathbb{E}[X_0 X_k].
\end{aligned} \tag{4.18}$$

With all the needed terms expressed in terms of $\mathbb{E}[X_0 X_k]$, the main equation $\mathbb{E}[Y_0 Y_k]$

can be rewritten and rearranged using (4.7), (4.12) and (4.16) where $k \neq 0$ as follows:

$$\begin{aligned}
\mathbb{E}[Y_0 Y_k] &= \left(\frac{q-2}{2}\right)^2 \cdot p_{00} + \frac{(q-1)(q-2)}{2} \cdot (p_{01} + p_{10}) + (q-1)^2 \cdot p_{11} \\
&= \left(\frac{q-2}{2}\right)^2 \cdot (\mathbb{E}[X_0 X_k] - 2p(1) + 1) \\
&\quad + \frac{(q-1)(q-2)}{2} \cdot (2p(1) - 2\mathbb{E}[X_0 X_k]) \\
&\quad + (q-1)^2 \cdot \mathbb{E}[X_0 X_k] \\
&= \frac{q^2}{4} E[X_0 X_k] + \frac{1}{2} q(q-2)p(1) + \frac{1}{4}(q-2)^2, \quad k \neq 0.
\end{aligned} \tag{4.19}$$

Note that the result in 4.19 is found by using the total probability theorem. The high symbol gives the value of itself, and the low symbols give the average value of them since they are equiprobable.

The theoretical derivation given step by step above treats any lag k as equivalent and computes the necessary probabilities accordingly. However, lag at 0, $k = 0$, should be handled differently. Without discrediting the original derivation since it is true for $k \neq 0$ and it is described this way from the start, via performing subtraction and addition for the term at lag 0, the true result can be achieved. The reason for this difference is, for any k, it is assumed that the charge levels Y_0 and Y_k could be different, and a joint probability would be considered. This is not the case for $k = 0$ since Y_0 and Y_k becomes the same charge level, and only the probability of $\mathbb{P}[Y_0]$ should be considered.

From the sum of probabilities defined in (4.6) only the manipulations involving p_{00} is erroneous for the term at lag 0. Because for p_{01} and p_{10}, Y_0 and Y_k are already defined as different charge levels, and for p_{11}, Y_0 and Y_k are already defined as the same charge level, which is $(q-1)$.

The general conclusions given in Section 3.2 apply here also since $\mathbb{R}_Y(k)$ is defined as follows, which can be considered analogous to (3.22):

$$\mathbb{R}_Y(k) = \begin{cases} \frac{q^2}{4}\mathbb{R}_X(k) + \frac{1}{2}q(q-2)p(1) + \frac{1}{4}(q-2)^2, & \text{if } k \neq 0, \\ \mathbb{R}_Y(0), & \text{if } k = 0. \end{cases} \tag{4.20}$$

Then, respective a and b constants for (4.20) can be written considering (3.21) as

follows:

$$a = \frac{q^2}{4},$$
$$b = \frac{1}{2}q(q-2)p(1) + \frac{1}{4}(q-2)^2. \tag{4.21}$$

Then, using the definitions in (3.24) the following expressions can be written:

$$\begin{aligned}
\text{Addition} &= \mathbb{R}_Y(0) = \mathbb{E}[Y_n^2] \\
&= p(1)(q-1)^2 + \frac{\big(1-p(1)\big)}{(q-1)} \sum_{y_n=0}^{q-2} y_n^2 \\
&= p(1)(q-1)^2 + \frac{\big(1-p(1)\big)}{(q-1)} \sum_{y_n=0}^{q-2} y_n^2 \\
&= p(1)(q-1)^2 + \frac{\big(1-p(1)\big)(q-2)(2q-3)}{6} \\
&= \frac{p(1)\cdot(4q^2-5q)}{6} + \frac{(2q^2-7q+6)}{6},
\end{aligned} \tag{4.22}$$

$$\begin{aligned}
\text{Subtraction} &= a\mathbb{R}_X(0) + b \\
&= \frac{q^2}{4}\mathbb{E}[X_n^2] + \frac{1}{2}q(q-2)p(1) + \frac{1}{4}(q-2)^2 \\
&= \frac{q^2}{4}p(1) + \frac{1}{2}q(q-2)p(1) + \frac{1}{4}(q-2)^2, \\
&= \frac{p(1)\cdot(3q^2-4q)}{4} + \frac{(q-2)^2}{4},
\end{aligned} \tag{4.23}$$

$$\begin{aligned}
\text{Correction} &= \text{Addition} - \text{Subtraction}, \\
&= \frac{p(1)\cdot(4q^2-5q)}{6} + \frac{(2q^2-7q+6)}{6} - \frac{p(1)\cdot(3q^2-2q)}{4} - \frac{(q-2)^2}{4} \\
&= \frac{p(1)\cdot(-q^2+2q)}{12} + \frac{(q^2-2q)}{12} \\
&= \frac{\big(1-p(1)\big)q(q-2)}{12},
\end{aligned} \tag{4.24}$$

$$\begin{aligned}
S_Y(f) &= aS_X(f) + b\delta(f) + \text{Correction} \\
&= \frac{q^2}{4}\cdot S_X(f) + \left(\frac{2q(q-2)p(1)+(q-2)^2}{4}\right)\cdot\delta(f) + \frac{\big(1-p(1)\big)q(q-2)}{12}.
\end{aligned} \tag{4.25}$$

Note that the correction term in (4.25) is a constant, not a Dirac delta function. The reason why it was simply added is that it covers the zero lag's effect when multiplied with $e^{i2\pi kf}$, which is 1 for $k = 0$.

Now, the second general conclusion obtained in (3.27) can be inspected as follows for finding the area of the Dirac delta function in $S_Y(f)$ where $S_Y^d(f)$ represents the discrete part of the spectra:

$$\begin{aligned} S_Y^d(f) &= \mathbb{E}^2[Y_n]\delta(f) \\ &= \left[p(1)(q-1) + \frac{(1-p(1))}{(q-1)} \sum_{y_n=0}^{q-2} y_n\right]^2 \delta(f) \\ &= \left[p(1)(q-1) + \frac{\big(1-p(1)\big)(q-2)}{2}\right]^2 \delta(f) \\ &= \left[\frac{qp(1) + (q-2)}{2}\right]^2 \delta(f) \end{aligned} \tag{4.26}$$

Remember that according to (3.27), in order to have a zero discrete part in power spectra, the area of the Dirac delta function computed in (4.26) should be equal to zero. Since the resultant term is a squared expression, only the nominator can be inspected. For the nominator to be zero $p(1)$, the steady state probability of obtaining a 1 in $\{X_n\}$, should be equal to $-\frac{q-2}{q}$. Remember that q here represents the number of levels in a Flash cell, which is known as $q \geq 2$. For $q = 2$, $p(1)$ should also be equal to zero to satisfy the condition. Note that for $q = 2$ there exists 2 levels as 0 and 1, which makes the actual sequence $\{Y_n\}$ equal to $\{X_n\}$. This choice is not applicable since $p(1) = 0$ implies that the generated sequence will be a stream of 0's, and there will be no clue to distinguish if a coded symbol is a 0 or 1. For $q > 2$, the expression will be equal to a negative number between -1 and 0, and this case is also improbable since any probability is greater than or equal to 0. Therefore, there exists a discrete component in $S_Y(f)$ with an area of $\left[\frac{qp(1)+(q-2)}{2}\right]^2$ at $f = 0$ as it was expected since QA-LOCO codes are not symmetric.

Now that $S_Y(f)$ is represented in terms of $S_X(f)$, the writing signal needs to be formed as suggested in (2.13):

$$S_W(f) = \text{sinc}^2(\pi f) S_Y(f) \tag{4.27}$$

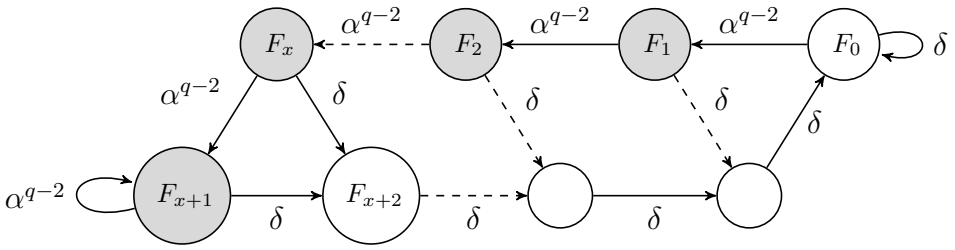

Figure 4.1: FSTD for infinite-length $\mathcal{Q}_x^q$-constrained sequence. Here, $\delta_i \in \mathrm{GF}(q) \setminus \{\alpha^{q-2}\}$ for any i and $\delta_i = \delta$ for simplicity. Note that the symbol α^{q-2} represents the highest level. Dashed lines imply that the transition may be more than one state in length. Specifically, the diagonal dashed edges leaving state F_i contain $x - i$ states.

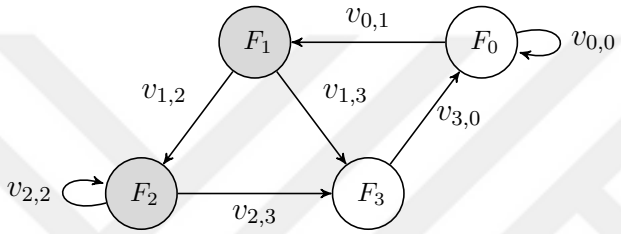

Figure 4.2: FSTD with maxentropic transition probabilities on the edges for infinite-length $\mathcal{Q}_1^q$-constrained sequence.

Now that the sequence is formed into its latest shape, and S_W is written in terms of the binary sequence S_X, the method described in Section 2.2 can be applied to S_x in order to obtain its PSD. For this purpose, first, an FSTD should be constructed for the non-binary problem, and its binary counterpart should be found. Then, the respective OSTD should be formed, after which the OSTM entries need to be written. However, for different values of x, the FSTD, OSTD, and OSTM size changes. Therefore, a parametric discussion and examples for $x = 1$ and $x = 2$ will be provided for the related steps.

Figure 4.1 shows a non-binary FSTD constructed for QA-LOCO codes with different x values. The maxentropic transition probabilities on the edges can be computed using the adjacency matrix of the FSTD given in Figure 4.1 and the method given in [72].

Instead of providing a parametric adjacency matrix for the FSTD in Figure 4.1, the

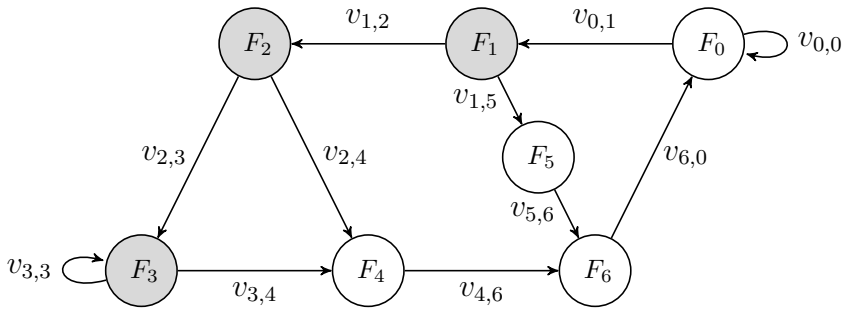

Figure 4.3: FSTD with maxentropic transition probabilities on the edges for infinite-length $\mathcal{Q}_2^q$-constrained sequence.

cases for $x = 1$ and $x = 2$ will be shown. Figure 4.2 shows the FSTD constructed for $x = 1$ case. The corresponding adjacency matrix is as follows:

$$\mathbf{A} = \begin{bmatrix} a_{0,0} & a_{0,1} & a_{0,2} & a_{0,3} \\ a_{1,0} & a_{1,1} & a_{1,2} & a_{1,3} \\ a_{2,0} & a_{2,1} & a_{2,2} & a_{2,3} \\ a_{3,0} & a_{3,1} & a_{3,2} & a_{3,3} \end{bmatrix} = \begin{bmatrix} q-1 & 1 & 0 & 0 \\ 0 & 0 & 1 & q-1 \\ 0 & 0 & 1 & q-1 \\ q-1 & 0 & 0 & 0 \end{bmatrix} \tag{4.28}$$

Figure 4.3 shows the FSTD constructed for $x = 2$ case. The corresponding adjacency matrix is as follows where the first element is $a_{0,0}$ and the last element is $a_{6,6}$:

$$\mathbf{A} = \begin{bmatrix} q-1 & 1 & 0 & 0 & 0 & 0 & 0 \\ 0 & 0 & 1 & 0 & 0 & q-1 & 0 \\ 0 & 0 & 0 & 1 & q-1 & 0 & 0 \\ 0 & 0 & 0 & 1 & q-1 & 0 & 0 \\ 0 & 0 & 0 & 0 & 0 & 0 & q-1 \\ 0 & 0 & 0 & 0 & 0 & 0 & q-1 \\ q-1 & 0 & 0 & 0 & 0 & 0 & 0 \end{bmatrix} \tag{4.29}$$

Using the FSTD given for non-binary sequence in Figure 4.1, the binary FSTD can be constructed using the same maxentropic transition probabilities. The maxentropic probabilities matrix $\mathbf{V}$ starts with element $v_{0,0}$ and the total size of the matrix is dependent on x. Note that the grey-colored states are the ones where the incoming transition is caused by the high-level symbol, which is α^{q-2}. The binary FSTD is

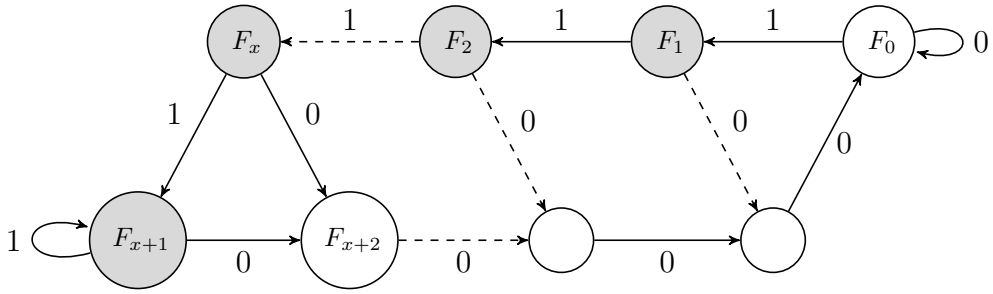

Figure 4.4: Binary FSTD with symbols 0 and 1 on the edges for infinite-length $\mathcal{Q}_x^q$-constrained sequence. Dashed lines imply that the transition may be more than one state in length. Specifically, the diagonal dashed edges leaving state F_i contain $x - i$ states.

shown in Figure 4.4. It is important to note that the FSTD presented is not minimal in the number of states since a fixed number of symbols are considered for a state. Therefore, maxentropic probabilities $v_{1,2} = v_{2,3} = v_{3,4} = \ldots = v_{x,x+1} = v_{x+1,x+1}$.

Then, an OSTD is constructed using 4.4, which would have $x + 1$ number of states. Finally, an OSTD of size $(x+1) \times (x+1)$ is formed with variables α and β as follows where $\mathbf{I}_x$ is the identity matrix of size $x \times x$:

$$\mathbf{G}(D) = \begin{bmatrix} \alpha & & \\ \vdots & & \beta D \mathbf{I}_x \\ \alpha & 0 \quad \cdots \quad 0 & \beta \end{bmatrix}, \tag{4.30}$$

$$\alpha = v_{0,1} v_{1,x+2} D^{x+2} \sum_{k=0}^{\infty} (v_{0,0} D)^k = \frac{v_{0,1} v_{1,x+2} D^{x+2}}{1 - v_{0,0} D}, \tag{4.31}$$

$$\beta = v_{1,2} D. \tag{4.32}$$

Finally, with (4.30) obtained above, the PSD $S_X(D)$ can be obtained through the method defined in (2.7).

4.3 Results

In this section, the theoretical result derived is plotted and compared with Monte Carlo simulations, where the sequence has 10^7 elements.

It is observed that the PSD expression obtained involves a delta function, which is placed at the frequency 0. In the following figures, this delta function will not be shown in the plots. However, the area of this discrete component at frequency 0 is equal to $\mathbb{E}^2[Y_n]$ and will be given in the discussion.

In a general sense, the parameter x in QA-LOCO represents the number of low voltage level symbols in between two high voltage level symbols in the forbidden pattern set [28]. Therefore, depending on the number of levels q and parameter x, the number of forbidden patterns changes.

4.3.1 Results for MLC

Results are as follows for multi-level cells that have 2 bits per cell and have a total of $q = 4$ levels per cell.

The discrete part of the PSD for Figure 4.5 is a Dirac delta function at $f = 0$ with an area of $\mathbb{E}^2[Y_n] = 1.928$. It is seen from Figure 4.5 that the theoretical results match the experimental results perfectly. In Figure 4.5, a different pattern is observed compared to an uncoded sequence's PSD, which would be the sinc function. Since $q = 4$, the overall shape of the PSD is distinct and observable.

The discrete part of the PSD for Figure 4.6 is a Dirac delta function at $f = 0$ with an area of $\mathbb{E}^2[Y_n] = 1.7429$. It is seen from Figure 4.6 that the theoretical results also match the experimental results perfectly. In Figure 4.6, the number of forbidden patterns is increased. Therefore, the pattern of the plot deviates more from one of an uncoded sequence's shape, and the shape is differed compared to Figure 4.5, and it is observable. Also, it can be observed that the peak of the graph has moved towards the left compared to Figure 4.5, which will be explained in detail later.

The discrete part of the PSD for Figure 4.7 is a Dirac delta function at $f = 0$ with an area of $\mathbb{E}^2[Y_n] = 1.622$. It is seen from Figure 4.7 that the theoretical results again match the experimental results perfectly. In Figure 4.7, the number of forbidden patterns is further increased. Therefore, compared to Figure 4.6, the plot has a different pattern and it is still observable. Also, it can be observed that the peak of the graph has moved towards left further compared to Figure 4.5 and Figure 4.6.

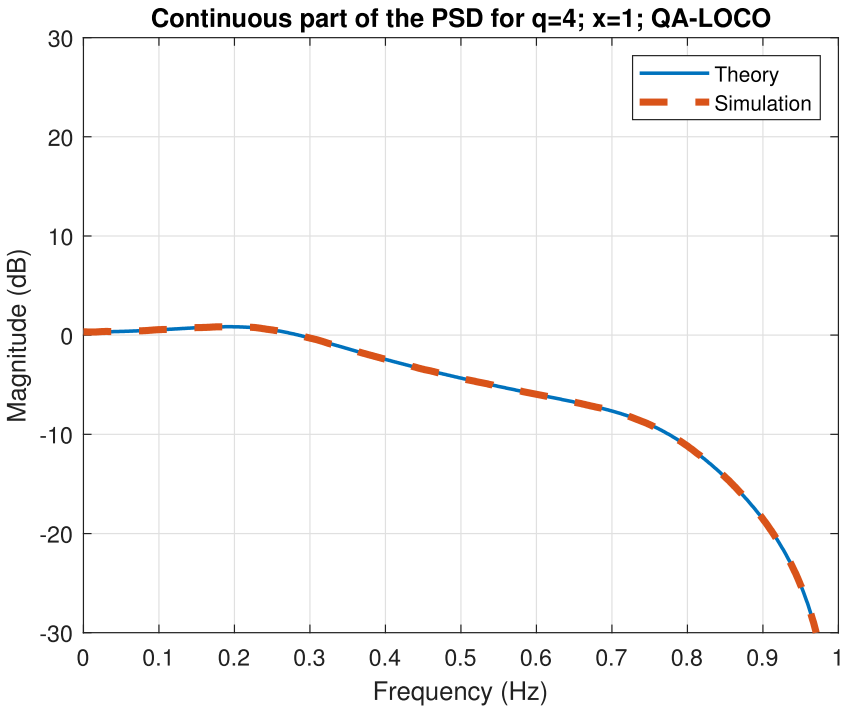

Figure 4.5: Continuous part of the PSD for $q = 4$, $x = 1$.

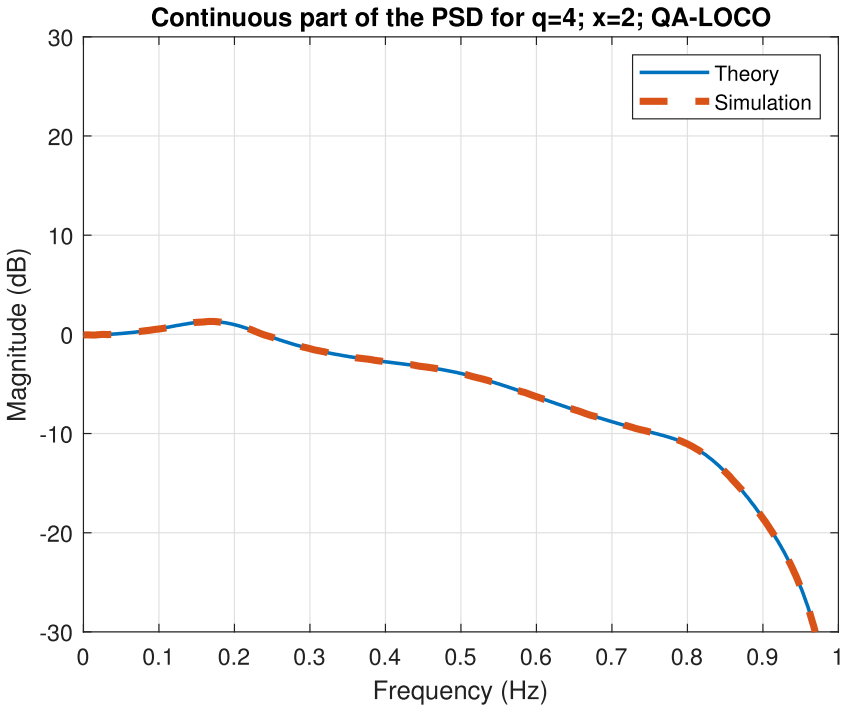

Figure 4.6: Continuous part of the PSD for $q = 4$, $x = 2$.

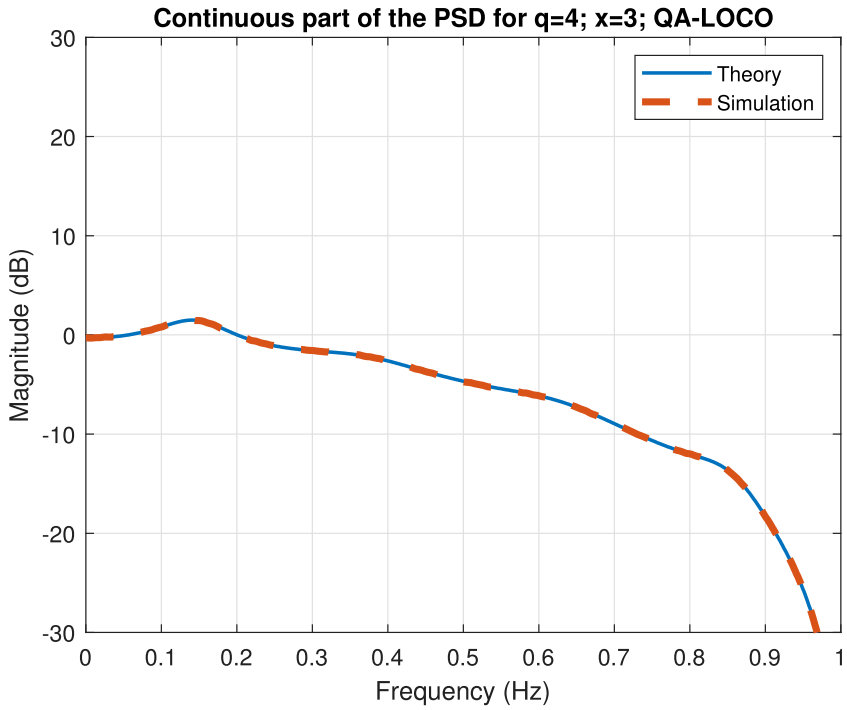

Figure 4.7: Continuous part of the PSD for $q = 4$, $x = 3$.

4.3.2 Results for TLC

Results are as follows for multi-level cells that have 3 bits per cell and have a total of $q = 4$ levels per cell.

The discrete part of the PSD for Figure 4.8 is a Dirac delta function at $f = 0$ with an area of $\mathbb{E}^2[Y_n] = 11.6896$. It is seen from Figure 4.8 that the theoretical results match the experimental results perfectly. For a TLC, three bits exist per cell makes the total number of levels 8. With the increase in q, the probability of a forbidden pattern happening decreases compared to MLC since their number is increased. Since less coding is applied, Figure 4.8 is closer to the pattern of the uncoded stream compared to Figure 4.5.

The discrete part of the PSD for Figure 4.9 is a Dirac delta function at $f = 0$ with an area of $\mathbb{E}^2[Y_n] = 11.3041$. It is seen from Figure 4.9 that the theoretical results also match the experimental results perfectly. In Figure 4.9, the number of forbidden patterns is increased. Therefore, the pattern deviates more from one of an uncoded

sequence's shape, and the shape is differed compared to Figure 4.8.

Discrete part of the PSD for Figure 4.10 is a Dirac delta function at $f = 0$ with an area of $\mathbb{E}^2[Y_n] = 11.0211$. It is seen from Figure 4.10 that the theoretical results again match the experimental results perfectly. In Figure 4.10, the number of forbidden patterns is further increased. Therefore, compared to Figure 4.8 and 4.9, the pattern has a different pattern again, more damped. As x increases, the maximum power density point shifts to the left.

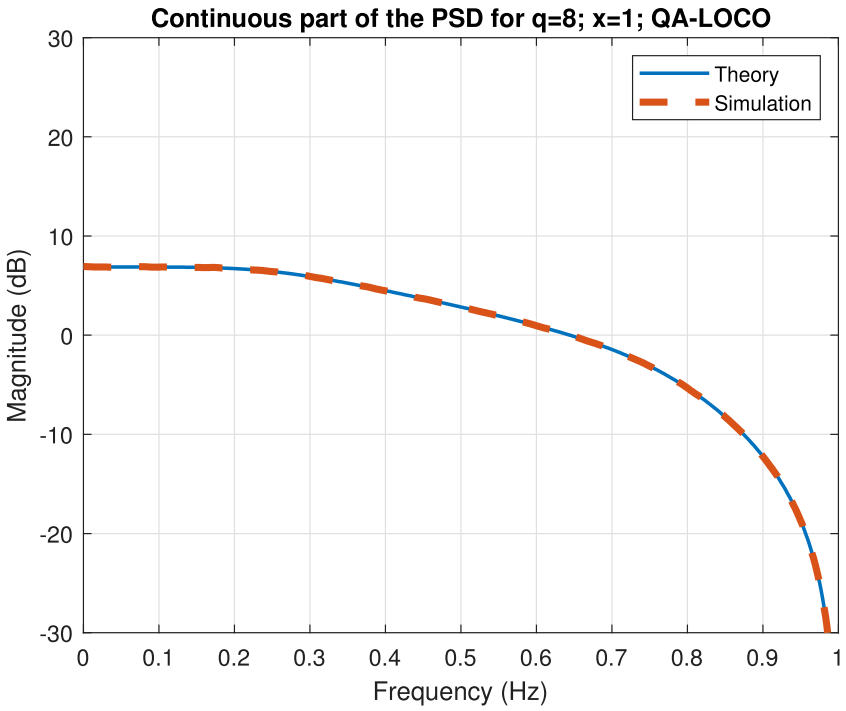

Figure 4.8: Continuous part of the PSD for $q = 8$, $x = 1$.

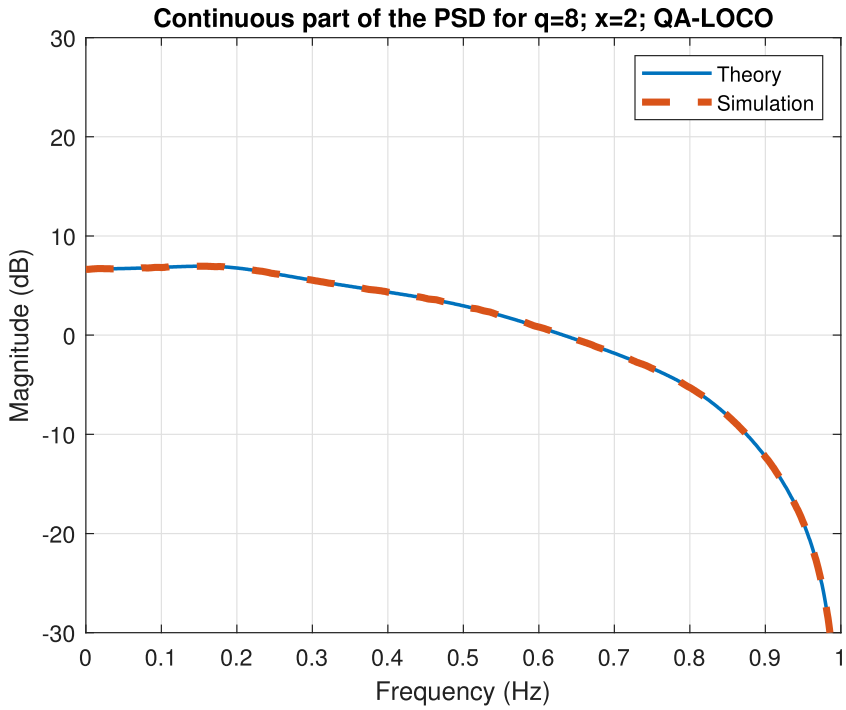

Figure 4.9: Continuous part of the PSD for $q = 8$, $x = 2$.

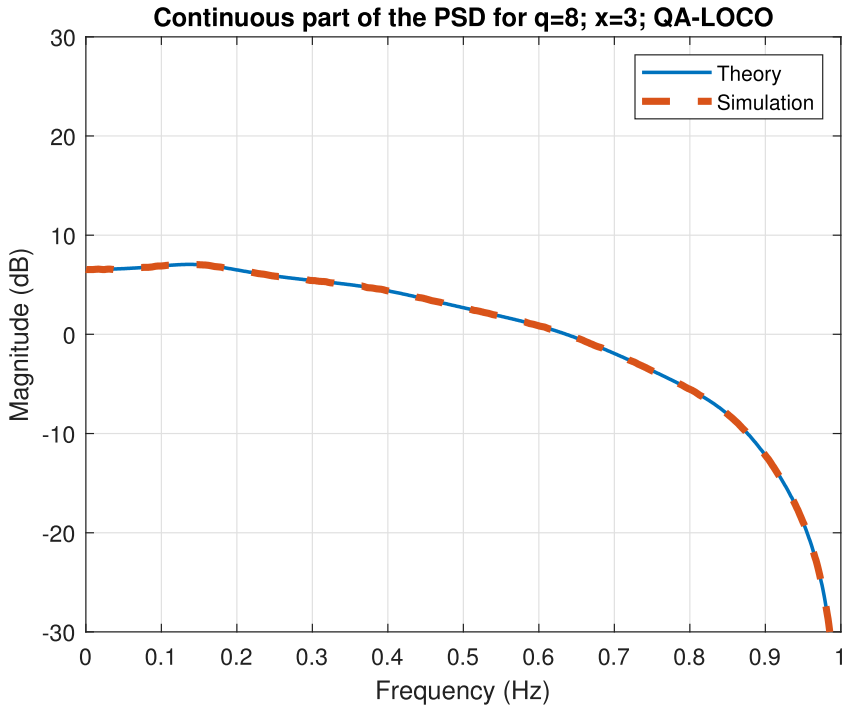

Figure 4.10: Continuous part of the PSD for $q = 8$, $x = 3$.

4.3.3 Results for QLC

Results are as follows for multi-level cells that have 4 bits per cell and have a total of $q = 16$ levels per cell.

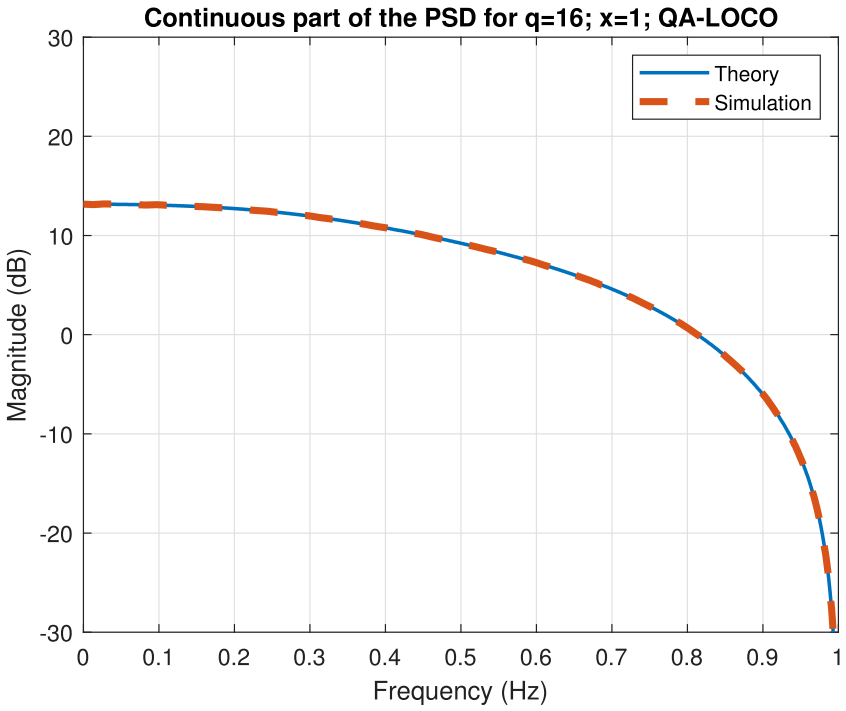

Figure 4.11: Continuous part of the PSD for $q = 16$, $x = 1$.

The discrete part of the PSD for Figure 4.11 is a Dirac delta function at $f = 0$ with an area of $\mathbb{E}^2[Y_n] = 55.5080$. It is seen from Figure 4.11 that the theoretical results match the experimental results perfectly. For a QLC, four bits exist per cell, which makes the total number of levels sixteen. With this exponential increase in q, the probability of a forbidden pattern happening decreases so significantly that Figure 4.11 becomes almost a sinc function.

The discrete part of the PSD for Figure 4.12 is a Dirac delta function at $f = 0$ with an area of $\mathbb{E}^2[Y_n] = 54.9152$. It is seen from Figure 4.12 that the theoretical results match the experimental results perfectly. The increase in the forbidden patterns changes the shape, as discussed earlier. However, for Figure 4.12, the difference with Figure 4.11 is not clear.

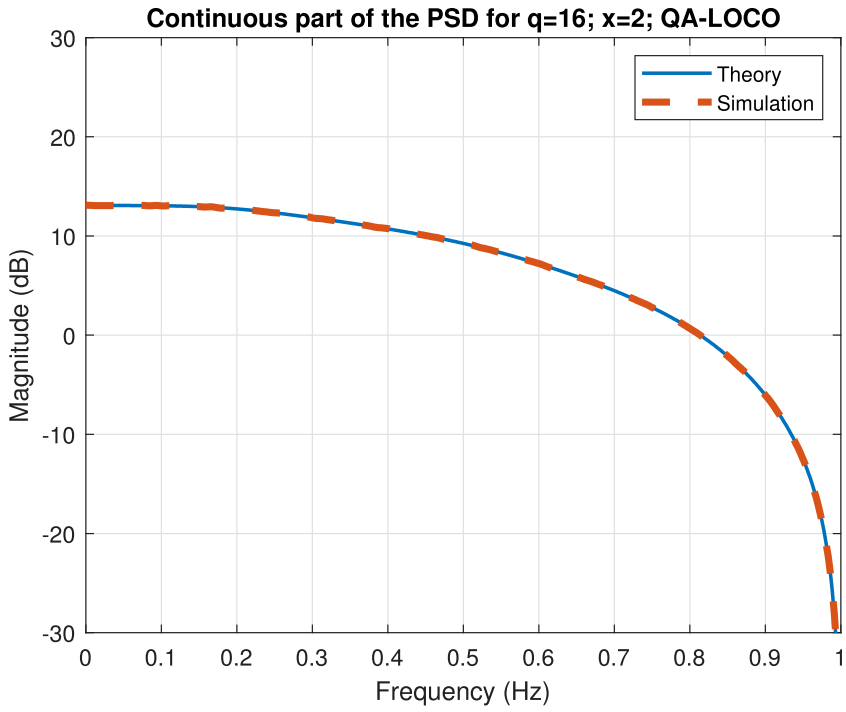

Figure 4.12: Continuous part of the PSD for $q = 16$, $x = 2$.

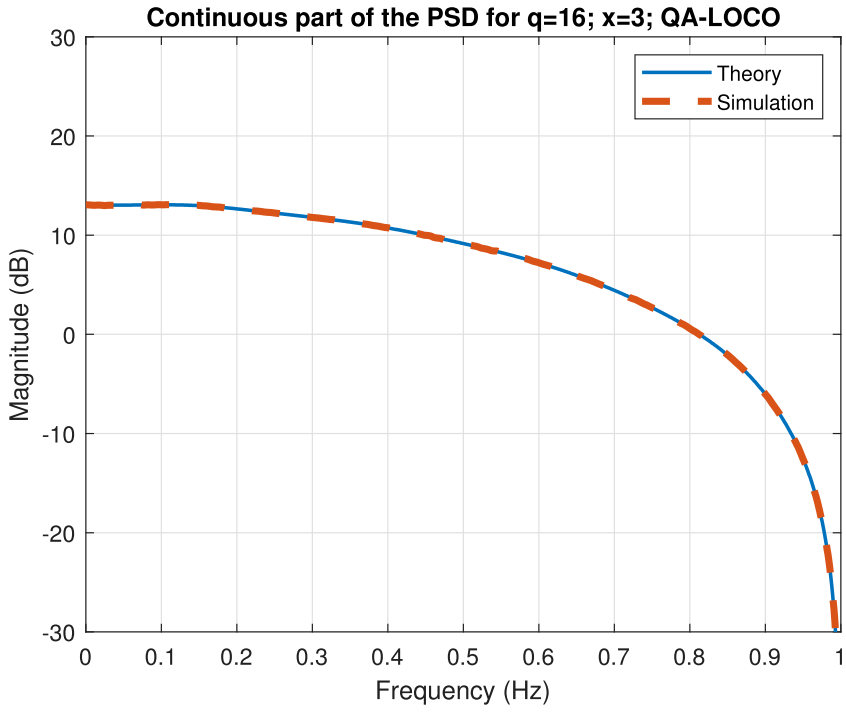

Figure 4.13: Continuous part of the PSD for $q = 16$, $x = 3$.

The discrete part of the PSD for Figure 4.13 is a Dirac delta function at $f = 0$ with an area of $\mathbb{E}^2[Y_n] = 54.4296$. It is seen from Figure 4.13 that the theoretical results match the experimental results perfectly. For Figure 4.13, bare-eye cannot rationalize the change since it seems there is not any compared to Figure 4.11 and 4.12.

4.3.4 Comparative Results for SLC, MLC, and TLC

This subsection plots x levels from 1 to 5 for SLC, MLC, and TLC.

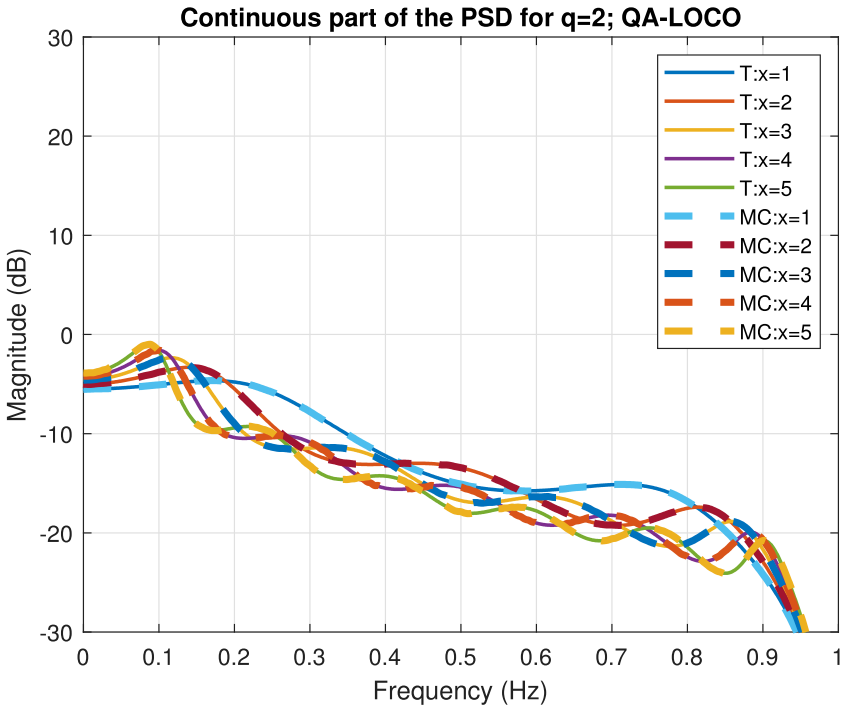

Figure 4.14: Continuous part of the PSDs for $q = 2$ for all x.

For Figure 4.14, the changes in the shape when x increases are seen clearly, and the shape is too different from a sinc function. As x increases, the overall bandwidth of the signal decreases. This is a result of the increase in forbidden patterns. When x increases, the sequence generates more 0's in between the 1's, which makes rapid transitions less and the higher frequency components in the signal lessens. This also causes the peak of the plot to shift left as the majority of the signal components lay on lower frequencies.

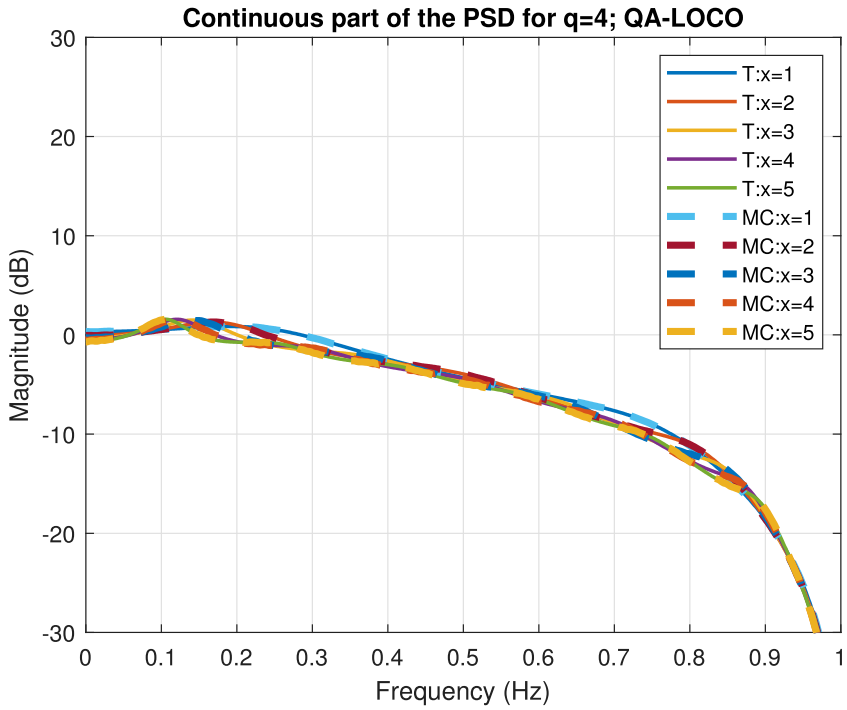

Figure 4.15: Continuous part of the PSDs for $q = 4$ for all x.

For Figure 4.15, the lines for different x are closer compared to Figure 4.14. However, the shift in the peak of maximum power density is still clear since a similar discussion to the binary case is also valid here, with the overall effect is lower due to the increased q.

For Figure 4.16, all the lines for different x values are close since the increase in x is linear while the increase in q is exponential. The shift of the peak point to the left and the smaller bandwidth discussion is valid here also but the overall effect is nearly unobservable due to the much increased q.

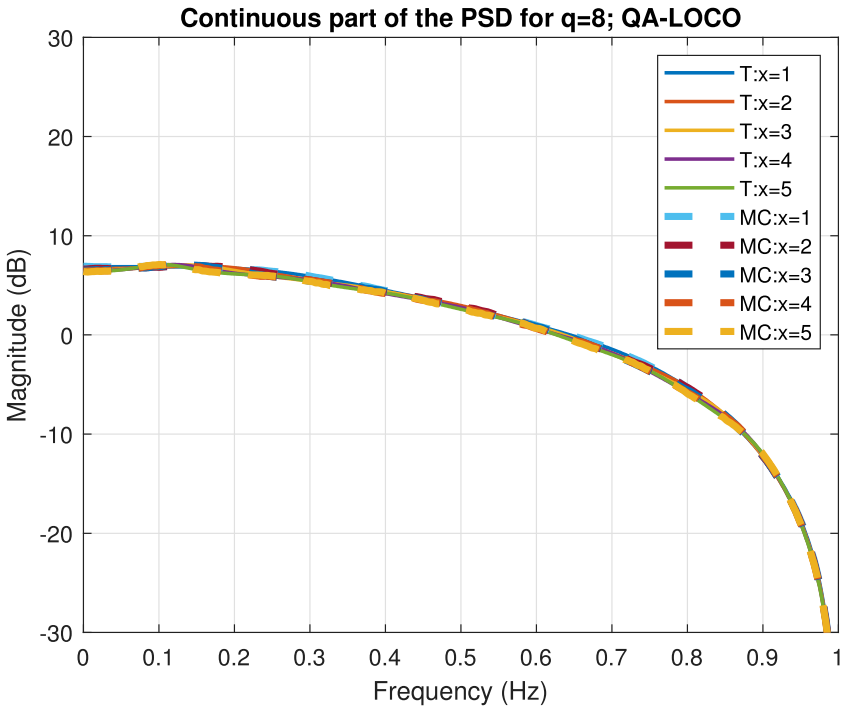

Figure 4.16: Continuous part of the PSDs for $q = 8$ for all x.

Acknowledgments

The contributions made by Prof. Robert Calderbank, Assist. Prof. Ahmed Hareedy, Dr. Jessica Centers and Norah Tan were instrumental in the completion of this section.

CHAPTER 5

APPROXIMATE PSD FOR MULTI-LEVEL CONSTRAINED CODES: OP-LOCO CODES

In this chapter, an approximate method for deriving the power spectra for OP-LOCO codes [31] will be presented. Section 5.1 will provide preliminary background for OP-LOCO codes, Section 5.2 will show the approximation method for the PSD step-by-step, and Section 5.3 will present the results that are plotted approximation against MC simulations.

5.1 OP-LOCO Codes

As discussed in Section 2.3.2 and Section 3.1, TDMR is a technology that allows magnetic storage to remain competitive regarding storage density [57, 58, 61]. In TDMR, horizontal tracks are compressed and not separated from one another [61], enabling a storage density of 10 terabits per square inch [57, 59].

Considering a 3×3 grid in the TDMR system, data patterns that result in the isolation of the bit at the center of this grid should be forbidden [60]. Additionally, data patterns where the central bit is surrounded by 4 complementary bits in both upwards and downwards directions, excluding the 4 corner bits, should also be forbidden since they significantly increase two-dimensional interference along both the horizontal and vertical track directions and likely to change the sign of the center bit [31]. It is important to note that the bits at the corners cause less interference than bits at positions with Manhattan distance 1 from the center [60, 64]. This data pattern is the PIS pattern, as discussed in Section 3.1. The prevention of PIS patterns is also named the no-isolated-bit (NIB) constraint [60, 64].

The literature includes studies on both two-dimensional RLL codes [64, 66] and two-dimensional codes with NIB constraints [60, 62, 65]. In the former case, the 2D (d, k)-RLL constraint is composed of all binary arrays where every row and column of the one-dimensional (d, k)-RLL constraint is satisfied when the square lattice is used, and the appropriate range of parameters in both dimensions is $0 \leq d < k \leq \infty$ [66]. It is seen that the codes with NIB constraints offer significantly higher code rates, which highlights the importance of creating coding schemes that forbid PIS patterns upon writing.

In 2022, Hareedy et al. [31] introduced novel rate-wise optimal LOCO codes, where rate-wise optimization refers to minimal redundancy [70]. These codes are named OP-LOCO codes and explicitly designed to prevent error-prone PIS patterns from being written onto the TDMR medium [31]. These non-binary codes are associated with level-based signaling, significantly increasing the system reliability and device performance [31]. OP-LOCO codes are capacity-achieving as the rates approach the system's maximum capacity even at moderate lengths [31]. OP-LOCO codes also offer minimal redundancy, simplicity, and reconfigurability like the other codes from the LOCO family [31].

In their work [31], they adopt a practical Voronoi TDMR channel model, which treats the distribution of grain centers as a point process [60]. The model is characterized by a wide read head that simultaneously reads data from three adjacent down tracks [58, 61, 65]. In this model [60], down tracks in the TD grid are indexed sequentially from 0 to $D - 1$, where D is the total number of down tracks and is divisible by 3. Thus, this setup allows the down tracks to be partitioned into groups of three, such as $(0, 1, 2), (3, 4, 5), \ldots, (D - 3, D - 2, D - 1)$. Interference from one group of tracks to another in the cross-track direction is negligible [58, 65]. Consequently, the coding problem transitions from a two-dimensional binary-constrained problem to a one-dimensional non-binary constrained problem [31]. In this new framework, a symbol in $\mathrm{GF}(8)$ represents a column of three bits to be written across three adjacent down tracks within the same group [31]. It can be observed that three symbols from $\mathrm{GF}(8)$ together create a 3×3 grid pattern, which will help define the error-prone patterns.

For OP-LOCO codes [31], the following standard mapping-demapping from binary patterns to $\mathrm{GF}(8)$ symbols is used:

$$\begin{aligned}
[0\ 0\ 0]^{\mathrm{T}} &\longleftrightarrow 0,\\
[0\ 0\ 1]^{\mathrm{T}} &\longleftrightarrow 1,\\
[0\ 1\ 0]^{\mathrm{T}} &\longleftrightarrow \alpha,\\
[0\ 1\ 1]^{\mathrm{T}} &\longleftrightarrow \alpha^2,\\
[1\ 0\ 0]^{\mathrm{T}} &\longleftrightarrow \alpha^3,\\
[1\ 0\ 1]^{\mathrm{T}} &\longleftrightarrow \alpha^4,\\
[1\ 1\ 0]^{\mathrm{T}} &\longleftrightarrow \alpha^5,\\
[1\ 1\ 1]^{\mathrm{T}} &\longleftrightarrow \alpha^6.
\end{aligned} \tag{5.1}$$

Denoting an OP-LOCO code of length m by $\mathcal{OPC}_8^m$, the formation of the code follows the definition of a generic LOCO code with $q = 8$, $C_q^m = \mathcal{OPC}_8^m$ [31]. In addition, the index of the codewords, the cardinality, and the encoding-decoding rule are derived in the same way [31].

The set of forbidden patterns, denoted by $\mathcal{T}$ is as follows:

$$\begin{aligned}
\mathcal{T} = \mathcal{O}P^8 \triangleq \big\{ &\bar{\beta}_1 \alpha \beta_1, \bar{\beta}_2 \alpha^4 \beta_2, \forall \bar{\beta}_1, \beta_1 \in \{0, 1, \alpha^3, \alpha^4\} \\
&\text{and} \, \forall \bar{\beta}_2, \beta_2 \in \{\alpha, \alpha^2, \alpha^5, \alpha^6\} \big\}.
\end{aligned} \tag{5.2}$$

A critical discussion is the structure of forbidden patterns. Following from (5.1), symbols α and α^4 are mapped to $[0\ 1\ 0]^{\mathrm{T}}$ and $[1\ 0\ 1]^{\mathrm{T}}$ respectively, and they appear as the middle track of the forbidden pattern as it is seen from (5.2). Therefore, it can be observed that the middle bits from symbols α and α^4 are the central bits of a 3×3 grid and also have their upper and lower bits in the complementary sign. It can be said that having the symbol α or α^4 in the central position is risky and makes the 3×3 grid a candidate for forbidden patterns.

The first and third symbols in $\mathcal{T}$ from (5.2) will also be closely inspected. For symbol α, symbols $\bar{\beta}_1$ and β_1 belong to the set $\{0, 1, \alpha^3, \alpha^4\}$. By looking at the symbols' corresponding binary representation from (5.1), it can be observed that all the symbols in this set have their center bit as 0. Having these symbols as the first and third symbols,

the center bit of the second symbol α, which is also the central bit of the 3×3 grid, becomes surrounded by complementary bits from the left and right directions. Since the center bit of symbol α was surrounded by complementary bits already with this addition to the first and third tracks, the 3×3 grid becomes a forbidden PIS pattern. Analogously, for symbol α^4, symbols $\bar{\beta}_2$ and β_2 belong to the set $\{\alpha, \alpha^2, \alpha^5, \alpha^6\}$ and it can be observed that all the symbols in this set have their center bit as 1 in their corresponding binary representation from (5.1). Having these symbols as the first and third symbols, the center bit of the second symbol, α^4, becomes surrounded by complementary bits from the left and right directions, with the center bit of symbol α^4 surrounded by complementary bits already, this addition by the first and third tracks makes the 3×3 grid become the other forbidden PIS pattern. In addition, referring to (5.2), there exists $(4 \times 4) + (4 \times 4) = 32$ configurations possible for a PIS pattern.

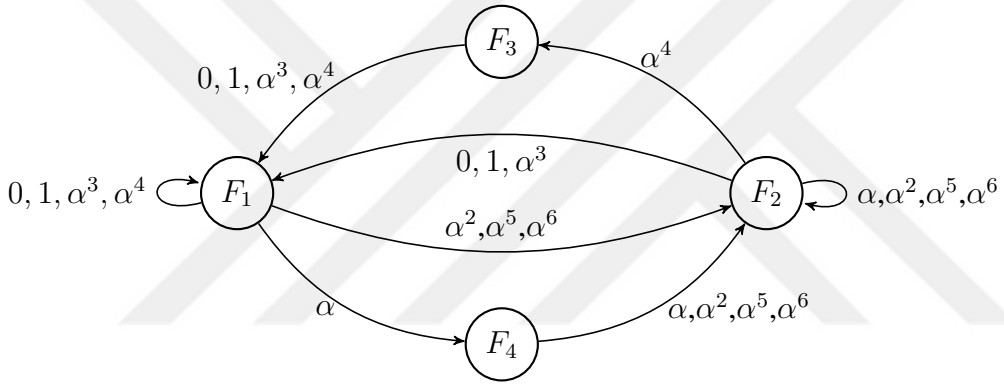

Figure 5.1: FSTD for OP-LOCO codes that have infinite length, defined over $\mathrm{GF}(8)$ and prevent PIS patterns.

An FSTD of an infinite $8 - ary$ constrained sequence defined over $\mathrm{GF}(8)$ in which 32 PIS patterns in (5.2) are prevented in is shown in above Figure 5.1.

Let the corresponding adjacency matrix be $\mathbf{F}$ and the maximum real positive eigenvalue of $\mathbf{F}$ be $\lambda_{\max}(\mathbf{F})$.

$$\mathbf{F} = \begin{bmatrix} 4 & 3 & 0 & 1 \\ 3 & 4 & 1 & 0 \\ 4 & 0 & 0 & 0 \\ 0 & 4 & 0 & 0 \end{bmatrix} \tag{5.3}$$

The capacity C, in input bits per coded symbol, and the normalized capacity C_n can be calculated as [21]:

$$C = \log_2(\lambda_{\max}(\mathbf{F})) = \log_2 7.5311 = 2.9129,$$
$$C^n = \frac{1}{3}C = 0.9710. \tag{5.4}$$

Moreover, OP-LOCO codes achieve substantial frame error rate (FER) and bit error rate (BER) improvements despite the absence of traditional error-correcting codes [31]. This is due to the inherent capability of OP-LOCO codes to conduct error correction analogous to LOCO codes [19]. The mechanism involves examining the encoded $8 - ary$ sequence of length m for constraint violations. If a violation is detected, the bit corresponding to the value nearest to zero within the $3 \times m$ grid of the codeword is altered [31]. Subsequently, the sequence is converted back using $\mathrm{GF}(8)$, and the constraint is re-evaluated [31]. If the constraint is now satisfied, this indicates successful one-symbol error correction [31]. The reader is referred to [19] for more information.

An essential factor that distinguishes OP-LOCO codes from other NIB constraint TD codes is that it achieves rate gain by focusing only on PIS patterns within the same group of down tracks, as interference between groups in the cross-track direction is of less importance [31]. As a result of this methodology, the highest achievable normalized rate for OP-LOCO codes is 0.9710, as shown in (5.4), while the highest achievable rate in [60] is 0.9238.

To elaborate the comparison in greater detail, codes that use the technique of stuffing bits into a TD grid to forbid PIS patterns [60, 62] are not customized for a TDMR system with a wide read head such as the one OP-LOCO codes adopt [58, 61] even though wide read heads offer the advantage of higher speeds in reading. It is also vital to mention that codes in [60, 66] which utilize bit-stuffing techniques, lack explicit ways to convert unconstrained input messages into codewords, or vice versa, while OP-LOCO codes offer simple systematic mapping-demapping for conversion via the integer index [31].

5.2 Approximation Method

This section will present an approximation method to obtain the PSD for OP-LOCO codes as closely as possible. It is important to note that OP-LOCO codes are finite-length codes. However, in this thesis, the approximation method will be developed for infinite-length OP-LOCO codes. From now on, referring to OP-LOCO codes will mean infinite-length OP-LOCO codes. The fundamental properties of the OP-LOCO codes still apply, and the forbidden set T is defined in the same way. Also, OP-LOCO codes use level-based signaling, making it possible to apply the method for obtaining the PSD for binary sequences in [8].

Before delving into the derivation, why an approximation method was needed in the first place will be discussed. A summary of work conducted so far will be given to highlight the essential steps.

The method for obtaining a PSD introduced in [7] and [8] requires a binary sequence. Thus, the steps taken so far for the cases of SP-LOCO and QA-LOCO codes were finding a way to introduce a fundamental binary mapping for the symbols in the alphabet and expressing the non-binary signal in terms of the binary signal. For SP-LOCO, the symbols in $\mathrm{GF}(8)$ were mapped to $\mathrm{GF}(2)$, as was already the case for the configuration of the code. For QA-LOCO, the symbols in $\mathrm{GF}(q)$ are mapped to $\mathrm{GF}(2)$ by considering the highest level symbol as a 1 and the lower level symbols as a 0, benefiting the equal treatment for each low-level symbol. Therefore, the main idea is to divide the symbols in the non-binary alphabet into two groups, depending on the code's fundamental properties.

Considering the forbidden pattern set $\mathcal{T}$ for OP-LOCO codes, which is given in (5.2), it can be seen that the variables β_1 and $\bar{\beta}_1$ belong to one set and β_2 and $\bar{\beta}_2$ belong to another set where these two sets are mutually exclusive, which indicates two groups. However, the symbols in the middle of the forbidden patterns cannot be any element in the respective sets. In fact, if an element is considered from the respective sets, the element is the middle symbol that creates the forbidden pattern with a certain probability, which will create the essence in the approximation method that will be suggested. So, the symbols in the middle divide the defined groups of sets into half

again, which creates another step and complicates the analysis. It is logical to deduce that the FSTD of OP-LOCO is more complex, and applying the same idea of dividing all symbols into half that is used until now would not work or at least would not work easily. Therefore, a solution is offered by creating an analysis based on the two sets mentioned above in the first step blindly as if it is correct to assume all the members in the sets would cause a forbidden pattern, then closely examining if that random element in the set would actually create a forbidden pattern. Lastly, these two steps are realized in an FSTD. It is important to note that the probability analysis involved makes the method an approximate solution.

For the approximation method presented in this section to obtain the PSD for OP-LOCO codes, the maxentropic symbol probabilities are needed for the theorem application of the binary sequence and the method.

Using the method proposed in [21], maxentropic symbol probabilities are calculated as follows, where $\mathbf{V}$ represents the maxentropic transition probabilities and $\boldsymbol{\pi}$ represents the steady state distribution of maxentropic Markov chain. The calculation method will not be shown here, and the reader is referred to [72].

$$\mathbf{V} = \begin{bmatrix} v_{1,1} & v_{1,2} & v_{1,3} & v_{1,4} \\ v_{2,1} & v_{2,2} & v_{2,3} & v_{2,4} \\ v_{3,1} & v_{3,2} & v_{3,3} & v_{3,4} \\ v_{4,1} & v_{4,2} & v_{4,3} & v_{4,4} \end{bmatrix} = \begin{bmatrix} 0.5311 & 0.3983 & 0 & 0.0705 \\ 0.3983 & 0.5311 & 0.0705 & 0 \\ 1 & 0 & 0 & 0 \\ 0 & 1 & 0 & 0 \end{bmatrix} \tag{5.5}$$

$$\boldsymbol{\pi} = \begin{bmatrix} \pi_1 & \pi_2 & \pi_3 & \pi_4 \end{bmatrix} = \begin{bmatrix} 0.4671 & 0.4671 & 0.0329 & 0.0329 \end{bmatrix} \tag{5.6}$$

Let $\{S_n\}$ represent the stream of symbols where $S_n \in \{0, 1, \alpha, \alpha^2, \alpha^3, \alpha^4, \alpha^5, \alpha^6\}$. Using the FSTD presented in Figure 5.1 and the results from (5.6) and (5.5), the symbol probabilities for symbols 0 and α in the equilibrium state can be calculated as follows:

$$\mathbb{P}[S_n = 0] = \pi_1 \cdot v_{1,1} \cdot \frac{1}{4} + \pi_2 \cdot v_{2,1} \cdot \frac{1}{3} + \pi_3 \cdot v_{3,1} \cdot \frac{1}{4} = 0.13227, \tag{5.7}$$

$$\mathbb{P}[S_n = \alpha^4] = \pi_1 \cdot v_{1,1} \cdot \frac{1}{4} + \pi_2 \cdot v_{2,3} \cdot 1 + \pi_3 \cdot v_{3,1} \cdot \frac{1}{4} = 0.10319. \tag{5.8}$$

Notice that the results in (5.7) and (5.8) are not the same. Hence, the probability of each symbol is not the same for OP-LOCO codes.

Now, the mapping-demapping given in (5.1) will be extended to physical levels. Note that the discussion about the relations between the physical levels was provided in Section 3.2 applies, and the result will be used directly.

Let $\mathrm{GF}(8) = \{0, 1, \alpha, \alpha^2, \alpha^3, \alpha^4, \alpha^5, \alpha^6\}$ represent the symbols and $a_k, k \in \{0, 1, 2, 3\}$ represent the physical levels where $a_0 > a_1 = a_2 > a_3 > 0$. The extended mapping-demapping for 3-tuple binary down-track patterns, their $\mathrm{GF}(8)$ symbols and physical levels are as follows:

$$
\begin{array}{lcll}
3-\text{Tuple} & & \mathrm{GF}(8) & \text{Level} \\
[0\ 0\ 0]^{\mathrm{T}} & \longleftrightarrow & 0 & \longleftrightarrow -a_0, \\
[0\ 0\ 1]^{\mathrm{T}} & \longleftrightarrow & 1 & \longleftrightarrow -a_1, \\
[0\ 1\ 0]^{\mathrm{T}} & \longleftrightarrow & \alpha & \longleftrightarrow +a_3, \\
[0\ 1\ 1]^{\mathrm{T}} & \longleftrightarrow & \alpha^2 & \longleftrightarrow +a_2, \\
[1\ 0\ 0]^{\mathrm{T}} & \longleftrightarrow & \alpha^3 & \longleftrightarrow -a_2, \\
[1\ 0\ 1]^{\mathrm{T}} & \longleftrightarrow & \alpha^4 & \longleftrightarrow -a_3, \\
[1\ 1\ 0]^{\mathrm{T}} & \longleftrightarrow & \alpha^5 & \longleftrightarrow +a_1, \\
[1\ 1\ 1]^{\mathrm{T}} & \longleftrightarrow & \alpha^6 & \longleftrightarrow +a_0.
\end{array} \tag{5.9}
$$

Let the sequence of the physical levels be $\{Y_n\}$ where $Y_n \in \{\pm a_0, \pm a_1, \pm a_2, \pm a_3\}$. Let the binary sequence be $\{X_n\}$ where $X_n \in \{0, 1\}$, then the binary mapping sequence is defined as follows:

$$
X_n = \begin{cases} 1, & \text{if } Y_n \in \{a_0, a_1, a_2, a_3\}, \\ 0, & \text{else.} \end{cases} \tag{5.10}
$$

The positive physical levels are mapped to 1 in X_n, while the negative physical levels are mapped to 0. Looking at the mapping-demapping presented in (5.9), it can be observed that the physical levels that are mapped to 1 have a 1 in the middle position of the binary 3-tuple and the physical levels that are mapped to 0 have a 0 in the

middle position of the binary 3-tuple, considering this relation, two families will be defined. Define the family of 1's as a set F_1 that has the $\mathrm{GF}(8)$ symbol mappings of the positive physical levels and the family of 0's as a set F_0 that has the $\mathrm{GF}(8)$ symbol mappings of the negative physical levels as follows:

$$\begin{aligned}\mathcal{F}_1 &= \{\alpha, \alpha^2, \alpha^5, \alpha^6\},\\ \mathcal{F}_0 &= \{0, 1, \alpha^3, \alpha^4\}.\end{aligned} \tag{5.11}$$

Referring back to $\mathcal{T}$ given in (5.2), the forbidden patterns have the middle symbols as α and α^4. Thus, it appears that α is the detrimental symbol in F_1 while α^4 is the detrimental symbol in F_0.

Because of the symmetry in OP-LOCO codes, the detrimental symbol from a family of 1's, α, and the detrimental symbol from a family of 0's, α^4 have equal probabilities.

$$\mathbb{P}[S_n = \alpha] = \mathbb{P}[S_n = \alpha^4] = 0.10319 \tag{5.12}$$

Non-detrimental symbols from both families have equal probabilities among each other, and because of the symmetry, this probability is the same for all non-detrimental symbols.

$$\begin{aligned}\mathbb{P}[S_n = 0] = \mathbb{P}[S_n = 1] = \mathbb{P}[S_n = \alpha^3] = 0.13227,\\ \mathbb{P}[S_n = \alpha^2] = \mathbb{P}[S_n = \alpha^5] = \mathbb{P}[S_n = \alpha^6] = 0.13227\end{aligned} \tag{5.13}$$

Note that the symbol probabilities from both sets $\mathcal{F}_1$ and $\mathcal{F}_0$ individually sum up to 0.5 as expected due to symmetry.

$$\begin{aligned}\mathbb{P}[S_n = 0] + \mathbb{P}[S_n = 1] + \mathbb{P}[S_n = \alpha^3] + \mathbb{P}[S_n = \alpha^4] = 0.5,\\ \mathbb{P}[S_n = \alpha] + \mathbb{P}[S_n = \alpha^2] + \mathbb{P}[S_n = \alpha^5] + \mathbb{P}[S_n = \alpha^6] = 0.5\end{aligned} \tag{5.14}$$

Given the sequences $\{S_n\}$ and $\{Y_n\}$, the mapping-demapping relationship in (5.9) is defined by a bijective function such that each symbol is uniquely mapped to a corresponding physical level and vice versa. Thus, this bidirectional mapping ensures that the probability of S_n taking a specific value is equal to the probability of Y_n

taking the corresponding physical level. Results found in (5.12), (5.13) and (5.11) can be rewritten as follows with introducing p_3, p_{012}, p_{F1} and p_{F0} :

$$p_3 = \mathbb{P}[Y_n = a_3] = \mathbb{P}[Y_n = -a_3] = 0.10319, \tag{5.15}$$

$$\begin{aligned} p_{012} &= \mathbb{P}[Y_n = -a_0] = \mathbb{P}[Y_n = -a_1] = \mathbb{P}[Y_n = -a_2] \\ &= \mathbb{P}[Y_n = a_0] = \mathbb{P}[Y_n = a_1] = \mathbb{P}[Y_n = a_2] \\ &= 0.13227, \end{aligned} \tag{5.16}$$

$$\begin{aligned} p_{\mathrm{F1}} &= \mathbb{P}[Y_n = a_0] + \mathbb{P}[Y_n = a_1] + \mathbb{P}[Y_n = a_2] + \mathbb{P}[Y_n = a_3] \\ p_{\mathrm{F0}} &= \mathbb{P}[Y_n = -a_0] + \mathbb{P}[Y_n = -a_1] + \mathbb{P}[Y_n = -a_2] + \mathbb{P}[Y_n = -a_3] \\ &= 0.5. \end{aligned} \tag{5.17}$$

In order to simplify the expressions and improve the readability of the equations, the following notations will be used throughout the derivation:

$$\begin{aligned} p_{00} &= \mathbb{P}[X_0 = 0, X_k = 0], \\ p_{01} &= \mathbb{P}[X_0 = 0, X_k = 1], \\ p_{10} &= \mathbb{P}[X_0 = 1, X_k = 0], \\ p_{11} &= \mathbb{P}[X_0 = 1, X_k = 1]. \end{aligned} \tag{5.18}$$

The auto-correlation function of $\{X_n\}$ can be written as follows:

$$\mathbb{R}_X(k) = \mathbb{E}[X_0 X_k] = 0 \cdot 0 \cdot p_{00} + 0 \cdot 1 \cdot p_{01} + 1 \cdot 0 \cdot p_{10} + 1 \cdot 1 \cdot p_{11} = p_{11}. \tag{5.19}$$

Since the code is symmetric, the following can be written,

$$\begin{aligned} \mathbb{P}[X_0 = 1, X_k = 1] &= \mathbb{P}[X_0 = 0, X_k = 0] = p_{11}, \\ \mathbb{P}[X_0 = 1, X_k = 0] &= \mathbb{P}[X_0 = 0, X_k = 1] = p_{10}. \end{aligned} \tag{5.20}$$

Using the unit measure axiom of probability,

$$\begin{aligned} 2 \cdot p_{11} + 2 \cdot p_{10} &= 1, \\ p_{10} &= \frac{1}{2} - p_{11}, \\ p_{10} &= \frac{1}{2} - \mathbb{E}[X_0 X_k]. \end{aligned} \tag{5.21}$$

For the sequence $\{Y_n\}$, the auto-correlation function can be written as follows where $a_m, a_n \in \{a_0, a_1, a_2, a_3\}$, $m, n \in \{0, 1, 2, 3\}$ and $k \neq 0$:

$$\begin{aligned}\mathbb{R}_Y(k) = \mathbb{E}[Y_0 Y_k] = &\sum_{m=0}^{3}\sum_{n=0}^{3} a_m \cdot a_n \cdot \mathbb{P}[Y_0 = a_m, Y_k = a_n] \\ &- \sum_{m=0}^{3}\sum_{n=0}^{3} a_m \cdot a_n \cdot \mathbb{P}[Y_0 = a_m, Y_k = -a_n] \\ &- \sum_{m=0}^{3}\sum_{n=0}^{3} a_m \cdot a_n \cdot \mathbb{P}[Y_0 = -a_m, Y_k = a_n] \\ &+ \sum_{m=0}^{3}\sum_{n=0}^{3} a_m \cdot a_n \cdot \mathbb{P}[Y_0 = -a_m, Y_k = -a_n]. \end{aligned} \tag{5.22}$$

Because of the symmetry, (5.22) can be rewritten as follows:

$$\begin{aligned}\mathbb{E}[Y_0 Y_k] = &2 \cdot \sum_{m=0}^{3}\sum_{n=0}^{3} a_m \cdot a_n \cdot \mathbb{P}[Y_0 = a_m, Y_k = a_n] \\ &- 2 \cdot \sum_{m=0}^{3}\sum_{n=0}^{3} a_m \cdot a_n \cdot \mathbb{P}[Y_0 = a_m, Y_k = -a_n] \end{aligned} \tag{5.23}$$

Since OP-LOCO codes do not have the same probability for each symbol, each of the 16 combinations of physical levels will have different probabilities. Remember that the detrimental symbol in $\mathcal{F}_\infty$ is α while the detrimental symbol in $\mathcal{F}_\prime$ is α^4 and their corresponding physical levels are a_3 and $-a_3$ respectively.

Now, the probability $\mathbb{P}[Y_0 = a_m, Y_k = a_n]$ will be closely inspected case by case where $a_m, a_n \in \{a_0, a_1, a_2, a_3\}$. Define $y_0, y_k \in \{a_0, a_1, a_2\}$ so that they represent the physical levels that belong to the non-detrimental symbols in $\mathcal{F}_1$. Also note that $p_{\mathrm{F}_1} = 0.5$ as showed in (5.17) and use the notation given in (5.15) and (5.16).

Case 0: $Y_0 = y_0$ and $Y_k = y_k$

$$\begin{aligned}
p_{\mathrm{S0}} &= \mathbb{P}[Y_0 = y_0, Y_k = y_k] \\
&= \sum_{x_0} \sum_{x_k} \mathbb{P}[Y_0 = y_0, Y_k = y_k \mid X_0 = x_0, X_k = x_k] \cdot \mathbb{P}[X_0 = x_0, X_k = x_k] \\
&= \mathbb{P}[Y_0 = y_0, Y_k = y_k \mid X_0 = 1, X_k = 1] \cdot p_{11} \\
&= \mathbb{P}[Y_0 = y_0 \mid X_0 = 1] \cdot \mathbb{P}[Y_k = y_k \mid X_k = 1] \cdot p_{11} \\
&= \left(\frac{p_{012}}{p_{\mathrm{F1}}}\right)^2 \cdot p_{11} \\
&= 4 \cdot p_{012}^2 \cdot p_{11}
\end{aligned} \tag{5.24}$$

Case 1: $Y_0 = y_0$ and $Y_k = a_3$

$$\begin{aligned}
p_{\mathrm{S1}} &= \mathbb{P}[Y_0 = y_0, Y_k = a_3] \\
&= \sum_{x_0} \sum_{x_k} \mathbb{P}[Y_0 = y_0, Y_k = a_3 \mid X_0 = x_0, X_k = x_k] \cdot \mathbb{P}[X_0 = x_0, X_k = x_k] \\
&= \mathbb{P}[Y_0 = y_0, Y_k = a_3 \mid X_0 = 1, X_k = 1] \cdot p_{11} \\
&= \mathbb{P}[Y_0 = y_0 \mid X_0 = 1] \cdot \mathbb{P}[Y_k = a_3 \mid X_k = 1] \cdot p_{11} \\
&= \frac{p_{012}}{p_{\mathrm{F1}}} \cdot \frac{p_3}{p_{\mathrm{F1}}} \cdot p_{11} \\
&= 4 \cdot p_{012} \cdot p_3 \cdot p_{11}
\end{aligned} \tag{5.25}$$

Case 2: $Y_0 = a_3$ and $Y_k = y_k$

$$\begin{aligned}
p_{\mathrm{S2}} &= \mathbb{P}[Y_0 = a_3, Y_k = y_k] \\
&= \sum_{x_0} \sum_{x_k} \mathbb{P}[Y_0 = a_3, Y_k = y_k \mid X_0 = x_0, X_k = x_k] \cdot \mathbb{P}[X_0 = x_0, X_k = x_k] \\
&= \mathbb{P}[Y_0 = a_3, Y_k = y_k \mid X_0 = 1, X_k = 1] \cdot p_{11} \\
&= \mathbb{P}[Y_0 = a_3 \mid X_0 = 1] \cdot \mathbb{P}[Y_k = y_k \mid X_k = 1] \cdot p_{11} \\
&= \frac{p_3}{p_{\mathrm{F1}}} \cdot \frac{p_{012}}{p_{\mathrm{F1}}} \cdot p_{11} \\
&= 4 \cdot p_3 \cdot p_{012} \cdot p_{11}
\end{aligned} \tag{5.26}$$

Case 3: $Y_0 = a_3$ and $Y_k = a_3$

$$\begin{aligned}
p_{\mathrm{S}3} &= \mathbb{P}[Y_0 = a_3, Y_k = a_3] \\
&= \sum_{x_0} \sum_{x_k} \mathbb{P}[Y_0 = a_3, Y_k = a_3 \mid X_0 = x_0, X_k = x_k] \cdot \mathbb{P}[X_0 = x_0, X_k = x_k] \\
&= \mathbb{P}[Y_0 = a_3, Y_k = a_3 \mid X_0 = 1, X_k = 1] \cdot p_{11} \\
&= \mathbb{P}[Y_0 = a_3 \mid X_0 = 1] \cdot \mathbb{P}[Y_k = a_3 \mid X_k = 1] \cdot p_{11} \\
&= \left(\frac{p_3}{p_{\mathrm{F}1}}\right)^2 \cdot p_{11} \\
&= 4 \cdot p_3^2 \cdot p_{11}
\end{aligned} \tag{5.27}$$

Notice that results in (5.25) and (5.26) are the same since the code is symmetric. Now that all probabilities are inspected case by case and all the cases are expressed in terms of p_3, p_{012} and p_{11}, the first sum in (5.23) can be rewritten using (5.24), (5.25), (5.26) and (5.27) where $a_m, a_n \in \{a_0, a_1, a_2, a_3\}$ and $m, n \in \{0, 1, 2, 3\}$.

$$\begin{aligned}
S &= \sum_{m=0}^{3} \sum_{n=0}^{3} a_m \cdot a_n \cdot \mathbb{P}[Y_0 = a_m, Y_k = a_n] \\
&= \sum_{m=0}^{2} \sum_{n=0}^{2} a_m \cdot a_n \cdot \mathbb{P}[Y_0 = a_m, Y_k = a_n] + \sum_{m=0}^{2} a_m \cdot a_3 \cdot \mathbb{P}[Y_0 = a_m, Y_k = a_3] \\
&\quad + \sum_{n=0}^{2} a_3 \cdot a_n \cdot \mathbb{P}[Y_0 = a_3, Y_k = a_n] + a_3 \cdot a_3 \cdot \mathbb{P}[Y_0 = a_3, Y_k = a_3] \\
&= p_{\mathrm{S}0} \cdot \sum_{m=0}^{2} \sum_{n=0}^{2} a_m \cdot a_n + p_{\mathrm{S}1} \cdot a_3 \cdot \sum_{m=0}^{2} a_m + p_{\mathrm{S}2} \cdot a_3 \cdot \sum_{n=0}^{2} a_n + p_{\mathrm{S}3} \cdot a_3^2 \\
&= 4 \cdot p_{012}^2 \cdot p_{11} \cdot \sum_{m=0}^{2} \sum_{n=0}^{2} a_m \cdot a_n + 4 \cdot p_0 \cdot p_3 \cdot p_{11} \cdot a_3 \cdot \sum_{m=0}^{2} a_m \\
&\quad + 4 \cdot p_3 \cdot p_{012} \cdot p_{11} \cdot a_3 \cdot \sum_{n=0}^{2} a_n + 4 \cdot p_3^2 \cdot p_{11} \cdot a_3^2 \\
&= 4 \cdot p_{11} \cdot \left[p_{012}^2 \cdot \sum_{m=0}^{2} \sum_{n=0}^{2} a_m \cdot a_n + 2 \cdot p_3 \cdot p_{012} \cdot a_3 \cdot \sum_{n=0}^{2} a_n + p_3^2 \cdot a_3^2 \right]
\end{aligned} \tag{5.28}$$

The term $\mathbb{P}[Y_0 = a_m, Y_k = -a_n]$ will be inspected in a similar manner where $y_0, y_k \in \{a_0, a_1, a_2\}$.

Case 0: $Y_0 = y_0$ and $Y_k = -y_k$

$$\begin{aligned}
p_{\mathrm{D}0} &= \mathbb{P}[Y_0 = y_0, Y_k = -y_k] \\
&= \sum_{x_0} \sum_{x_k} \mathbb{P}[Y_0 = y_0, Y_k = -y_k \mid X_0 = x_0, X_k = x_k] \cdot \mathbb{P}[X_0 = x_0, X_k = x_k] \\
&= \mathbb{P}[Y_0 = y_0, Y_k = -y_k \mid X_0 = 1, X_k = 0] \cdot p_{10} \\
&= \mathbb{P}[Y_0 = y_0 \mid X_0 = 1] \cdot \mathbb{P}[Y_k = -y_k \mid X_k = 0] \cdot p_{10} \\
&= \frac{p_{012}}{p_{\mathrm{F}1}} \cdot \frac{p_{012}}{p_{\mathrm{F}0}} \cdot p_{10} \\
&= 4 \cdot p_{012}^2 \cdot p_{10}
\end{aligned} \tag{5.29}$$

Case 1: $Y_0 = y_0$ and $Y_k = -a_3$

$$\begin{aligned}
p_{\mathrm{D}1} &= \mathbb{P}[Y_0 = y_0, Y_k = -a_3] \\
&= \sum_{x_0} \sum_{x_k} \mathbb{P}[Y_0 = y_0, Y_k = -a_3 \mid X_0 = x_0, X_k = x_k] \cdot \mathbb{P}[X_0 = x_0, X_k = x_k] \\
&= \mathbb{P}[Y_0 = y_0, Y_k = -a_3 \mid X_0 = 1, X_k = 0] \cdot p_{10} \\
&= \mathbb{P}[Y_0 = y_0 \mid X_0 = 1] \cdot \mathbb{P}[Y_k = a_3 \mid X_k = 0] \cdot p_{10} \\
&= \frac{p_{012}}{p_{\mathrm{F}1}} \cdot \frac{p_3}{p_{\mathrm{F}0}} \cdot p_{10} \\
&= 4 \cdot p_{012} \cdot p_3 \cdot p_{10}
\end{aligned} \tag{5.30}$$

Case 2: $Y_0 = a_3$ and $Y_k = -y_k$

$$\begin{aligned}
p_{\mathrm{D}2} &= \mathbb{P}[Y_0 = a_3, Y_k = -y_k] \\
&= \sum_{x_0} \sum_{x_k} \mathbb{P}[Y_0 = a_3, Y_k = -y_k \mid X_0 = x_0, X_k = x_k] \cdot \mathbb{P}[X_0 = x_0, X_k = x_k] \\
&= \mathbb{P}[Y_0 = a_3, Y_k = -y_k \mid X_0 = 1, X_k = 0] \cdot p_{10} \\
&= \mathbb{P}[Y_0 = a_3 \mid X_0 = 1] \cdot \mathbb{P}[Y_k = -y_k \mid X_k = 0] \cdot p_{10} \\
&= \frac{p_3}{p_{\mathrm{F}1}} \cdot \frac{p_{012}}{p_{\mathrm{F}0}} \cdot p_{10} \\
&= 4 \cdot p_3 \cdot p_{012} \cdot p_{10}
\end{aligned} \tag{5.31}$$

Case 3: $Y_0 = a_3$ and $Y_k = -a_3$

$$\begin{aligned}
p_{\mathrm{D3}} &= \mathbb{P}[Y_0 = a_3, Y_k = -a_3] \\
&= \sum_{x_0} \sum_{x_k} \mathbb{P}[Y_0 = a_3, Y_k = -a_3 \mid X_0 = x_0, X_k = x_k] \cdot \mathbb{P}[X_0 = x_0, X_k = x_k] \\
&= \mathbb{P}[Y_0 = a_3, Y_k = -a_3 \mid X_0 = 1, X_k = 0] \cdot p_{10} \\
&= \mathbb{P}[Y_0 = a_3 \mid X_0 = 1] \cdot \mathbb{P}[Y_k = -a_3 \mid X_k = 0] \cdot p_{10} \\
&= \frac{p_3}{p_{\mathrm{F1}}} \cdot \frac{p_3}{p_{\mathrm{F0}}} \cdot p_{10} \\
&= 4 \cdot p_3^2 \cdot p_{10}
\end{aligned} \tag{5.32}$$

Notice that results in (5.30) and (5.31) are also the same since the code is symmetric. Now that all the cases are expressed in terms of p_3, p_{012} and p_{10}, the second sum in (5.23) can be rewritten using (5.29), (5.30), (5.31) and (5.32) as follows where $a_m, a_n \in \{a_0, a_1, a_2, a_3\}$ and $m, n \in \{0, 1, 2, 3\}$:

$$\begin{aligned}
D &= -\sum_{m=0}^{3} \sum_{n=0}^{3} a_m \cdot a_n \cdot \mathbb{P}[Y_0 = a_m, Y_k = -a_n] \\
&= -\sum_{m=0}^{2} \sum_{n=0}^{2} a_m \cdot a_n \cdot \mathbb{P}[Y_0 = a_m, Y_k = -a_n] - \sum_{m=0}^{2} a_m \cdot a_3 \cdot \mathbb{P}[Y_0 = a_m, Y_k = -a_3] \\
&\quad - \sum_{n=0}^{2} a_3 \cdot a_n \cdot \mathbb{P}[Y_0 = a_3, Y_k = -a_n] - a_3 \cdot a_3 \cdot \mathbb{P}[Y_0 = a_3, Y_k = -a_3] \\
&= -p_{\mathrm{D0}} \cdot \sum_{m=0}^{2} \sum_{n=0}^{2} a_m \cdot a_n - p_{\mathrm{D1}} \cdot a_3 \cdot \sum_{m=0}^{2} a_m - p_{\mathrm{D2}} \cdot a_3 \cdot \sum_{n=0}^{2} a_n - p_{\mathrm{D3}} \cdot a_3^2 \\
&= -4 \cdot p_{012}^2 \cdot p_{10} \cdot \sum_{m=0}^{2} \sum_{n=0}^{2} a_m \cdot a_n - 4 \cdot p_{012} \cdot p_3 \cdot p_{10} \cdot a_3 \cdot \sum_{m=0}^{2} a_m \\
&\quad - 4 \cdot p_3 \cdot p_{012} \cdot p_{10} \cdot a_3 \cdot \sum_{n=0}^{2} a_n - 4 \cdot p_3^2 \cdot p_{10} \cdot a_3^2 \\
&= -4 \cdot p_{10} \cdot \left[p_{012}^2 \cdot \sum_{m=0}^{2} \sum_{n=0}^{2} a_m \cdot a_n + 2 \cdot p_3 \cdot p_{012} \cdot a_3 \cdot \sum_{n=0}^{2} a_n + p_3^2 \cdot a_3^2 \right].
\end{aligned} \tag{5.33}$$

Notice that the results in (5.28) and (5.33) have the same term in brackets. Call this term W.

$$W = p_{012}^2 \cdot \sum_{m=0}^{2} \sum_{n=0}^{2} a_m \cdot a_n + 2 \cdot p_3 \cdot p_{012} \cdot a_3 \cdot \sum_{n=0}^{2} a_n + p_3^2 \cdot a_3^2 \tag{5.34}$$

Thus, the expression for the auto-correlation of Y_n found in (5.23) becomes:

$$\begin{aligned}\mathbb{E}[Y_0 Y_k] &= 2 \cdot S + 2 \cdot D \\ &= 8 \cdot p_{11} \cdot W - 8 \cdot p_{10} \cdot W \\ &= 8 \cdot W \cdot (p_{11} - p_{10}) \,. \end{aligned} \tag{5.35}$$

Since p_{10} was already written in terms of p_{11} in (5.21), (5.35) can be further simplified.

$$\begin{aligned}\mathbb{E}[Y_0 Y_k] &= 8W \,(p_{11} - p_{10}) \\ &= 8W \,(\mathbb{E}[X_0 X_k] - (0.5 - E[X_0 X_k])) \\ &= 8W \,(2\mathbb{E}[X_0 X_k] - 0.5) \\ &= 4W \,(4\mathbb{E}[X_0 X_k] - 1) \,, \quad k \neq 0. \end{aligned} \tag{5.36}$$

Note that the result in 5.36 is found by using the total probability theorem and since the symbols in both families are not equiprobable, a weighted average is found for this case. Also, observe that the results for $\mathbb{E}[Y_0 Y_k], k \neq 0$ in (5.36) for OP-LOCO codes and (3.18) for SP-LOCO codes are the same except the value of the constants. Now, it is achieved to have the auto-correlation function of $\{Y_n\}$ in terms of the auto-correlation function of $\{X_n\}$ for $k \neq 0$. Then, $\mathbb{R}_Y(k)$ can be written as follows:

$$\mathbb{R}_Y(k) = \begin{cases} 4W \,(4\mathbb{R}_X(k) - 1) \,, & \text{if } k \neq 0, \\ \mathbb{R}_Y(0), & \text{if } k = 0. \end{cases} \tag{5.37}$$

Observe that $\mathbb{R}_Y(k)$ defined in (5.37) is analogous to the generic $\mathbb{R}_Y(k)$ defined in (3.22). Therefore the conclusions obtained for (3.22) apply here also.

Then, respective a and b constants for (5.37) can be written considering (3.21) as follows:

$$\begin{aligned} a &= 16W, \\ b &= -4W. \end{aligned} \tag{5.38}$$

Also, using the definitions in (3.24) the following expressions can be written for

(5.37):

$$\begin{aligned}\text{Addition} &= \mathbb{E}[Y_n^2] \\ &= \sum_{m=0}^{3} a_m^2 \mathbb{P}[Y_n = a_m] + \sum_{m=0}^{3} (-a_m)^2 \mathbb{P}[Y_n = -a_m] \\ &= 2\sum_{m=0}^{3} a_m^2 \mathbb{P}[Y_n = a_m] \\ &= 2\left(a_0^2 \cdot p_{012} + a_1^2 \cdot p_{012} + a_2^2 \cdot p_{012} + a_3^2 \cdot p_3\right) \\ &= 2\left(p_{012} \cdot (a_0^2 + a_1^2 + a_2^2) + p_3 \cdot a_3^2\right) \end{aligned} \tag{5.39}$$

$$\begin{aligned}\text{Subtraction} &= a\mathbb{E}[X_n^2] + b \\ &= 16W \cdot \frac{1}{2} - 4W = 4W, \end{aligned} \tag{5.40}$$

$$\begin{aligned}\text{Correction} &= \text{Addition} - \text{Subtraction} \\ &= 2\left(p_{012} \cdot (a_0^2 + a_1^2 + a_2^2) + p_3 \cdot a_3^2\right) - 4W \end{aligned} \tag{5.41}$$

$$\begin{aligned} S_Y(f) &= aS_X(f) + b\delta(f) + \text{Correction} \\ &= 16W S_X(f) - 4W\delta(f) + 2\left(p_{012}(a_0^2 + a_1^2 + a_2^2) + p_3 a_3^2\right) - 4W \end{aligned} \tag{5.42}$$

Note that the correction term in (5.42) is a constant offset, not a Dirac delta function. Now, the second general conclusion obtained in (3.27) can be inspected as follows for finding the area of the Dirac delta function in $S_Y(f)$ where $S_Y^d(f)$ represents the discrete part of the spectra for OP-LOCO codes:

$$\begin{aligned} S_Y^d(f) &= \mathbb{E}^2[Y_n]\delta(f) \\ &= \left[\sum_{m=0}^{3} a_m \mathbb{P}[Y_n = a_m] + \sum_{m=0}^{3} (-a_m)\mathbb{P}[Y_n = -a_m]\right]^2 \delta(f) \\ &= \left[\sum_{m=0}^{3} a_m \mathbb{P}[Y_n = a_m] - \sum_{m=0}^{3} a_m \mathbb{P}[Y_n = -a_m]\right]^2 \delta(f) \\ &= 0 \end{aligned} \tag{5.43}$$

Since OP-LOCO codes are also symmetric, the expected value of the physical level sequence is zero. Therefore, $S_Y(f)$ does not involve any Dirac delta function as shown in (5.43). Now, the writing signal needs to be applied to S_Y.

$$S_W(f) = \text{sinc}^2(\pi f) \cdot S_Y(f). \tag{5.44}$$

After obtaining S_W in terms of S_X, the method given in [8] and described in Subsection 2.2.1 can be applied for finding S_X. The first step is creating an FSTD for OP-LOCO codes and finding the maxentropic probabilities accordingly using the method described in [72], which was already done. Figure 5.1 shows an FSTD for infinite length OP-LOCO codes with maxentropic transition probabilities given in (5.5), from which a binary FSTD should be constructed. Remember the discussion given earlier on why an approximation method was needed instead of an exact solution, the existence of more than two groups of symbols in the forbidden patterns set. The method offered is making two transitions from each state in the binary FSTD considering the actual maxentropic symbol probabilities. Observe that having two transitions from each state would not strictly forbid any pattern but it would generate a lower probability for some patterns to form, which makes this method an approximation.

First, observe the transitions in the non-binary FSTD given in Figure 5.1. The states F_1 and F_2 allow all 8 symbols to be generated because no immediate action needs to be taken to forbid any symbol from being generated. However, states F_3 and F_4 only allow 4 specific symbols to be generated so that forbidden patterns would not occur. Since there will be no real restrictions on any symbol to be generated in the binary FSTD, the transition probabilities from states F_1 and F_2 will be used.

Note that states F_1 and F_2 are symmetric and consider state F_1 for now. All incoming transitions are from the symbols that belong to family of 0's. So, if the detrimental symbol from the family of 1's, which is α, gets generated from an outgoing transition of state F_1, it would be dangerous. This transition probability is represented as $v_{1,4}$ in $\mathbf{V}$, which is named as p_d, referring to the danger. Another outgoing transition probability from state F_1 is $v_{1,1}$, and this transition would not change the current status since the resultant state is again F_1 with a symbol from a family of 0's generated. Let this transition probability be named p_n, which refers to neutral. The last outgoing transition probability is $v_{1,2}$, creating one of the non-detrimental symbols from the family of 1's. Since incoming transitions to state F_1 generated a symbol from the family of 0's, symbol α is dangerous, and this transition would make sure to move on safely. Let this transition probability be named p_s, which refers to safe. Also, note that state F_2 can be inspected in detail symmetrically. The probabilities renamed so

far are as follows:

$$\begin{aligned} p_d &= v_{1,4}, \\ p_n &= v_{1,1}, \\ p_s &= v_{1,3}. \end{aligned} \tag{5.45}$$

Create a binary FSTD where each state represents lastly generated 2 bits. The symbols from $\mathrm{GF}(8)$ will be mapped to 1 if they belong to $\mathcal{F}_1$ which is defined in (5.11) and will be mapped to 0 otherwise. The state 00 is not at risk of producing a forbidden pattern with one transition. Hence, it will return to itself with probability p_n and will go to state 01 with probability $p_s + p_d$. Symmetrically, state 11 will return to itself with probability p_n and will go to state 10 with probability $p_s + p_d$. The state 01 may generate a forbidden pattern if the last bit 1 was the result of an α. In order to reduce the chances of creating a forbidden pattern, p_d should be directed to state 11 combined with the probability of p_n. So, state 01 goes to state 11, generating a 1 with probability of $p_d + p_n$. The probability p_s that represents the non-detrimental symbols in a family will be directed to state 10 with generating a 0. Again, symmetrically, state 10 will go to state 00 with generating a 0 with probability $p_d + p_n$ and will go to state 01 with generating a 1 with probability p_s. The discussed binary FSTD can be seen in Figure 5.2. For ease of notation for the later derivations, define the probabilities as follows:

$$\begin{aligned} a &= p_s + p_d, \\ b &= p_n + p_d, \\ c &= p_n, \\ d &= p_s. \end{aligned} \tag{5.46}$$

Now, the binary FSTD given in Figure 5.2 needs to be converted into an OSTD, as explored in Section 2.2. Note that the gray-colored states in Figure 5.2 represents the states that will be used in the OSTD since all incoming transitions are with bit 1. Then, using the OSTD given in Figure 5.3, OSTM can be constructed as follows:

$$\mathbf{G}(D) = \begin{bmatrix} \beta & bD \\ \alpha & cD \end{bmatrix}, \tag{5.47}$$

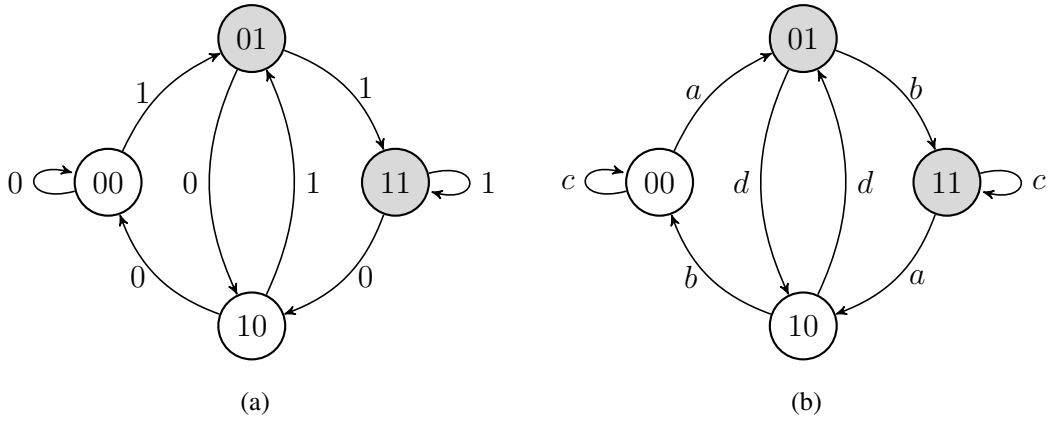

Figure 5.2: (a) A binary FSTD that represents the approximation method for infinite length OP-LOCO codes, (b) The same FSTD with transition probabilities on the edges.

Figure 5.3: (a) OSTD that is formed considering the binary FSTD of OP-LOCO codes where the numbers represent the run-lengths, (b) OSTD with transition probabilities on the edges for infinite-length OP-LOCO constrained sequence.

$$\begin{aligned}\beta &= d^2D^2 + dbaD^3 + dbcaD^4 + dbc^2aD^5 + \dots \\ &= d^2D^2 + dbaD^3\sum_{k=0}^{\infty}(cD)^k = d^2D^2 + \frac{dbaD^3}{1-cD}\end{aligned} \tag{5.48}$$

$$\begin{aligned}\alpha &= adD^2 + a^2bD^3 + a^2bcD^4 + \dots \\ &= adD^2 + a^2bD^3\sum_{k=0}^{\infty}(cD)^k = adD^2 + \frac{a^2bD^3}{1-cD}\end{aligned} \tag{5.49}$$

Finally, with (5.47) obtained above, the PSD $S_X(D)$ can be obtained through the method defined in (2.4).

5.3 Results

This section will apply the approximation method provided and the conventional methods to the randomly generated sequences using MC simulations where a sequence is 10^7 elements. The difference between the theoretical and experimental results will be calculated using the mean square error (MSE) formula among all points.

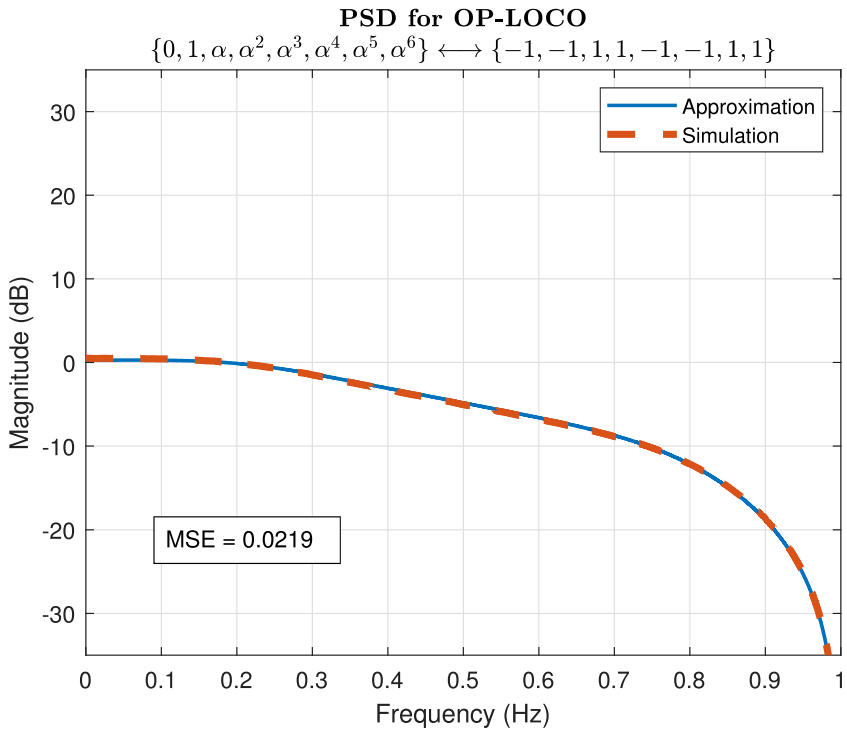

Figure 5.4: PSD of OP-LOCO codes where all the physical levels are the same.

Figure 5.4 shows that the approximation is nearly the same as experimental results, and the MSE is 0.0219. However, this low MSE was expected since 2 distinct levels exist, $+1$ and -1. Further inspection at more distinct physical levels is needed to confirm that the approximation method works well.

Figure 5.5 shows that the approximation versus the experimental results give an MSE of 0.0203 with 1 level apart physical levels. In fact, MSE decreases compared to Figure 5.4 even though the physical levels are increased in magnitude. So far, the error magnitude seems unrelated to the magnitudes of the physical levels.

Figure 5.6 shows that the approximation is very close to the experimental results

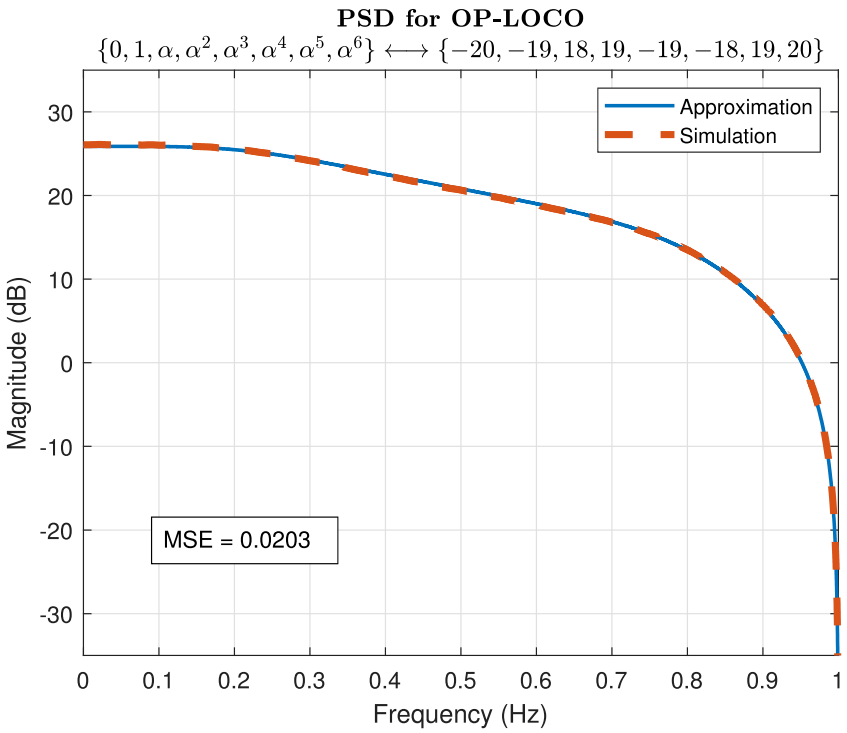

Figure 5.5: PSD of OP-LOCO codes where the physical levels are 1 level apart.

with 2 physical level differentiation also, creating an MSE of 0.0223. The magnitude increase in error compared to Figure 5.5 is very slight even though the magnitude in physical levels is decreased. Therefore, this increase in error should result from the physical level difference, which is 2.

Figure 5.7 shows that the approximation is still close to the experimental results enough that the characteristic shape of the PSD is preserved in the case of 4 physical level differentiation. However, the MSE is 0.0461. Although it is still very low compared to Figures 5.4, 5.5 and 5.6, the MSE is nearly double. Physical level magnitudes are similar compared with 5.6. Thus, it can be said that as the differentiation magnitude between physical levels increases, MSE also increases.

So far, results show that the approximation method works well in different magnitude levels, whether high or low, or the difference between consecutive physical levels is high or low. Thus, the approximation method can be applied with any voltage level considering the baseline properties of the physical level mapping from the $\mathrm{GF}(8)$ symbols, which are $a_0 > a_1 > a_2 > a_3 > 0$.

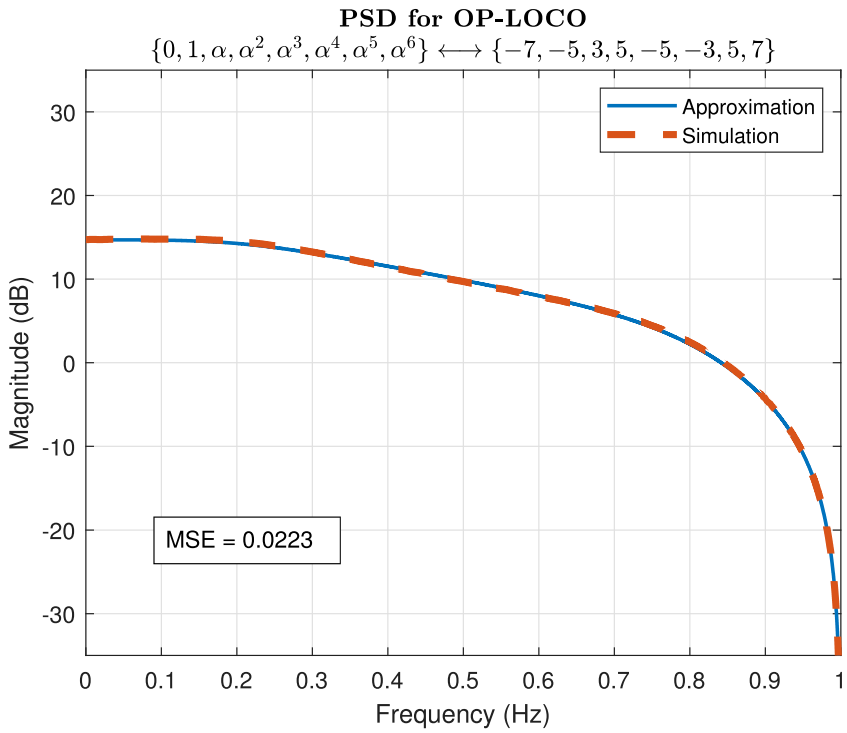

Figure 5.6: PSD of OP-LOCO codes where the physical levels are 2 levels apart.

The possible effects of the assumption made for the equivalence between the symbols belonging to the same set, 3-tuples having the first or the third track bits in complementary sign with respect to the middle track, was inspected in Section 3.3. The conclusion was that the assumption was logical and did not affect the results. While this conclusion is still expected for the approximation method for OP-LOCO codes, different mapping for symbols a_1 and a_2 will be inspected by setting their physical levels differently in two possible cases for complete justification of the method.

Figure 5.8 shows that the approximation versus experimental results give an MSE of 0.0472 when different physical levels are defined for a_1 and a_2, where $a_1 > a_2$. Compared with the MSE in Figure 5.7, the increase is very slight.

It is seen from Figure 5.9 that the approximation versus the experimental results gives an MSE of 0.0471 when different physical levels are defined for a_1 and a_2, where $a_1 > a_2$. Compared with the MSE in Figure 5.7, the increase is again very slight. Compared with the MSE in Figure 5.8, the results are nearly identical. Thus, it can be said that the assumption of $a_1 = a_2$ did not alter the results, and even if they are

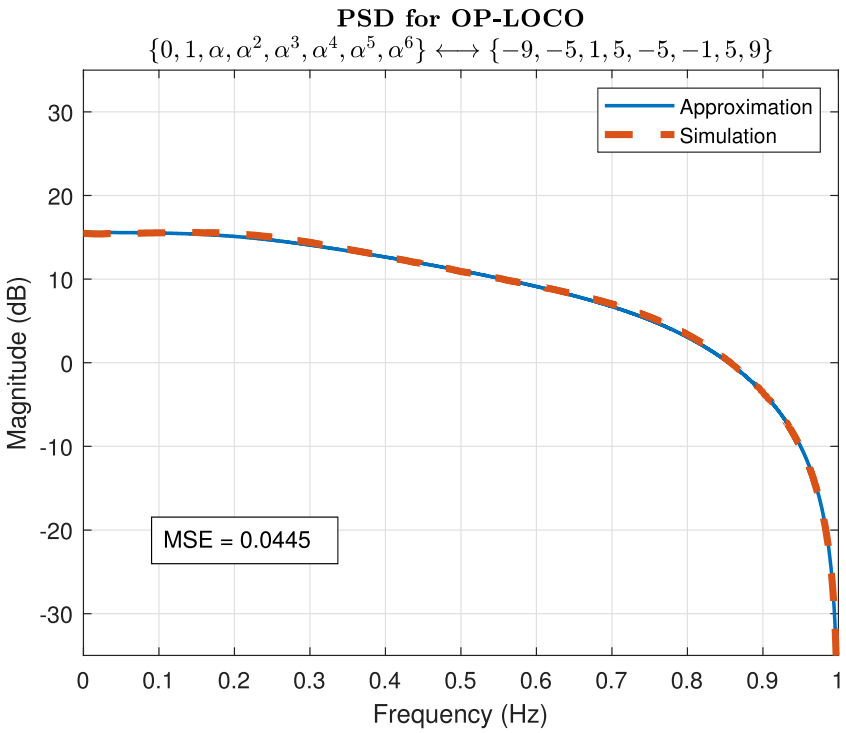

Figure 5.7: PSD of OP-LOCO codes where the physical levels are 4 levels apart.

set differently in both settings, the MSE is not affected. Therefore, the approximation method proposed in this chapter can be applied to any physical-level mapping as demonstrated in (5.9).

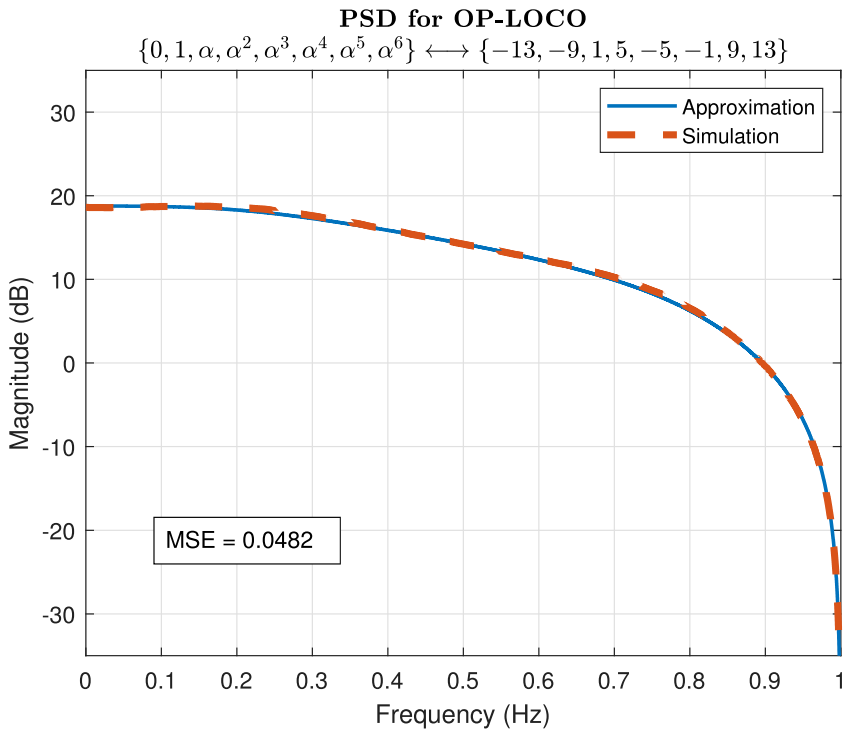

Figure 5.8: PSD of OP-LOCO codes, the physical levels are 4 levels apart, $a_1 > a_2$.

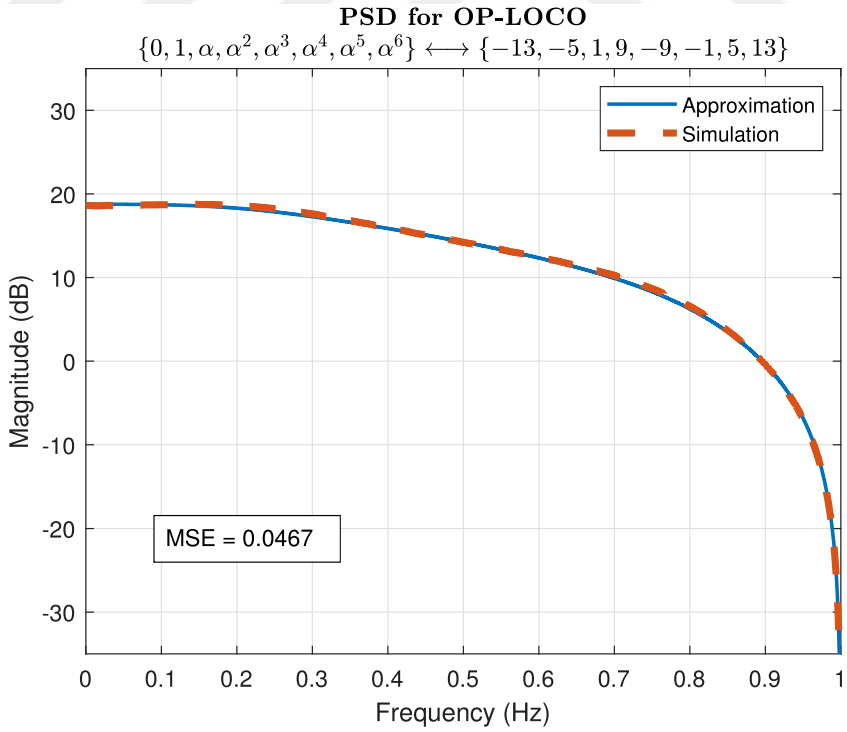

Figure 5.9: PSD of OP-LOCO codes, the physical levels are 4 levels apart, $a_2 > a_1$.

Acknowledgments

The contributions made by Assist. Prof. Ahmed Hareedy was instrumental in completing this section.

CHAPTER 6

CONCLUSION

Analyzing the PSD for constrained codes is crucial for optimizing the performance of data storage and communication systems. In this thesis, novel methods for obtaining the PSD theoretically for multi-level constrained codes are developed, which address a significant gap in current research. By comparing the theoretical derivation and Monte Carlo simulations, it is demonstrated that the suggested approaches provide accurate PSD calculations. An approximation method for obtaining the PSD for multi-level constrained codes with more complex state diagrams is also introduced, which achieves a strong match between the theoretical and simulated PSD with low MSE. The main idea of mapping the multi-level sequence to binary sequences and using a probabilistic approximation method shows that these derivations can be further applied to the multi-level constrained codes of interest. This work contributes to both theoretical advancements and practical applications in Flash memory and magnetic recording devices. By addressing the challenge of obtaining the PSD theoretically by multi-level constrained codes, this thesis lays the foundation for future research. It broadens the chance of optimization in coding theory, which will ultimately enhance the efficiency and reliability of modern data storage technologies. Future work includes extending the methods provided for finite length codes and how the PSD can help the designer identify the device's status in terms of aging and dilapidation.

REFERENCES

[1] O. Manz, *Data Transmission and Storage*, pp. 1–4. Springer Wiesbaden, 2021.

[2] S. Lashkare, W. Uddin, K. Priyadarshi, and U. Ganguly, "Emerging memory technologies for data storage and brain-inspired computation: A global view with Indian research insights with a focus on resistive memories," *Proceedings of the National Academy of Sciences, India Section A: Physical Sciences*, vol. 93, pp. 459–476, Sep 2023.

[3] B. Bhushan, "Current status and outlook of magnetic data storage devices," *Microsystem Technologies*, vol. 29, pp. 1529–1546, Nov 2023.

[4] D. Chatzoulis, C. Chaikalis, D. Kosmanos, K. E. Anagnostou, and G. T. Karetsos, "5G V2X performance comparison for different channel coding schemes and propagation models," *Sensors*, vol. 23, no. 5, 2023.

[5] T. Ali, A. R. Razwan, I. Baig, M. Irfan, and U. Draz, "Efficient shadow encoding scheme towards power spectrum density in digital network communication," *Wireless Personal Communications*, vol. 119, pp. 3179–3206, Aug. 2021.

[6] K. Schouhamer Immink, *Codes for Mass Data Storage Systems*. Shannon Foundation Publisher, 11 2004.

[7] A. Gallopoulos, C. Heegard, and P. Siegel, "The power spectrum of run-length-limited codes," *IEEE Transactions on Communications*, vol. 37, no. 9, pp. 906–917, 1989.

[8] J. Centers, X. Tan, A. Hareedy, and R. Calderbank, "Power spectra of constrained codes with level-based signaling: Overcoming finite-length challenges," *IEEE Transactions on Communications*, vol. 69, no. 8, pp. 4971–4986, 2021.

[9] B. S. Bosik, "The spectral density of a coded digital signal," *The Bell System Technical Journal*, vol. 51, no. 4, pp. 921–932, 1972.

[10] G. Cariolaro and G. Tronca, "Spectra of block coded digital signals," *IEEE Transactions on Communications*, vol. 22, no. 10, pp. 1555–1564, 1974.

[11] J. Justesen, "Calculation of power spectra for block coded signals," *IEEE Transactions on Communications*, vol. 49, no. 3, pp. 389–392, 2001.

[12] C. Pimentel and V. C. da Rocha, "On the power spectral density of constrained sequences," *IEEE Transactions on Communications*, vol. 55, no. 3, pp. 409–416, 2007.

[13] E. Biglieri and G. Caire, "Power spectrum of block-coded modulation," *IEEE Transactions on Communications*, vol. 42, no. 234, pp. 1580–1585, 1994.

[14] D. Lindholm, "Power spectra of channel codes for digital magnetic recording," *IEEE Transactions on Magnetics*, vol. 14, no. 5, pp. 321–323, 1978.

[15] C. Menyennett and H. Ferreira, "Spectral properties of (d, k) codes with multiple spacing," *IEEE Transactions on Magnetics*, vol. 30, no. 6, pp. 4215–4217, 1994.

[16] D. Bishop, S. Million, T. Nguyen, and M. Simon, "Power spectrum of unbalanced nrz and biphase signals in the presence of data asymmetry," *IEEE Transactions on Electromagnetic Compatibility*, vol. 40, no. 1, pp. 55–61, 1998.

[17] R. Karabed and P. H. Siegel, "Coding for higher-order partial-response channels," in *Coding and Signal Processing for Information Storage* (R. M. Rao, S. A. Dianat, S. W. McLaughlin, and M. Hassner, eds.), vol. 2605, pp. 115 – 126, International Society for Optics and Photonics, SPIE, 1995.

[18] B. Vasic and E. Kurtas, *Coding and Signal Processing for Magnetic Recording Systems*. CRC Press, 2005.

[19] A. Hareedy and R. Calderbank, "LOCO codes: Lexicographically-ordered constrained codes," *IEEE Transactions on Information Theory*, vol. 66, no. 6, pp. 3572–3589, 2020.

[20] A. Hareedy, R. Wu, and L. Dolecek, "A channel-aware combinatorial approach to design high performance spatially-coupled codes," *IEEE Transactions on Information Theory*, vol. 66, no. 8, pp. 4834–4852, 2020.

[21] C. E. Shannon, "A mathematical theory of communication," *The Bell System Technical Journal*, vol. 27, no. 3, pp. 379–423, 1948.

[22] K. A. S. Immink, "Innovation in constrained codes," *IEEE Communications Magazine*, vol. 60, no. 10, pp. 20–24, 2022.

[23] K. A. S. Immink, P. Siegel, and J. Wolf, "Codes for digital recorders," *IEEE Transactions on Information Theory*, vol. 44, no. 6, pp. 2260–2299, 1998.

[24] D. T. Tang and R. L. Bahl, "Block codes for a class of constrained noiseless channels," *Information and Control*, vol. 17, no. 5, pp. 436–461, 1970.

[25] S. R. Sridhara and N. R. Shanbhag, "Coding for reliable on-chip buses: a class of fundamental bounds and practical codes," *IEEE Transactions on Computer-Aided Design of Integrated Circuits and Systems*, vol. 26, no. 5, pp. 977–982, 2007.

[26] J. Saadé, A. Goulahsen, A. Picco, J. Huloux, and F. Pétrot, "Low overhead, dc-balanced and run length limited line coding," in *2015 IEEE 19th Workshop on Signal and Power Integrity (SPI)*, pp. 1–4, 2015.

[27] P. Siegel, "Recording codes for digital magnetic storage," *IEEE Transactions on Magnetics*, vol. 21, no. 5, pp. 1344–1349, 1985.

[28] A. Hareedy, B. Dabak, and R. Calderbank, "Managing device lifecycle: Reconfigurable constrained codes for M/T/Q/P-LC Flash memories," *IEEE Transactions on Information Theory*, vol. 67, no. 1, pp. 282–295, 2021.

[29] K. Immink, "A practical method for approaching the channel capacity of constrained channels," *IEEE Transactions on Information Theory*, vol. 43, no. 5, pp. 1389–1399, 1997.

[30] T. Cover, "Enumerative source encoding," *IEEE Transactions on Information Theory*, vol. 19, no. 1, pp. 73–77, 1973.

[31] A. Hareedy, B. Dabak, and R. Calderbank, "The secret arithmetic of patterns: A general method for designing constrained codes based on lexicographic indexing," *IEEE Transactions on Information Theory*, vol. 68, no. 9, pp. 5747–5778, 2022.

[32] L. Sassatelli and D. Declercq, "Non-binary hybrid LDPC codes: structure, decoding and optimization," in *2006 IEEE Information Theory Workshop - ITW '06 Chengdu*, pp. 71–75, 2006.

[33] M. Qin, E. Yaakobi, and P. H. Siegel, "Constrained codes that mitigate inter-cell interference in read/write cycles for Flash memories," *IEEE Journal on Selected Areas in Communications*, vol. 32, no. 5, pp. 836–846, 2014.

[34] I. Guzel, D. Özbayrak, R. Calderbank, and A. Hareedy, "Eliminating media noise while preserving storage capacity: Reconfigurable constrained codes for two-dimensional magnetic recording," *IEEE Transactions on Information Theory*, vol. 70, no. 7, pp. 4905–4927, 2024.

[35] D. Özbayrak, D. Uyar, and A. Hareedy, "Low-complexity constrained coding schemes for two-dimensional magnetic recording," in *2024 IEEE International Symposium on Information Theory (ISIT)*, pp. 1–6, 2024.

[36] C. İrimağzı, Y. Uslan, and A. Hareedy, "Protecting the future of information: LOCO coding with error detection for DNA data storage," *IEEE Transactions on Molecular, Biological, and Multi-Scale Communications*, vol. 10, no. 2, pp. 317–333, 2024.

[37] A. Oppenheim and G. Verghese, *Signals, Systems and Inference*. Prentice Hall, 2015.

[38] W. S. Gan, *Convolution, Correlation, and Power Spectral Density*, pp. 21–30. Singapore: Springer Singapore, 2020.

[39] A. R. Bansal and V. P. Dimri, *Power Spectral Density*, pp. 1092–1095. Cham: Springer International Publishing, 2023.

[40] T. Coughlin, "A timeline for Flash memory history [the art of storage]," *IEEE Consumer Electronics Magazine*, vol. 6, no. 1, pp. 126–133, 2017.

[41] Y. Cai, Y. Luo, E. F. Haratsch, K. Mai, and O. Mutlu, "Data retention in MLC NAND Flash memory: Characterization, optimization, and recovery," in *2015 IEEE 21st International Symposium on High Performance Computer Architecture (HPCA)*, pp. 551–563, 2015.

[42] Z. Jun, "Flash memory technology development," in *2001 6th International Conference on Solid-State and Integrated Circuit Technology. Proceedings (Cat. No.01EX443)*, vol. 1, pp. 189–194 vol.1, 2001.

[43] S. S. Kim, S. K. Yong, W. Kim, S. Kang, H. W. Park, K. J. Yoon, D. S. Sheen, S. Lee, and C. S. Hwang, "Review of semiconductor Flash memory devices for material and process issues," *Advanced Materials*, vol. 35, no. 43, p. 2200659, 2023.

[44] A. Leventhal, "Flash storage today: Can Flash memory become the foundation for a new tier in the storage hierarchy?," *Queue*, vol. 6, p. 24–30, jul 2008.

[45] H. Kim, N. Agrawal, and C. Ungureanu, "Revisiting storage for smartphones," *ACM Trans. Storage*, vol. 8, dec 2012.

[46] S. Byan, J. Lentini, A. Madan, L. Pabon, M. Condict, J. Kimmel, S. Kleiman, C. Small, and M. Storer, "Mercury: Host-side flash caching for the data center," in *2012 IEEE 28th Symposium on Mass Storage Systems and Technologies (MSST)*, pp. 1–12, 2012.

[47] P. Cappelletti, R. Bez, D. Cantarelli, and L. Fratin, "Failure mechanisms of flash cell in program/erase cycling," in *Proceedings of 1994 IEEE International Electron Devices Meeting*, pp. 291–294, 1994.

[48] C.-Y. Lu, *Future prospects of NAND Flash memory technology–the evolution from floating gate to charge trapping to 3D stacking.*, vol. 12 10, pp. 7604–18. American Scientific Publishers, 2012.

[49] J. Bruck, A. Vardy, A. Jiang, E. Yaakobi, J. K. Wolf, R. Mateescu, and P. H. Siegel, "Storage coding for wear leveling in Flash memories," *IEEE Transactions on Information Theory*, vol. 56, pp. 5290–5299, 2009.

[50] J.-D. Lee, S.-H. Hur, and J.-D. Choi, "Effects of floating-gate interference on NAND Flash memory cell operation," *IEEE Electron Device Letters*, vol. 23, no. 5, pp. 264–266, 2002.

[51] V. Taranalli, H. Uchikawa, and P. H. Siegel, "Error analysis and inter-cell interference mitigation in multi-level cell Flash memories," in *2015 IEEE International Conference on Communications (ICC)*, pp. 271–276, 2015.

[52] R. Motwani, "Hierarchical constrained coding for floating-gate to floating-gate coupling mitigation in Flash memory," in *2011 IEEE Global Telecommunications Conference - GLOBECOM 2011*, pp. 1–5, 2011.

[53] Y. M. Chee, J. Chrisnata, H. M. Kiah, S. Ling, T. T. Nguyen, and V. K. Vu, "Capacity-achieving codes that mitigate intercell interference and charge leakage in Flash memories," *IEEE Transactions on Information Theory*, vol. 65, no. 6, pp. 3702–3712, 2019.

[54] A. Hareedy and R. Calderbank, "Asymmetric LOCO codes: Constrained codes for Flash memories," in *2019 57th Annual Allerton Conference on Communication, Control, and Computing (Allerton)*, pp. 124–131, 2019.

[55] A. Berman and Y. Birk, "Constrained Flash memory programming," in *2011 IEEE International Symposium on Information Theory Proceedings*, pp. 2128–2132, 2011.

[56] H. Coufal, L. Dhar, and C. D. Mee, "Materials for magnetic data storage: The ongoing quest for superior magnetic materials," *MRS Bulletin*, vol. 31, no. 5, pp. 374–378, 2006.

[57] R. Wood, M. Williams, A. Kavcic, and J. Miles, "The feasibility of magnetic recording at 10 terabits per square inch on conventional media," *IEEE Transactions on Magnetics*, vol. 45, no. 2, pp. 917–923, 2009.

[58] K. S. Chan and M. R. Elidrissi, "A system level study of two-dimensional magnetic recording (TDMR)," *IEEE Transactions on Magnetics*, vol. 49, no. 6, pp. 2812–2817, 2013.

[59] R. H. Victora, S. M. Morgan, K. Momsen, E. Cho, and M. F. Erden, "Two-dimensional magnetic recording at 10 Tbits/in^2," *IEEE Transactions on Magnetics*, vol. 48, no. 5, pp. 1697–1703, 2012.

[60] M. Bahrami, C. K. Matcha, S. M. Khatami, S. Roy, S. G. Srinivasa, and B. Vasić, "Investigation into harmful patterns over multitrack shingled magnetic detection using the Voronoi model," *IEEE Transactions on Magnetics*, vol. 51, no. 12, pp. 1–7, 2015.

[61] S. G. Srinivasa, Y. Chen, and S. Dahandeh, "A communication-theoretic framework for 2-DMR channel modeling: Performance evaluation of coding and signal processing methods," *IEEE Transactions on Magnetics*, vol. 50, no. 3, pp. 6–12, 2014.

[62] K. Pituso, C. Warisarn, D. Tongsomporn, and P. Kovintavewat, "An inter-track interference subtraction scheme for a rate-4/5 modulation code for two-dimensional magnetic recording," *IEEE Magnetics Letters*, vol. 7, pp. 1–5, 2016.

[63] S. S. Garani, L. Dolecek, J. Barry, F. Sala, and B. Vasić, "Signal processing and coding techniques for 2-D magnetic recording: An overview," *Proceedings of the IEEE*, vol. 106, no. 2, pp. 286–318, 2018.

[64] A. Sharov and R. M. Roth, "Two-dimensional constrained coding based on tiling," *IEEE Transactions on Information Theory*, vol. 56, no. 4, pp. 1800–1807, 2010.

[65] B. Dabak, A. Hareedy, and R. Calderbank, "Non-binary constrained codes for two-dimensional magnetic recording," *IEEE Transactions on Magnetics*, vol. 56, no. 11, pp. 1–10, 2020.

[66] S. Halevy, J. Chen, R. Roth, P. Siegel, and J. Wolf, "Improved bit-stuffing bounds on two-dimensional constraints," *IEEE Transactions on Information Theory*, vol. 50, no. 5, pp. 824–838, 2004.

[67] A. Kato and K. Zeger, "On the capacity of two-dimensional run-length constrained channels," *IEEE Transactions on Information Theory*, vol. 45, no. 5, pp. 1527–1540, 1999.

[68] P. Siegel and J. Wolf, "Bit-stuffing bounds on the capacity of 2-dimensional constrained arrays," in *Proceedings. 1998 IEEE International Symposium on Information Theory (Cat. No.98CH36252)*, pp. 323–, 1998.

[69] S. S. Garani and B. Vasi´c, "Channels engineering in magnetic recording: from theory to practice," *IEEE BITS the Information Theory Magazine*, pp. 1–36, 2023.

[70] D. A. Huffman, “A method for the construction of minimum-redundancy codes,” *Proceedings of the IRE*, vol. 40, no. 9, pp. 1098–1101, 1952.

[71] A. Hareedy, S. Zheng, P. H. Siegel, and R. Calderbank, “Efficient constrained codes that enable page separation in modern Flash memories,” *IEEE Transactions on Communications*, vol. 71, no. 12, pp. 6834–6848, 2023.

[72] B. H. Marcus, R. M. Roth, and P. H. Siegel, “An introduction to coding for constrained systems,” 2001. Lecture notes.